Australian National University

InGaAs/GaAs Quantum Dot Solar Cells by Metal Organic Chemical Vapour Deposition

Haofeng Lu

A THESIS SUBMITTED FOR THE DEGREE OF DOCTOR OF PHILOSOPHY

OF THE AUSTRALIAN NATIONAL UNIVERSITY

October 2016

Department of Electronic Materials Engineering

Research School of Physics and Engineering

College of Physical and Mathematical Sciences

The Australian National University

Declaration

This thesis contains no material which has been accepted for the award of any other degree or diploma in any university.

To the best of my knowledge and belief, it does not contain any material previously published or written by another person, except where due reference is made in the text.

Haofeng Lu

October 2016

For mum,

for your endless love.

Acknowledgement

I am very fortunate to have my PhD research carried out at the Department of Electronic Materials Engineering (EME), the Australian National University (ANU) during my first several years in Canberra. The memorable experience gives me great impression of Australia and makes me love this country.

Firstly, I would like to acknowledge my principal supervisors, A/Prof. Lan Fu and Prof. Chennupati Jagadish, for their great support, encouragement and guidance throughout my PhD. As the Chair of my supervisory panel, A/Prof. Lan Fu has been involved in almost all aspects of my PhD project and providing guidance whenever needed. Prof. Jagadish is always patient with the students and looks after us like a father despite of his tight travel schedules. I am honoured to be one of the members in Prof. Jagadish's research group at the ANU.

A big thank you to Prof. Hoe Tan as a very important supervisor. He has trained me on MOCVD system and many other types of equipment. Prof. Tan is always the first person to call for laboratory issues. I could not imagine what we could achieve without him. He is also a good "mentor" on Australian red wines.

Dr. Michael Gao deserves very special thanks. He is the first person I met from EME, who picked me up from the Canberra airport on a sunny day and introduced me to the ANU. He also helped me find a place to live in the first few days. I am also grateful to Dr. Wen Lei for his advice on experimental designs and Dr. Jenny Wong-Leung, who has guided and helped me with the TEM analysis and sample preparation. For the FDTD simulation, I am deeply grateful to Dr. Sudha Mokkapati. She taught me simulations on plasmonic structures.

Dr. Greg Jolley is an expert on quantum well/dot device characterization and theoretical calculation. He provided excellent support in the first year of my PhD, and remained as an excellent collaborator after he moved to Perth. It was also a great pleasure working with Dr. Ian McKerracher, who helped me a lot with device fabrication and mask design. I would like to thank Drs. Patrick Parkinson and Qing Li, who graciously shared their expertise on optical spectroscopy experiments. In addition, I

thank Dr. Rongping Wang from the Department of Laser Physics for his guidance on thin-film reflectance measurements.

The Australian National Fabrication Facility (ANFF) ACT node has provided important facility support for my research. I would like to thank Drs. Fouad Karouta, Kaushal Vora and Jie Tian from ANFF, as well as Michael Aggett, David Llewellyn, Craig Saint, Tom Kitchen and Dr. Kidane Belay from EME for their technical support. I am also very grateful to all the administrative staff for their continuing support, especially Liz Micallef, Liudmila Mangos, Heeok Kyung, Julie Arnold, Karen Scholte and Karen Nulty.

I also appreciate the support from other colleagues and good friends. Dr. Danyu Liu and Dr. Xin Gai helped me with some theoretical aspects of my project. More importantly, we spent spare time together to share tasty food and jokes. I also thank Dr. Ziyuan Li for her help when we shared the same office. I am also grateful to Dr. Mykhaylo Lysevych, Dr. Sup Charnvanichborikarn, Dr. Jordan Kang, Nian Jiang, Qian Gao, Zhe Li, Bijun Zhao, and my office neighbours Dr. Boshra Afra, Dr. Bimo Bayu Aji, Timothy Burgess - you make EME such a great place to stay.

In 2012, I visited the Rochester Institute of Technology where I was warmly hosted by Prof. Seth Hubbard's research group. I would particularly like to thank Prof. Hubbard and Yushuai Dai for their kind help and discussions regarding quantum dot solar cell characterization. I also visited Prof. Diana L. Huffaker's group at the University of California, Los Angeles. I am grateful to Dr. Baolai Liang and Dr. Ramesh B. Laghumavarapu for their hospitality to show me the equipment and discuss their research.

I also wish to thank our collaborators at the University of Maryland: Prof. Mario Dagenais and Dr. Tian Li. It has been a great pleasure collaborating with you.

Finally, I would like to thank my family: Mum and Dad, my wife, my uncles and aunties, my grandparents, and also my cousins. Your unconditional love and support help me through the most difficult times. I love you all.

Abstract

Along with the ongoing research and industry development to reduce the cost of conventional PV devices such as Si-based solar cells, significant research efforts have been focused on exploring new concepts and approaches for high efficiency III-V compound semiconductor solar cells, especially through the fast emerging nanotechnology to exploit the unique properties of nanostructures such as self-assembled quantum dots (QDs).

By incorporating self-assembled QDs into the intrinsic region of a standard p-i-n solar cell structure during the epitaxial growth, photons in the solar spectrum with energy lower than the energy gap of the host material can be absorbed by the QD layers, leading to an extended photoresponse to longer wavelengths and hence larger photocurrent. In addition, the size and composition of the QDs can be varied and thereby allowing the bandgap to be tuned for absorption in different regime of the solar spectrum. However, due to the small QD absorption cross section, the increase of photocurrent in QDSCs is not significant and always accompanied with some reduction in other device characteristics such as the open circuit voltage and fill factor.

In this thesis, self-assembled $In_{0.5}Ga_{0.5}As$/GaAs QDSCs have been designed, fabricated, characterized and investigated in comparison with conventional GaAs p-i-n solar cells. The properties and fundamental mechanisms behind their complicated photoelectrical behaviours were analysed and understood. Several approaches were proposed and carried out to improve the device performance of QDSCs, either during the epitaxial growth process or after the growth and fabrication of the solar cells.

Stacking more QD layers is supposed to enhance the total volume of QD material and hence the light absorption. We carried out experiments to grow QDSC structures with increased number of QD layers. However, much reduced photocurrent and conversion efficiency for 15 and 20-layer samples were observed, which could be due to low carrier extraction efficiency and strain-induced defects. In order to improve the carrier extraction efficiency and consequently more enhanced photocurrent, modulation doping has been introduced into QDs layers to partially populate the confined states with electrons. The modulation doping has been found to be effective to improve carrier

transport and collection efficiency, leading to an enhancement of the external quantum efficiency over the whole solar cell response range and thus the conversion efficiency.

We have also taken two different post-growth approaches to improve the QDSC efficiency, namely the rapid thermal annealing and surface plasmonic light trapping. Firstly, QDSCs with different layers were annealed at various temperatures between 700 and 850 °C with the device annealed at the highest temperature of 850 °C displayed the highest efficiency increase of 41.42 % from 10.26 % to 14.51 %, compared to the as-grown sample. Secondly, it was found that a combination of 120 nm diameter hemispherical Ag nanoparticle and a 5 nm thick TiO_2 dielectric film pre-deposited on the back of the GaAs substrate was the optimum light trapping configuration for our QDSC. The QDSC spectral response was improved by 35.7% over the 900 nm- 1200 nm wavelength range, leading to enhancements in both J_{sc} and V_{oc} and an overall efficiency enhancement of 7.6 % compared to the reference QD solar cell.

Publications

Journal papers

[1] T. Li, H.F. Lu, L. Fu, H.H. Tan, C. Jagadish, and M. Dagenais, Enhanced carrier collection efficiency and reduced quantum state absorption by electron doping in self-assembled quantum dot solar cells. Applied Physics Letters, 2015. 106(5): pp. 053902.

[2] G. Jolley, L. Faraone, L. Fu, H.F. Lu, H.H. Tan, and C. Jagadish, A study of quantum well solar cell structures with bound-to-continuum transitions for reduced carrier recombination. Applied Physics Letters, 2013. 102(21): pp. 213903.

[3] G. Jolley, L. Fu, H.F. Lu, H.H. Tan, and C. Jagadish, The role of intersubband optical transitions on the electrical properties of InGaAs/GaAs quantum dot solar cells. Progress in Photovoltaics: Research and Applications, 2013. 21(4): pp. 736-746.

[4] H.F. Lu, S. Mokkapati, L. Fu, G. Jolley, H.H. Tan, and C. Jagadish, Plasmonic quantum dot solar cells for enhanced infrared response. Applied Physics Letters, 2012. 100(10): pp. 103505.

[5] H.Y. Xu, Y.N. Guo, W. Sun, Z.M. Liao, T. Burgess, H.F. Lu, Q. Gao, H. Tan, C. Jagadish, and J. Zou, Quantitative study of GaAs nanowires catalyzed by Au film of different thicknesses. Nanoscale Research Letters, 2012. 7(1): pp. 589.

[6] H.F. Lu, L. Fu, J. Greg, T. Hark Hoe, T. Sudersena Rao, and J. Chennupati, Temperature dependence of dark current properties of InGaAs/GaAs quantum dot solar cells. Applied Physics Letters, 2011. 98(18): pp. 183509.

[7] G. Jolley, H.F. Lu, L. Fu, H.H. Tan, and C. Jagadish, Electron-hole recombination properties of $In_{0.5}Ga_{0.5}As$/GaAs quantum dot solar cells and the influence on the open circuit voltage. Applied Physics Letters, 2010. 97(12): pp. 123505.

Conference papers

[1] H.F. Lu, L. Fu, G. Jolley, H.H. Tan, and C. Jagadish, Improved performance of InGaAs/GaAs Quantum Dot Solar Cells using Si-modulation doping, in Conference on Optoelectronic and Microelectronic Materials and Devices (COMMAD). 2012, IEEE: Melbourne. pp. 127-128.

[2] S. Mokkapati, H.F. Lu, S. Turner, L. Fu, H.H. Tan, C. Jagadish, Plasmonics for III-V semiconductor solar cells, in 2012 IEEE Photonics Conference (Ipc). 2012. pp. 56-57.

[3] L. Fu, H.F. Lu, S. Mokkapati, G. Jolley, H.H. Tan, C. Jagadish, Plasmonic light trapping effect on properties of InGaAs/GaAs quantum dot solar cells, in IEEE Photonics Conference (Pho). 2011. pp. 387-388.

[4] L. Fu, G. Jolley, H.F. Lu, A. Majid, H.H. Tan, and C. Jagadish, Temperature effect on device characteristics of InGaAs/GaAs quantum dot solar cell, in 23rd Annual Meeting of the IEEE Photonics Society. 2010, IEEE: New York. pp. 716-717.

[5] H.F. Lu, L. Fu, G. Jolley, H.H. Tan, S.R. Tatavarti, and C. Jagadish, Temperature dependence of dark current properties of In-GaAs/GaAs quantum dot solar cells, in Conference on Optoelectronic and Microelectronic Materials and Devices (COMMAD). 2010, IEEE: Canberra. pp. 127-128.

[6] L. Fu, G. Jolley, S. Mokkapati, A. Majid, H.F. Lu, H.H. Tan, and C. Jagadish, III-V quantum dots for optoelectronic device applications, in 4th International Conference on Computers and Devices for Communication. 2009, IEEE: New York. pp. 468-468.

List of Figures

List of Tables

List of acronyms and Symbols

E_a	activation energy
AsH_3	arsine
k_B	boltzmann constant
V_{bi}	built-in electric field
DMZn	dimethylzinc
η	efficiency
EL	electroluminescence
EQE	external quantum efficiency
FF	fill factor
FDTD	finite-difference time-domain
FIB	focused ion beam
FWHM	full width at half maximum
n	ideality factor
LED	light-emitting diodes
MBE	molecular beam epitaxy
MOCVD	metalorganic chemical vapour deposition
V_{oc}	open-circuit voltage
PL	photoluminescence
RF	radio frequency
J_0	reverse saturation current density
R_s	series resistance
R_{sh}	shunt resistance
J_{sc}	short-circuit current density
SEM	scanning electron microscopy
STEM	scanning transmission electron microscopy

SiH_4	silane
TEM	transmission electron microscopy
$Al(CH_3)_3$, TMAl	trimethylaluminium
$Ga(CH_3)_3$, TMGa	trimethylgallium
$In(CH_3)_3$, TMIn	trimethylindium

Table of contents

Chapter 1

Introduction and background

1.1 Introduction

The current global energy challenges include energy security and excessive greenhouse gas emissions resulting from increasing energy consumption, mostly of fossil fuels. Under such pressure, the development of clean energy sources becomes an imperative task globally leading to ever increasing amount of investment as well as intensive research and development efforts. One of the abundant clean energy sources is solar energy, which has been developed as one of the most viable options to meet the global clean energy demand. The sun continuously delivers to the earth with an energy of 120,000 TW which theoretically well exceeds our current energy needs. For example, covering only ~ 0.1% of the earth's surface with solar cells of 10% efficiency would satisfy the current total energy demand in the world [1, 2]. However, the large-scale use of solar energy has not been achieved due to the relatively high cost and inadequate efficiency of existing photovoltaic (PV) technologies. Consequently, a great deal of research activities has been devoted to developing solar cells with better performance and lower cost in the past decades.

To date, three generations of photovoltaic devices have been developed. The majority of solar modules/cells on the market are single junction silicon devices known as the first generation solar cells. Thermodynamic limits for their energy conversion efficiency are between 31% and 40.7% depending on the concentration of incident solar illumination. This is known as the Shockley-Queisser (SQ) limit that was established in 1961 [3, 4]. Another much smaller but rapidly growing part of the PV market focuses on thin film designs are called the second generation solar cells. For example, devices based on amorphous silicon (a-Si), (indium) gallium arsenide (GaAs or InGaAs), cadmium telluride (CdTe) and copper indium (gallium) diselenide (CIS or CIGS) are typical 2nd generation solar cells, which also follow the efficiency restrictions as conventional Si cells but some of them with lower cost for unit device [5-8]. Nonetheless, they suffer from higher non-radiative recombination losses mainly due to lower film quality. The third generation PVs are designed to combine the advantages of both the first and second generation devices. Attempts have been made to improve the

efficiency of solar cells above the Shockley-Queisser limit through various methods and approaches such as multi-junction and intermediate-band solar cells, quantum structured cells, dye-sensitized solar cells, hot carrier cells and multi-exciton solar cells etc. [2, 7, 9-18].

1.1.1 Solar spectrum

The surface of the sun is called the photosphere, which is at a temperature of about 6000 K and can be treated as a blackbody. So the 6000 K blackbody spectrum is commonly used in detailed balance calculations, but temperatures of 5730 ± 90 K have also been proposed as a more accurate value to the sun's spectrum [19].

The solar radiation outside the earth's atmosphere is calculated based on the radiant power density at the sun's surface (5.961×10^7 W/m^2), the radius of the sun, and the distance between the earth and the sun. The calculated solar irradiance at top of the Earth's atmosphere is around 1.36 kW/m^2.

Before reaching the earth, all the sun radiation passes through the atmosphere, gases, dust and aerosols, which modify the spectrum by absorption or scattering. Specific gases, such as ozone (O_3), carbon dioxide (CO_2), and water vapour (H_2O), have very high absorption of photons that have energies close to the bond energies of these atmospheric gases. These absorption yields deep valleys in the spectral radiation curve at ground or sea level as shown in Figure 1.1.

The Air Mass (AM) is the path length which light passes through the atmosphere normalized to the shortest possible path length (that is, when the sun is directly overhead). The Air Mass quantifies the reduction in the power of light as it passes through the atmosphere layer. The Air Mass is defined as:

$$\mathrm{AM} = 1/\cos(\theta) \tag{1.1}$$

where θ is the angle of incident light from the vertical direction. For example, when the sun is directly overhead, the Air Mass equals to 1.

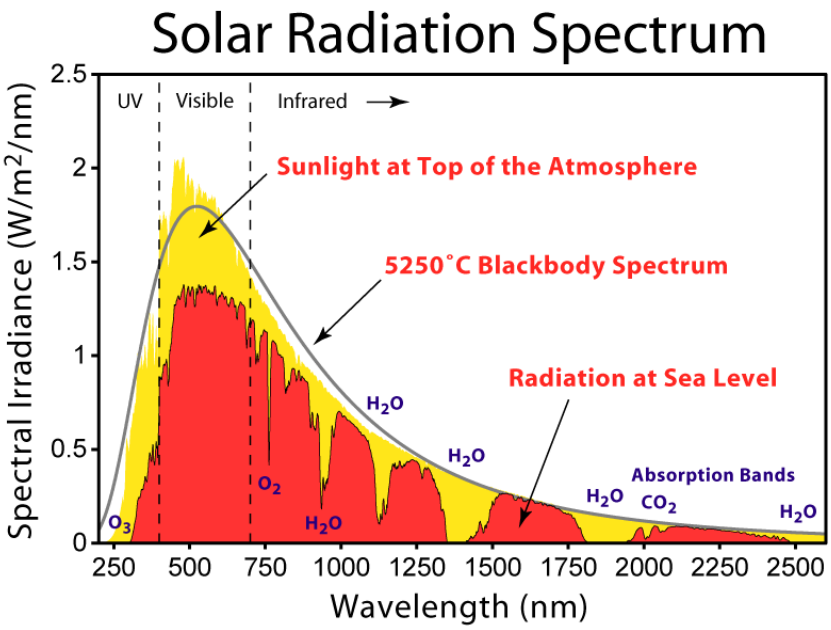

Figure 1.1: Solar spectrum above atmosphere and at the earth surface, which is also compared to the spectrum of a 5250 ℃ (5523 K) blackbody [20].

With the sun is overhead, direct radiation that reaches the ground passes straight through the entire atmosphere (all of the air mass). This radiation is called 'Air Mass 1 Direct' (AM 1D) radiation, and for standardization purposes a sea level reference site is normally used. The standard spectrum at the Earth's surface is called AM1.5G, (the G stands for global and includes both direct and diffuse radiation) or AM1.5D (which includes direct radiation only). The intensity of AM1.5D radiation can be approximated by reducing the AM0 (solar radiation outside the Earth's atmosphere) spectrum by 28% (18% due to absorption and 10% to scattering). The global spectrum is 10% higher than the direct spectrum, these calculations give approximately 970 W/m^2 for AM1.5G. However, the standard AM1.5G spectrum is normalized to give 1 kW/m^2 for convenience and the fact that there are inherent variations in incident solar radiation.

For the standard solar cell performance tests performed in this thesis, a Newport (Oriel) 91160 Solar Simulator (150 W) was used, which uses filters to duplicate spectra corresponding to Air Mass 1.5G. For more details, please refer to Chapter 2.

1.1.2 Principle of semiconductor solar cells

Irrespective of the types of solar cells, most of the p-n junction based semiconductor devices share a similar operation principle behind their behaviours. There are several key parameters that characterise the basic properties of solar cells. They are very important for the understanding and investigation of the solar cell device characteristics and performance. Such properties are briefly defined and introduced in this section and more detailed analysis will be presented in the following Chapters.

A solar cell is an optoelectronic device which directly converts sunlight into electricity. Light illuminates on the solar cell and produces both a current and a voltage to generate electric power. This process requires firstly, a material in which the absorption of light raises electrons to a higher energy state, and secondly, the movement of these higher energy electrons from the solar cell into an external circuit. A variety of materials and processes can potentially satisfy the requirements for photovoltaic energy conversion, but in practice nearly all photovoltaic energy conversion uses semiconductor materials based on a p-n junction.

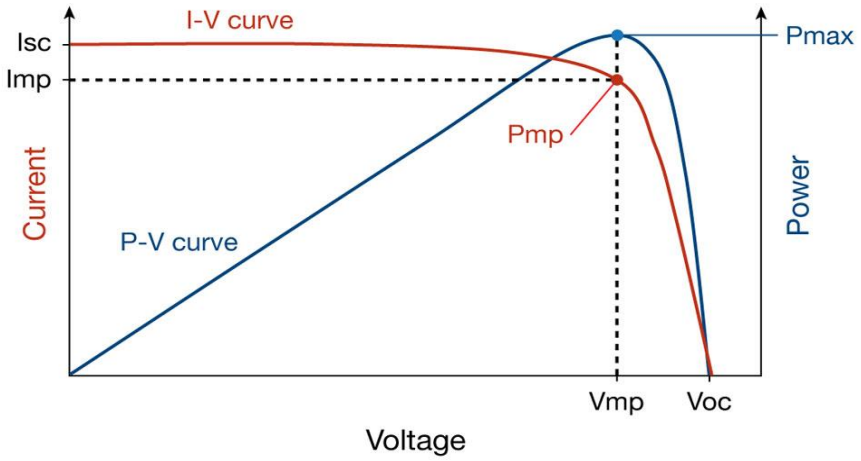

Figure 1.2: The typical solar cell I-V (red) and power output versus voltage (blue) curves. The key parameters for this plot are shown in the diagram [21].

The normal current-voltage (I-V) curve, power-voltage (P-V) curve, and key indicators for a solar cell are shown in Figure 1.2. Short-circuit current (I_{sc}) is the current through the solar cell (p-n junction) when the voltage across the device is zero (i.e., when the solar cell is short circuited), with the short-circuit current density (unit area short-circuit current) being referred to as J_{sc}. J_{sc} is dependent on the generation and actual collection amount of photo-generated carriers. For an

ideal solar cell, the short-circuit current and the photo-generated current are identical, therefore, it is the largest current which may be extracted from the cell. The open-circuit voltage (V_{oc}) is the maximum voltage from a solar cell, which only occurs at zero current. The open-circuit voltage corresponds to the amount of forward bias on solar cell when the dark current (I_{dark}) and photocurrent exactly cancel out. Although I_{sc} and V_{oc} are the maximum current and voltage value respectively from a solar device, at both of these operating points, the power output from the solar cell is zero. In Figure 1.2, it can be seen that there is a point, from which the maximum power output is obtained (P_{max}). The fill factor (FF) is the parameter which determines the maximum power from a solar cell [21]. It is defined as the ratio of the maximum power from the solar cell to the product of V_{oc} and I_{sc}, thus larger fill factor is desired for achieving high performance solar cells.

For the ideal diode, the V_{oc} follows the equation [21],

$$V_{oc} = \frac{k_B T}{q} \ln\left(\frac{J_{sc}}{J_0} + 1\right) \tag{1.2}$$

where J_0 is a constant (reverse saturation current density), q is the elementary charge of 1.6×10^{-19} Coulombs, k_B is the Boltzmann's constant 1.38×10^{-23} J/K, and T is temperature (in Kelvin).

When the solar cell (p-n junction) is connected to a load or forward biased between two terminals, a current will flow in the opposite direction to the photo-generated current, and the net current will be reduced from its I_{sc}. This reverse current is called the dark current. Most solar cells behave like a diode in the dark condition, exhibiting a much larger current under forward bias than reverse bias. Its density follows the equation (1.3) [21]:

$$J_{dark}(V) = J_0(e^{qV/k_B T} - 1) \tag{1.3}$$

The overall current extracted from solar cell can be seen as the sum of the short-circuit photocurrent and the dark current, which is known as the superposition approximation [21]. So the net current density through the solar cell is:

$$J(V) = J_{sc} - J_{dark}(V) \tag{1.4}$$

In reality, the actual dependence of J_{dark} on V is modified by an ideality factor n in the non-ideal diode equation [21],

$$J_{dark}(V) = J_0(e^{qV/nk_B T} - 1) \tag{1.5}$$

Ideality factor n varies between 1 and 2, and the reasons for this behaviour will be discussed in Chapter 3. Besides, for real solar cells, power can be dissipated through the resistance of the contacts and by leakage currents around the sides of the device. These effects can be represented as series (R_s) and shunt (R_{sh}) resistances in an equivalent circuit as shown in Figure 1.3. The series resistance arises from the resistance of the cell material to current flow, particularly through the surface to the metal contacts and between contacts. Series resistance is a problem for the high current density devices. The shunt (parallel) resistance arises from current leakage through the cell, around the edges of the device and between contacts of different polarities. For an efficient cell, we expect R_s to be as small as possible and R_{sh} to be as large as possible.

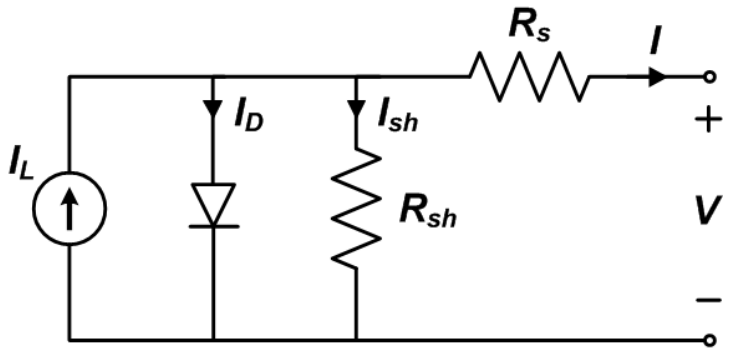

Figure 1.3: Equivalent circuit of a typical solar cell [21].

The efficiency η of a solar cell is determined as the fraction of incident power which is converted to electricity and is defined as:

$$\eta = {V_{OC}\, I_{SC}\, FF}/{P_{in}} \qquad (1.6)$$

Where V_{OC} is the open-circuit voltage, I_{SC} is the short-circuit current, FF is the fill factor and P_{in} is the incident power. For efficiency calculations under the 1 Sun@ AM1.5G condition with power density of 1 kW/m^2 or 100 mW/cm^2, the input power is determined by the area of solar cells.

1.1.3 External quantum efficiency

The external quantum efficiency (EQE) is the ratio of the number of carriers collected from the solar cell to the number of photons of a given energy incident

on the solar cell. The quantum efficiency for photons with energy below the materials band gap is zero [21]. Ideally, quantum efficiency should have the square shape with respect to wavelength with a value of 1 (i.e. 100 %). But QE for most real solar cells is degraded due to various loss mechanisms. For example, front surface recombination affects carriers generated near the surface, and since short wavelength light is absorbed very close to the surface, high front surface recombination will reduce the quantum efficiency at short wavelengths. Similarly, the long wavelength efficiency is decreased by low absorption coefficient, small carrier diffusion length and rear surface recombination. For light that is absorbed in the bulk of a solar cell, the low diffusion length and possible defects will affect the collection probability from the bulk and reduce the quantum efficiency.

The EQE of a solar cell includes the effect of optical losses such as transmission and surface reflection. It is also necessary to look at the quantum efficiency calculated based on light absorbed after all types of losses. Internal quantum efficiency (IQE) is the ratio of the number of generated carriers collected by the solar cell to the number of photons absorbed by the cell. By measuring the reflection and transmission of a device, the external quantum efficiency value can be corrected to obtain the internal quantum efficiency curve.

1.1.4 III-V compound semiconductor solar cells

The III-V compound semiconductors have been widely used in lasers, photodetectors, and solar cells etc. [22-27]. Among all types of solar cells and modules in both research and industry applications, III-V compound semiconductors are the most efficient solar cell materials [28-30], mainly due to their direct bandgap, high carrier mobility and good temperature stability. III-V multi-junction solar cells were initially developed for powering satellites in space and are now starting to be explored for terrestrial applications through the use of concentrator systems. Concentrators based on III-V solar cells is one of the most promising technologies for dramatically reducing the cost of PV electricity [31]. Extensive development of demonstration projects and commercial prototypes have taken place in the last few years [26, 32]. Concentrator III-V solar cells present a potential opportunity for large scale solar energy technology in the future.

The record efficiency reported for a concentrator cell to date is 46.0% for the GaInP/GaAs and GaInAsP/GaInAs multi-junction cell from Soitec/CEA/FhG-ISE tested under 508 suns condition [29]. GaAs solar cells have also held the

single junction device world record for the past two decades, with the latest efficiency records being 28.8% at AM 1.5G and 29.1% at 117 suns [29]. However, with an energy gap of 1.42 eV, GaAs has a band gap that is higher than the optimum value of 1.1 eV for the AM 1.5D spectrum under concentration [33]. In addition, there are no lower band gap lattice-matched binaries or ternary alloys in a GaAs based multi-junction cells. Therefore, it is important to lower the band gap for terrestrial applications of GaAs based single and multi-junction solar cells. One approach to addressing this problem is to grow slightly strained quantum structures that have lower band gap into the bulk GaAs solar cell in order to harvest more of the long wavelength photons from the solar spectrum.

1.2 GaAs solar cells with quantum structures

1.2.1 Motivation

Nanostructured materials such as the ones employing low dimensional epitaxial structures have offered new opportunities to design more efficient solar cells. These low dimensional structures, including quantum wells (2 dimensions), nanowires or nanotubes (1 dimension) and quantum dots (0 dimension), present great potential to improve efficiencies of solar cells by facilitating photon absorption and carrier collection [9, 10, 15, 17, 34-37].

Figure 1.4 shows the effect of reduced materials dimension on their density of states. In the case of a bulk material, the density of states is a continuous function of energy (Figure 1.4 (a)), which means that photo-generated carriers will spread over a wide 3D range. However, in the case of quantum wells, the carriers are confined in the growth direction, and can only move within a 2D plane. Furthermore, 0D quantum dots provide further carrier confinement, and will be able to restrict the carriers in all three directions as can be seen in Figure 1.4 (c). Incorporation of quantum dots results in the formation of discrete energy levels inside the bulk materials. This modifies the density of states, leading to an increase in carrier density at energies near the band edge and greater thermal stability, which is promising for high performance optoelectronic devices including solar cells. Besides, these quantum structures also offer the flexibility in bandgap engineering by tuning the material composition and the dimension/size of the quantum structures.

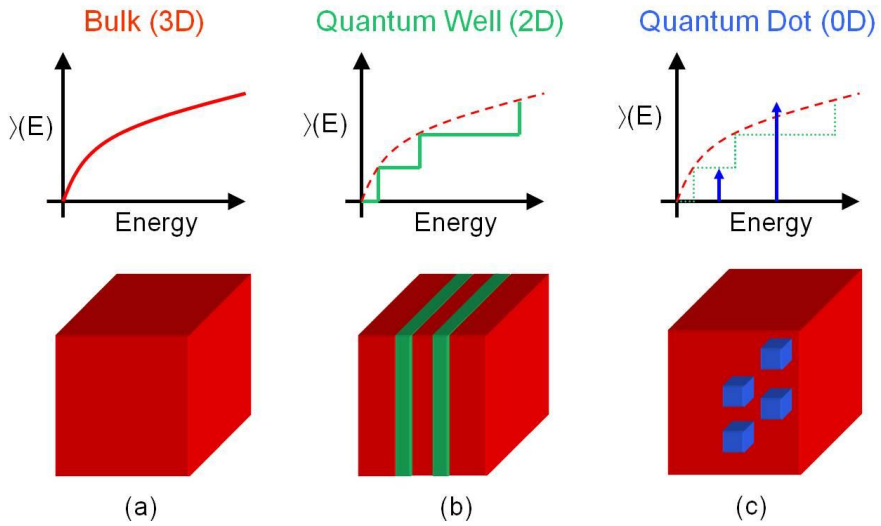

Figure 1.4: Schematic illustrating the density of states within (a) bulk material, and the effect of quantisation on states density in (b) quantum wells, and (c) quantum dots [38].

As mentioned in section 1.1.3, the band gap of GaAs restricts the utilization of wider range of solar irradiation. In order to make better use of low energy photons (less than the bandgap of GaAs) of the solar spectrum, low dimensional quantum structures have been introduced into GaAs p-i-n structures, such as (In)GaAs quantum wells (QWs) [39, 40] and different self-assembled quantum dots (QDs) systems [41-44]. Early studies indicate that incorporating QDs into the intrinsic region of a p-i-n solar cells can indeed extend their photoresponse to the longer wavelength range, leading to a slightly increased short circuit current density [10, 45-47]. This thesis aims to achieve a deeper understanding of quantum dot solar cell (QDSC) operation as well as designing new structures/post-treatment to improve device performance.

1.2.2 Quantum dot growth

Quantum dots can be grown by a number of epitaxial growth techniques such as chemical beam epitaxy (CBE), molecular beam epitaxy (MBE) and metal organic chemical vapour deposition (MOCVD) [48-51]. Among them, MBE provides precise control of the growth and crystalline quality because of the cleanliness of the growth environment and the availability of advanced in-situ monitoring techniques such as RHEED, but the growth rate is relatively low for the thickness of materials required by most devices [49, 52]. On the other hand, MOCVD has

higher growth rate and the ability to be scaled up to achieve large-scale production, which is preferred by the industry applications.

The self-assembled growth of QDs relies on the strain arising from the lattice mismatch between the substrate and the deposited layer. Normally, the epitaxial deposition on a substrate may proceed by three different modes [53, 54]. These modes are determined by the interface energy as well as strain, as illustrated in Figure 1.5. For the growth of material on lattice matched substrate, referred to as Frank-Van Der Merwe (FM) growth, the growth adatoms attraction force by the substrate surface is stronger than the force they attract each other. Furthermore, the adjoining atoms are not under any strain disturbance due to their matched lattice constant with the substrate. In this case deposited top layer completely covers the substrate in a layer by layer mode. The second growth mode is called the Volmer-Weber (VW) growth occurring for the material with large lattice constant than the substrate. The surface energy of the substrate is lower than the energy between the two materials. When adatoms attach on the substrate surface, the incoming atoms have higher probability to stick to the existing atoms forming islands rather than planar growth. Additionally, there is an intermediate case, which is called the Stranski-Krastanow (S-K) growth (Figure 1.5 (c)). It occurs when there is a small lattice constant difference between the depositing material and the substrate. The growth starts with layer-by-layer mode first and as the deposited layer becomes thicker (the threshold thickness is determined by the lattice mismatch between the layer and the substrate), the accumulated strain changes the growth from 2-dimensional growth to 3-dimensional growth leading to the formation of quantum dots [55]. Due to the self-organized nature of the process, QDs grown through the S-K mode is also called self-organized or self-assembled quantum dots, and the thin 2D layer formed below the 3D QDs is called the wetting layer (WL). This is the mechanism under which quantum dot solar cells in this thesis were grown.

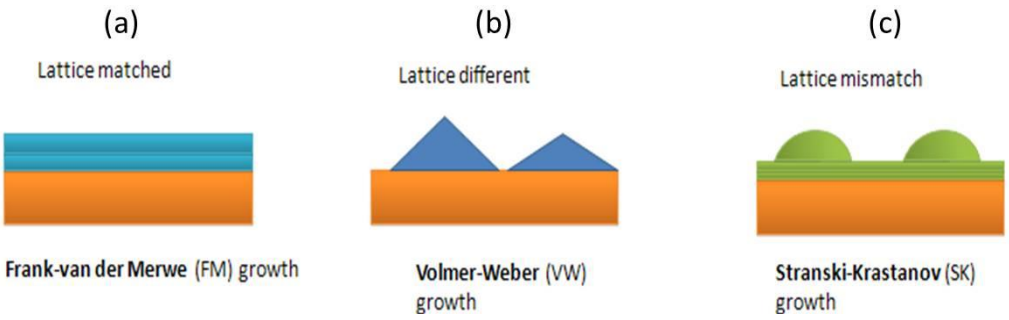

Figure 1.5: Three growth modes: (a) Frank van der Merwe (layer-by-layer), (b) Volmer-Weber (direct islanding), (c) Stranski-Krastanow (self-assembled) growth [20].

For example, InAs has a lattice mismatch of 7.2% with GaAs. After a few monolayers of growth, the deposition changes from layer-by-layer (two dimensional growth) to island growth (three dimensional). For InAs quantum dots this occurs after 1.7 monolayer (ML) of deposition [56, 57], for $In_{0.5}Ga_{0.5}As$ dots it occurs around 4 ML [58]. It has been shown that these islands are the minimum surface energy form for the strained layers [16] and they can be formed without any dislocations [59].

However, for the growth of self-assembled quantum dots, there are two main challenges [51, 60]. First, growth kinetics play a much greater role which results in a fast nucleation process and an increased tendency to form incoherent islands. This is partly due to the higher growth temperatures used in the MOCVD reactor (50-100 ℃ higher than that of MBE) to ensure enough pyrolysis of the precursor molecules. Furthermore, the use of in-situ monitoring techniques in MOCVD is limited, making it difficult to precise control the dot formation.

1.2.3 Concept of intermediate band solar cell

A solar cell device with an intermediate electronic band located within the conventional semiconductor p-n junction, is referred to as intermediate band solar cell (IBSC), which has been proposed as a better utilization of the solar spectrum [15, 61] involving absorption of sub-bandgap photons. The performance of solar cells with multiple photo-induced transitions was explained by Wolf in 1960, and the possibility of surpassing single-junction solar cells was also discussed [62]. More recent theoretical studies of IBSC have predicted potential efficiencies of 63.2 % under full concentration condition for ideal intermediate band solar cells [3, 4, 15, 63], compared with the Shockley-Queisser limit of 40.7% for a

conventional single junction device under the same illumination condition. In Figure 1.6, a band diagram of the ideal IBSC is illustrated. Apart from the usual semiconductor conduction band (CB) and valence band (VB), it also contains an intermediate band (IB). Consequently, in addition to the electron transition between the VB and the CB (process 3 in Figure 1.6), photo-induced transitions from VB to IB (process 1), and IB to CB (process 2) can also take place.

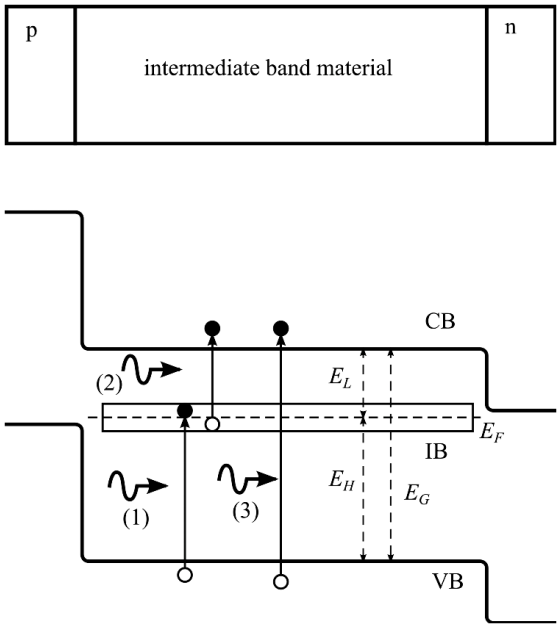

Figure 1.6: Schematic of the band structure of an intermediate band material within a p-n junction, showing the conduction band (CB), valence band (VB), and the intermediate band (IB). Three transitions induced by different energy photons are also shown [42].

Such structure can be realized possibly by several different approaches such as low dimensional superlattices, impurities, etc., although some of them may not strictly comply with the required conditions [64-68]. The use of quantum dots for the implementation of IBSC has also been proposed [10, 69], and many experimental and theoretical studies of quantum dot solar cells (QDSCs) have been reported [10, 15, 69-71]. Based on the ideal theoretical model of IBSC, when QD layers are incorporated into the intrinsic region of a p-i-n cell, the built-in potential should still be determined by the Fermi-level splitting of the doped emitter and base layers, as is the case for single junction GaAs solar cells. Therefore, it is possible for a QDSC to maintain a similar open-circuit voltage to the single-junction cell but to show an improved short-circuit current due to the extra contribution from the sub-bandgap quantum dot structures. However,

QD/wetting layer structures influence not only absorption but also recombination and transport of carriers in the intrinsic region, which tends to affect the V_{oc} of the whole solar cell [72, 73]. Furthermore, the strong QD confinement effect increases the carrier recombination possibility and thus restricts the total amount of photocurrent. Almost all the reported studies on QDSCs show the efficiency less than that of the reference GaAs cells. Although improvements in the short-circuit current have been demonstrated [41, 71, 73, 74], similar to the case of quantum well solar cells [75], the V_{oc} is still degraded by the inclusion of sub-bandgap quantum structures. This, together with small light absorption of the QDs/ WL (for a limited increase of short-circuit current), indicate that most of the real QDSCs do not meet the assumptions of theoretical models [10, 15, 63, 69] for QDSCs from exhibiting overall efficiency improvement. These possible effects will be studied in detail in this thesis to investigate the operation of intermediate band solar cells based on quantum dot structures.

1.3 Outline of the thesis

Overall, the topics of this thesis cover the basic concepts, operation principles, and the fundamental properties of InGaAs/GaAs quantum dot solar cells. **Chapter 1** as an introduction briefly presents some of the important concepts and background literature in this area. The thesis investigates four different approaches to enhance solar cell performance with the incorporation of quantum dots.

Chapter 2 presents the basic explanation of all experimental techniques used in this work. The growth of the quantum dot structures was achieved by metal organic chemical vapour deposition. The entire solar cell device fabrication processes is also described. Main characterization techniques such as atomic force microscopy, transmission electron microscopy, photoluminescence, and electroluminescence are described. Other device testing/analysis techniques such as I-V characterization, photoresponse, quantum efficiency measurement are also briefly explained.

Due to the accumulation of strain and the tendency to form dislocations, the growth conditions are carefully controlled to achieve high density and defect-free $In_{0.5}Ga_{0.5}As$ QD/WL structures within a GaAs p-i-n structure as presented in **Chapter 3**. Extensive and profound understanding of the unique QDSC behaviours are obtained based on a thorough investigation of the device dark

current, photo-generated carriers capture, recombination and transport properties. In addition, stacking more QD layers is aimed to increase the total optical absorption. Investigation on the effect of QD stacking number on devices performance are carried out in this chapter.

Despite the increased short-circuit current obtained for QDSC compared to the GaAs control cell, the contribution from QDs is still limited by their relative low absorption cross-section and QD-related recombination. QDSCs are considered as a promising candidate for the implementation of intermediate band solar cell, which is based on two-photon absorption processes. However, considerable amount of recombination occurs in QD confined states making transport and collection of photo-generated carriers inefficient. To improve carrier transport and extraction efficiency by partially occupying the confined states, n-type modulation doping of QD layers is proposed and studied systematically in **Chapter 4**.

One major challenge in the growth of QDs is the accurate control of their size and shape through controlling the growth parameters such as growth pressure, temperature, precursor flow rate, and V/III ratio. Therefore, post-growth thermal annealing is investigated as an alternative approach to tailor the energy band structures and carrier confinement, which could consequently lead to improved device performance. **Chapter 5** reports the study of the effects of postgrowth thermal annealing on the optical and electrical characteristics of QDSCs with different number of QD layers. The fitting of Arrhenius plots shows the activation energy E_a that is related to the QD confinement is generally reduced due to the thermal inter-diffusion leading to enhanced devices performance by thermal annealing. The annealing induced dopant diffusion is also examined by SIMS measurements in this chapter.

In **Chapter 6**, we propose another post-growth approach to enhance the long wavelength (870-1180 nm) photon absorption in QDSC by employing light trapping effect promoted by Ag plasmonic nanoparticles. This is critical for the QD structures due to their very small (thinner than the absorption length of corresponding wavelength) physical thickness. Maximising the scattering cross-section (Q_{scat}) is expected to ensure nanoparticles interact with most of the incident light and randomise its direction. High coupling fraction of scattered light into the substrate (F_{sub}) is necessary to minimize reflection or transmission losses. Simulation using finite-difference time-domain method is conducted to optimize the Q_{scat}, F_{sub}, as well as the resonance peak frequency by modelling a

single nanoparticle on a thin layer of dielectric film to enhance absorption at the wetting layer/QD peak wavelength region.

Finally, conclusions from the entire thesis and some recommendations for future work are presented in **Chapter 7**.

References

[1] Crabtree, G.W. and N.S. Lewis, Solar energy conversion. *Physics Today*, 2007. **60**(3): pp. 37-42.

[2] Grätzel, M., Solar Energy Conversion by Dye-Sensitized Photovoltaic Cells. *Inorganic Chemistry*, 2005. **44**(20): pp. 6841-6851.

[3] Shockley, W. and H.J. Queisser, Detailed Balance Limit of Efficiency of P-N Junction Solar Cells. *Journal of Applied Physics*, 1961. **32**(3): pp. 510-519.

[4] Araújo, G.L. and A. Martí, Absolute limiting efficiencies for photovoltaic energy conversion. *Solar Energy Materials and Solar Cells*, 1994. **33**(2): pp. 213-240.

[5] Hamakawa, Y., Thin-film solar cells : next generation photovoltaics and its applications. 2004, Berlin: Springer.

[6] Bett, A.W., F. Dimroth, G. Stollwerck, and O.V. Sulima, III-V compounds for solar cell applications. *Applied Physics A*, 1999. **69**(2): pp. 119-129.

[7] Bett, A.W., R. Adelhelm, C. Agert, R. Beckert, F. Dimroth, and U. Schubert, Advanced III-V solar cell structures grown by MOVPE. *Solar Energy Materials and Solar Cells*, 2001. **66**(1-4): pp. 541-550.

[8] Vigil-Galan, O., M. Courel, J.A. Andrade-Arvizu, Y. Sanchez, M. Espindola-Rodriguez, E. Saucedo, D. Seuret-Jimenez, and M. Titsworth, Route towards low cost-high efficiency second generation solar cells: current status and perspectives. *Journal of Materials Science-Materials in Electronics*, 2015. **26**(8): pp. 5562-5573.

[9] Brown, G.F. and J. Wu, Third generation photovoltaics. *Laser & Photonics Reviews*, 2009. **3**(4): pp. 394-405.

[10] Aroutiounian, V., S. Petrosyan, A. Khachatryan, and K. Touryan, Quantum dot solar cells. *Journal of Applied Physics*, 2001. **89**(4): pp. 2268-2271.

[11] Barnham, K., I. Ballard, J. Barnes, J. Connolly, P. Griffin, B. Kluftinger, J. Nelson, E. Tsui, and A. Zachariou, Quantum well solar cells. *Applied Surface Science*, 1997. **114**: pp. 722-733.

[12] Blokhin, S.A., A.V. Sakharov, A.M. Nadtochy, A.S. Pauysov, M.V. Maximov, N.N. Ledentsov, A.R. Kovsh, S.S. Mikhrin, V.M. Lantratov, S.A. Mintairov, N.A. Kaluzhniy, and M.Z. Shvarts, AlGaAs/GaAs photovoltaic cells with an array of InGaAs QDs. *Semiconductors*, 2009. **43**(4): pp. 514-518.

[13] Fetzer, C.M., R.R. King, P.C. Colter, K.M. Edmondson, D.C. Law, A.P. Stavrides, H. Yoon, J.H. Ermer, M.J. Romero, and N.H. Karam, High-efficiency metamorphic GaInP/GaInAs/Ge solar cells grown by MOVPE. *Journal of Crystal Growth*, 2004. **261**(2-3): pp. 341-348.

[14] Geisz, J.F., S. Kurtz, M.W. Wanlass, J.S. Ward, A. Duda, D.J. Friedman, J.M. Olson, W.E. McMahon, T.E. Moriarty, and J.T. Kiehl, High-efficiency GaInP/GaAs/InGaAs triple-junction solar cells grown inverted with a metamorphic bottom junction. *Applied Physics Letters*, 2007. **91**(2): pp. 023502.

[15] Luque, A. and A. Marti, Increasing the efficiency of ideal solar cells by photon induced transitions at intermediate levels. *Physical Review Letters*, 1997. **78**(26): pp. 5014-5017.

[16] Luque, A., A. Marti, E. Antolin, and C. Tablero, Intermediate bands versus levels in non-radiative recombination. *Physica B-Condensed Matter*, 2006. **382**(1-2): pp. 320-327.

[17] Yu, K. and J. Chen, Enhancing Solar Cell Efficiencies through 1-D Nanostructures. *Nanoscale Research Letters*, 2009. **4**(1): pp. 1-10.

[18] Pan, J., L.Z. Wang, J.C. Yu, G. Liu, and H.M. Cheng, A nonstoichiometric SnO2-delta nanocrystal-based counter electrode for remarkably improving the performance of dye-sensitized solar cells. *Chemical Communications*, 2014. **50**(53): pp. 7020-7023.

[19] Hanasoge, S.M., T.L. Duvall, and K.R. Sreenivasan, Anomalously weak solar convection. *Proceedings of the National Academy of Sciences of the United States of America*, 2012. **109**(30): pp. 11928-11932.

[20] Available from: https://en.wikipedia.org.

[21] Nelson, J., The Physics of Solar Cells. 2005, London: Imperial College Press.

[22] Davis, R.F., III-V nitrides for electronic and optoelectronic applications. *Proceedings of the IEEE*, 1991. **79**(5): pp. 702-712.

[23] Mathine, D.L., The integration of III-V optoelectronics with silicon circuitry. *Selected Topics in Quantum Electronics, IEEE Journal of*, 1997. **3**(3): pp. 952-959.

[24] Xu, G.Y., A. Salvador, W. Kim, Z. Fan, C. Lu, H. Tang, H. Morkoç, G. Smith, M. Estes, B. Goldenberg, W. Yang, and S. Krishnankutty, High speed, low noise ultraviolet photodetectors based on GaN p-i-n and AlGaN(p)-GaN(i)-GaN(n)structures. *Applied Physics Letters*, 1997. **71**(15): pp. 2154-2156.

[25] Chau, R., S. Datta, and A. Majumdar. Opportunities and challenges of III-V nanoelectronics for future high-speed, low-power logic applications. in *Compound Semiconductor Integrated Circuit Symposium, 2005. CSIC '05. IEEE*. 2005.

[26] Yamaguchi, M., T. Takamoto, K. Araki, and N. Ekins-Daukes, Multi-junction III–V solar cells: current status and future potential. *Solar Energy*, 2005. **79**(1): pp. 78-85.

[27] Dimroth, F., High-efficiency solar cells from III-V compound semiconductors. *physica status solidi (c)*, 2006. **3**(3): pp. 373-379.

[28] Green, M.A., K. Emery, Y. Hishikawa, W. Warta, and E.D. Dunlop, Solar cell efficiency tables (version 43). *Progress in Photovoltaics: Research and Applications*, 2014. **22**(1): pp. 1-9.

[29] Green, M.A., K. Emery, Y. Hishikawa, W. Warta, and E.D. Dunlop, Solar cell efficiency tables (version 47). *Progress in Photovoltaics: Research and Applications*, 2016. **24**(1): pp. 3-11.

[30] Green, M.A., K. Emery, Y. Hishikawa, W. Warta, and E.D. Dunlop, Solar cell efficiency tables (version 46). *Progress in Photovoltaics: Research and Applications*, 2015. **23**(7): pp. 805-812.

[31] Yamaguchi, M. and A. Luque, High efficiency and high concentration in photovoltaics. *Electron Devices, IEEE Transactions on*, 1999. **46**(10): pp. 2139-2144.

[32] O'Neill, M.J., A.J. McDanal, and P.A. Jaster. Development of terrestrial concentrator modules using high-efficiency multi-junction solar cells. in *Photovoltaic Specialists Conference, 2002. Conference Record of the Twenty-Ninth IEEE*. 2002.

[33] Ward, J.S., M.W. Wanlass, K.A. Emery, and T.J. Coutts. GaInAsP solar cells with the ideal band gap for terrestrial concentrator applications. in *Photovoltaic Specialists Conference, 1993., Conference Record of the Twenty Third IEEE*. 1993.

[34] Barnham, K.W.J., I. Ballard, J.G. Connolly, N. Ekins-Daukes, B.G. Kluftinger, J. Nelson, C. Rohr, and M. Mazzer, Recent results on quantum well solar cells. *Journal of Materials Science-Materials in Electronics*, 2000. **11**(7): pp. 531-536.

[35] Barnham, K.W.J., I. Ballard, J.P. Connolly, N.J. Ekins-Daukes, B.G. Kluftinger, J. Nelson, and C. Rohr, Quantum well solar cells. *Physica E: Low-dimensional Systems and Nanostructures*, 2002. **14**(1–2): pp. 27-36.

[36] Barnham, K.W.J., B. Braun, J. Nelson, M. Paxman, C. Button, J.S. Roberts, and C.T. Foxon, Short-Circuit Current and Energy Efficiency Enhancement in a Low-Dimensional Structure Photovoltaic Device. *Applied Physics Letters*, 1991. **59**(1): pp. 135-137.

[37] Lu, H.F., S. Mokkapati, L. Fu, G. Jolley, H.H. Tan, and C. Jagadish, Plasmonic quantum dot solar cells for enhanced infrared response. *Applied Physics Letters*, 2012. **100**(10): pp. 103505.

[38] Piprek, J., Semiconductor Optoelectronic Devices. Semiconductor Optoelectronic Devices. 2003, Boston: Academic Press.

[39] Mazzer, M., K.W.J. Barnham, I.M. Ballard, A. Bessiere, A. Ioannides, D.C. Johnson, M.C. Lynch, T.N.D. Tibbits, J.S. Roberts, G. Hill, and C. Calder, Progress in quantum well solar cells. *Thin Solid Films*, 2006. **511**: pp. 76-83.

[40] Wu, L.Z., W. Tian, and X.T. Jiang, Investigation on the performances of multi-quantum barriers in a single quantum well solar cell. *Journal of Materials Science*, 2005. **40**(6): pp. 1451-1454.

[41] Hubbard, S.M., C.D. Cress, C.G. Bailey, R.P. Raffaelle, S.G. Bailey, and D.M. Wilt, Effect of strain compensation on quantum dot enhanced GaAs solar cells. *Applied Physics Letters*, 2008. **92**(12): pp. 123512.

[42] Luque, A. and A. Marti, The Intermediate Band Solar Cell: Progress Toward the Realization of an Attractive Concept. *Advanced Materials*, 2010. **22**(2): pp. 160-174.

[43] Zhou, D., G. Sharma, S.F. Thomassen, T.W. Reenaas, and B.O. Fimland, Optimization towards high density quantum dots for intermediate band solar cells grown by molecular beam epitaxy. *Applied Physics Letters*, 2010. **96**(6): pp. 061913.

[44] Zhuang, Q.D., H.X. Li, L. Pan, J.M. Li, M.Y. Kong, and L.Y. Lin, Self-organization of the InGaAs GaAs quantum dots superlattice. *Journal of Crystal Growth*, 1999. **201**: pp. 1161-1163.

[45] Antolin, E., A. Marti, C.R. Stanley, C.D. Fanner, E. Canovas, N. Lopez, P.G. Linares, and A. Luque, Low temperature characterization of the photocurrent produced by two-photon transitions in a quantum dot intermediate band solar cell. *Thin Solid Films*, 2008. **516**(20): pp. 6919-6923.

[46] Levy, M.Y. and C. Honsberg, Intraband absorption in solar cells with an intermediate band. *Journal of Applied Physics*, 2008. **104**(11): pp. 113103.

[47] Marti, A., E. Antolin, C.R. Stanley, C.D. Farmer, N. Lopez, P. Diaz, E. Canovas, P.G. Linares, and A. Luque, Production of Photocurrent due to Intermediate-to-Conduction-Band Transitions: A Demonstration of a Key Operating Principle of the Intermediate-Band Solar Cell. *Physical Review Letters*, 2006. **97**(24): pp. 247701.

[48] Ohring, M., The materials science of thin films: deposition and structure. 2nd ed. 2002, San Diego, USA: Academic Press.

[49] Priester, C. and M. Lannoo, Origin of Self-Assembled Quantum Dots in Highly Mismatched Heteroepitaxy. *Physical Review Letters*, 1995. **75**(1): pp. 93-96.

[50] Dobbs, H.T., D.D. Vvedensky, A. Zangwill, J. Johansson, N. Carlsson, and W. Seifert, Mean-field theory of quantum dot formation. *Physical Review Letters*, 1997. **79**(5): pp. 897-900.

[51] Heyn, C. and C. Dumat, Formation and size evolution of self-assembled quantum dots. *Journal of Crystal Growth*, 2001. **227**: pp. 990-994.

[52] da Silva, M.J., A.A. Quivy, P.P. Gonzalez-Borrero, N.T. Moshegov, and E. Marega, Correlation between structural and optical properties of InAs quantum dots along their evolution. *Journal of Crystal Growth*, 2001. **227**: pp. 1025-1028.

[53] Zanella, P., G. Rossetto, N. Brianese, F. Ossola, M. Porchia, and J.O. Williams, Organometallic Precursors in the Growth of Epitaxial Thin-Films of Groups Iii-V Semiconductors by Metal Organic-Chemical Vapor-Deposition. *Chemistry of Materials*, 1991. **3**(2): pp. 225-242.

[54] Dupuis, R.D., Epitaxial growth of III-V nitride semiconductors by metalorganic chemical vapor deposition. *Journal of Crystal Growth*, 1997. **178**(1-2): pp. 56-73.

[55] Aryanto, D., Z. Othaman, A. Ismail, and A.S. Ameruddin, Surface Morphology of In0.5Ga0.5 Quantum Dots Grown using Stranski-Krastanov Growth Mode. *Sains Malaysiana*, 2010. **39**(6): pp. 1025-1030.

[56] Leonard, D., K. Pond, and P. Petroff, Critical layer thickness for self-assembled InAs islands on GaAs. *Physical Review B*, 1994. **50**(16): pp. 11687-11692.

[57] Bhatti, A., M. Grassi Alessi, M. Capizzi, P. Frigeri, and S. Franchi, Optical spectroscopy of quasimonolayer InAs at the onset of quantum-dot nucleation. *Physical Review B*, 1999. **60**(4): pp. 2592-2598.

[58] Leon, R. and S. Fafard, Structural and radiative evolution in quantum dots near the $In_xGa_{1-x}As$/GaAs Stranski-Krastanow transformation. *Physical Review B*, 1998. **58**(4): pp. R1726-R1729.

[59] Shchukin, V. and D. Bimberg, Spontaneous ordering of nanostructures on crystal surfaces. *Reviews of Modern Physics*, 1999. **71**(4): pp. 1125-1171.

[60] Heinrichsdorff, F., A. Krost, M. Grundmann, D. Bimberg, F. Bertram, J. Christen, A. Kosogov, and P. Werner, Self organization phenomena of InGaAs/GaAs quantum dots grown by metalorganic chemical vapour deposition. *Journal of Crystal Growth*, 1997. **170**(1-4): pp. 568-573.

[61] Luque, A. and A. Marti, A metallic intermediate band high efficiency solar cell. *Progress in Photovoltaics*, 2001. **9**(2): pp. 73-86.

[62] Wolf, M., Limitations and Possibilities for Improvement of Photovoltaic Solar Energy Converters: Part I: Considerations for Earth's Surface Operation. *Proceedings of the IRE*, 1960. **48**(7): pp. 1246-1263.

[63] Ley, M., J. Boudaden, and Z.T. Kuznicki, Thermodynamic efficiency of an intermediate band photovoltaic cell with low threshold Auger generation. *Journal of Applied Physics*, 2005. **98**(4): pp. 044905.

[64] Boer, K.W., Survey of Semiconductor Physics. 1990, New York: Van Nostrand Reinhold. pp. 201, 249, 617.

[65] Wahnón, P. and C. Tablero, Ab initio electronic structure calculations for metallic intermediate band formation in photovoltaic materials. *Physical Review B*, 2002. **65**(16): pp. 165115.

[66] Yu, K., W. Walukiewicz, J. Wu, W. Shan, J. Beeman, M. Scarpulla, O. Dubon, and P. Becla, Diluted II-VI Oxide Semiconductors with Multiple Band Gaps. *Physical Review Letters*, 2003. **91**(24): pp. 246403.

[67] Tablero, C., Electronic and magnetic properties of ZnS doped with Cr. *Physical Review B*, 2006. **74**(19): pp. 195203.

[68] Palacios, P., J. Fernández, K. Sánchez, J. Conesa, and P. Wahnón, First-principles investigation of isolated band formation in half-metallic TixGa1-xP. *Physical Review B*, 2006. **73**(8): pp. 085206.

[69] Marti, A., L. Cuadra, and A. Luque. Quantum dot intermediate band solar cell. in *28th IEEE Photovoltaic Specialists Conference*. 2000. Anchorage, Ak: Ieee.

[70] Laghumavarapu, R.B., M. El-Emawy, N. Nuntawong, A. Moscho, L.F. Lester, and D.L. Huffaker, Improved device performance of InAs/GaAs quantum dot solar cells with GaP strain compensation layers. *Applied Physics Letters*, 2007. **91**(24): pp. 243115.

[71] Guimard, D., R. Morihara, D. Bordel, K. Tanabe, Y. Wakayama, M. Nishioka, and Y. Arakawa, Fabrication of InAs/GaAs quantum dot solar cells with enhanced photocurrent and without degradation of open circuit voltage. *Applied Physics Letters*, 2010. **96**(20): pp. 203507.

[72] Jolley, G., H.F. Lu, L. Fu, H.H. Tan, and C. Jagadish, Electron-hole recombination properties of In0.5Ga0.5As/GaAs quantum dot solar cells and the influence on the open circuit voltage. *Applied Physics Letters*, 2010. **97**(12): pp. 123505.

[73] Lu, H.F., L. Fu, J. Greg, T. Hark Hoe, T. Sudersena Rao, and J. Chennupati, Temperature dependence of dark current properties of InGaAs/GaAs quantum dot solar cells. *Applied Physics Letters*, 2011. **98**(18): pp. 183509.

[74] Sugaya, T., S. Furue, H. Komaki, T. Amano, M. Mori, K. Komori, S. Niki, O. Numakami, and Y. Okano, Highly stacked and well-aligned $In_{0.4}Ga_{0.6}As$ quantum dot solar cells with $In_{0.2}Ga_{0.8}As$ cap layer. *Applied Physics Letters*, 2010. **97**(18): pp. 183104.

[75] Barnham, K., J. Connolly, P. Griffin, G. Haarpaintner, J. Nelson, E. Tsui, A. Zachariou, J. Osborne, C. Button, G. Hill, M. Hopkinson, M. Pate, J. Roberts, and T. Foxon, Voltage enhancement in quantum well solar cells. *Journal of Applied Physics*, 1996. **80**(2): pp. 1201-1206

Chapter 2

Experimental techniques

2.1 Introduction

This chapter will discuss the self-assembled growth of InGaAs/GaAs quantum dot solar cell (QDSC) on GaAs substrate by Metal Organic Chemical Vapour Deposition. The formation of QDs follows the Stranski-Krastanov (S-K) growth mode, which will be discussed in section 2.2. Stranski-Krastanov growth is a type of growth that has an epitaxy layer of 3-7 % lattice mismatch on the substrate with a smaller lattice constant [1-3]. The lattice mismatch between them can lead to the growth of a strained film, and the film initially grows in a layer-by-layer fashion until a certain critical thickness, beyond which 3D QDs will be formed. In this work, $In_xGa_{1-x}As$ layer that has larger lattice constant are deposited on GaAs (001) substrate, by adjusting the materials composition and growth parameters, $In_xGa_{1-x}As$/GaAs wetting layer (WL) and QDs structure will be obtained.

Section 2.3 discusses fabrication techniques used in this thesis, such as photo-lithography, wet and dry etching, metal evaporation, sputtering and thermal annealing. Detailed processing steps are shown in Section 2.4. Section 2.5 describes materials characterization techniques, including atomic force microscopy, electron microscopy et al. More techniques used for solar cell device characterization will be shown in Section 2.6, including photoluminescence, electroluminescence, current-voltage, quantum efficiency and spectral response measurements.

During the solar cell growth, device fabrication and characterization processes, most of the experiments have been mainly completed by the candidate after the proper training. Some of characterizations were achieved under the help of postdoctoral staff or technicians in ANU, such as atomic force microscope, scanning electron microscope and transmission electron microscope.

In summary, this chapter briefly describes the working principles of various equipment have been used in this thesis.

2.2 Metal Organic Chemical Vapour Deposition Growth

Metal Organic Chemical Vapour Deposition (MOCVD), also known as Metal Organic Vapour Phase Epitaxy (MOVPE), is an epitaxial growth technique

for crystalline materials, especially compound semiconductors, from the surface reaction of metal-organics and hydrides containing the required chemical elements [4, 5]. MOCVD is a technique that is widely used to deposit very thin layers of atoms onto a semiconductor wafer. It is the most significant manufacturing process for III-V compound semiconductors, especially for those based on Gallium Arsenide (GaAs) Indium Phosphide (InP) and Gallium Nitride (GaN). Another commonly used technique for epitaxial growth is Molecular Beam Epitaxy (MBE). MBE offers the advantage of more controllable growth than MOCVD, due to the well developed in-situ monitoring system [6]. But the MBE growth rate is too slow to be applied for large-scale industrial production, while MOCVD has faster growth rate so is an industry preferred technique.

Many types of low dimensional structures including quantum wells, quantum dots and nanowires can be grown by MOCVD [4, 7]. In the MOCVD the semiconductor precursors are injected into the reactor by highly purified carrier gas H_2 at their corresponding gaseous states [8]. Metalorganic precursors such as trimethylgallium ($Ga(CH_3)_3$), trimethylindium ($In(CH_3)_3$), and trimethylaluminium ($Al(CH_3)_3$) are used as the precursors for the group III elements, gallium (Ga), indium (In) and aluminium (Al), respectively. Hydride precursors arsine (AsH_3) and phosphine (PH_3) are used as precursors for group V elements, arsenic (As), phosphorus (P), respectively. AsH_3 and PH_3 are stored in high pressure cylinders, whereas TMGa, TMAl, and TMIn are stored in sealed stainless-steel cylinders held at a constant temperature in temperature-controlled baths. These incoming sources undergo pyrolysis chemical reactions and then deposit on the GaAs substrate atom by atom. The pipeline of the system is shown in Figure 2.1.

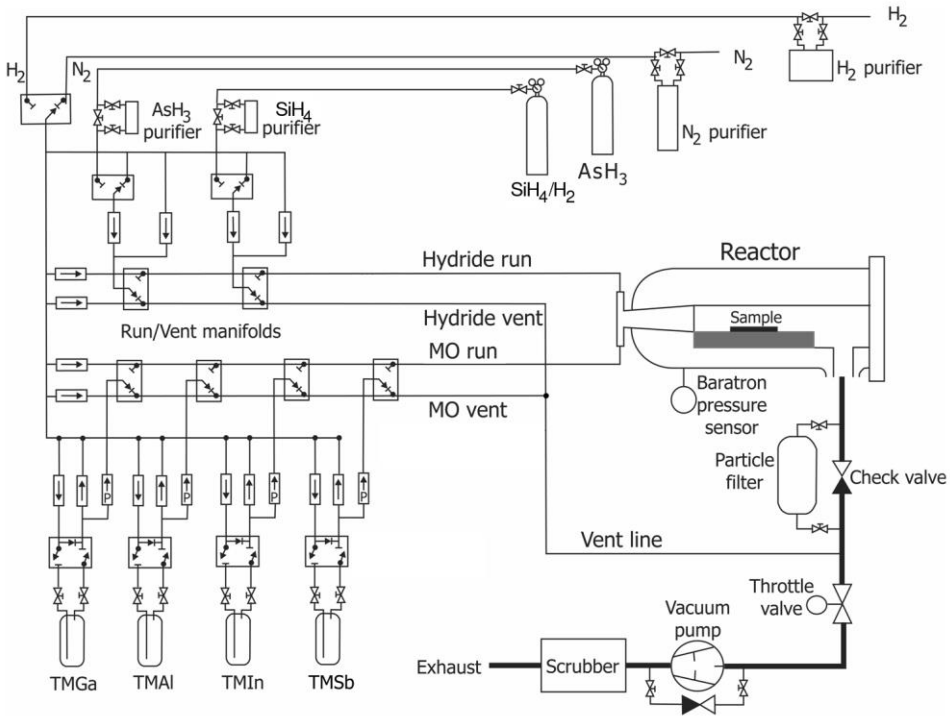

Figure 2.1: Schematic of the Aixtron AIX 200/4 metal-organic chemical vapour deposition system.

In this thesis, all the GaAs based solar cell structures were grown using the Aixtron AIX 200/4 horizontal flow MOCVD reactor at the Australian National University. The reactor was working at low pressure typically 100 mbar.

III-V semiconductors with binary, ternary and quaternary compositions can be grown by MOCVD. The typical equations for describing the pyrolysis chemical reactions to form GaAs and $In_xGa_{1-x}As$ used in this work are listed below:

$$(CH_3)_3Ga + AsH_3 = GaAs + 3CH_4 \quad (2.1)$$

And

$$x(CH_3)_3In + (1-x)(CH_3)_3Ga + AsH_3 = In_xGa_{1-x}As + 3CH_4 \quad (2.2)$$

As discussed in Chapter 1, the epitaxial deposition on a substrate is achieved by three different modes, and the self-organized QDs are grown through the S-K mode [9, 10].

During the MOCVD growth of $In_xGa_{1-x}As$/GaAs quantum dots investigated in this thesis, through the pyrolysis reactions (see equation 2.2) $In_xGa_{1-x}As$ will be firstly formed on the GaAs (001) substrate at the beginning

of the growth. After a few monolayers growth, the quantum dots appear due to lattice mismatch induced strain accumulation. The first few layers underneath the dots is called wetting layer as shown in Figure 2.2 (c), and usually QD is a few nanometres in height and tens of nanometres in width. The typical growth rate used for our GaAs based solar cell is 0.63 nm/s at 550 ℃. Various growth rate and temperatures have been used for different material growth (such as InGaAs QDs and AlGaAs layer) in the experiments to achieve the best quality material.

2.3 Device fabrication techniques

2.3.1 Photolithography

Photolithography, also termed as optical lithography or UV lithography, is a common process used in microfabrication to pattern parts of a thin film or a substrate. It uses UV light to transfer a pre-defined geometric defined pattern to a light-sensitive organic photoresist on the substrate. Generally, photoresist can be classified as either a positive or a negative resist, depending on the changes that occur under UV exposure. For the positive resist, exposure results in destruction of polymer bonds, increasing the resist solubility so these areas will be dissolved when placed in a developer. Hence resist is left only where the mask was opaque and the pattern is transferred onto the substrate [11, 12]. Negative resists behave in the opposite way, those unexposed areas will be developed away.

In this work Karl Suss MA6 Mask Aligner was used to fabricate solar cell devices. To fabricate the solar cell devices investigated in this thesis, samples were thoroughly cleaned by acetone, isopropanol and dried in oven at 85 ℃ for 3 minutes. Then the AZ 5214 E positive photoresist was spun on it at 4000 rpm for 30 s. After a 15 minutes soft-bake at 85 ℃, the samples were individually placed into the MA6 mask aligner. They were aligned and then exposed to UV light from a mercury lamp for 15 s. UV exposed sample is immersed in the developer for 30-50 s (constant visual inspection is required), then rinsed with deionised (DI) water. The resist was developed in AZ 726 MIF photoresist developer, which is the solution of tetramethylammonium hydroxide in water. After thoroughly rinsing in DI water and examination under an optical microscope, the samples were hard-baked for two minutes at 110 ℃. The photoresist pattern will be used as either etching mask that allows separation of top and bottom contact or define of contact pattern through subsequent metal deposition and lift-off.

2.3.2 Wet chemical etching

Wet chemical etching is widely used for fabrication of semiconductor devices. When used in conjunction with a photolithographic process, it enables patterns to be transferred from a designed mask to the semiconductor wafer. Wet etching is a low-cost and convenient technique due to its simplicity and scalability, where the substrate is just immersed in a solution for certain time, such as an acid, a base and/or an oxidizing agent. Etching rate depends on many parameters, including solution composition and concentration, semiconductor wafer orientation and material composition, etching temperature etc. With certain concentration of a etching solution, etching temperature can also greatly affect the etching rate with a higher etching rate achieved at higher temperature. Normally, when more precise etch depths are needed the solution can be cooled down or diluted to lower the reaction speed, vice versa, heating and higher concentration can be used to increase the etching rate. Most of the etching works were performed at room temperature in this thesis. A variety of etching solutions were used for different fabrication processes in this thesis, and the main etchants are listed in Table 2.1:

Table 2.1: Etchants solution used for wet etching of different materials

Materials	**Etchant rate (by volume)**	**Temperature (℃)**	**Comments**
(Al)(In)GaAs	Citric acid: 30% H_2O_2: H_2O= 3: 43: 150	Room temperature	Selective etching
GaAs	85% H_3PO_4: 30% H_2O_2: H_2O= 1: 1: 3	18	Most GaAs based III-V materials
GaO_x+ AsO_y	36% HCl: H_2O= 1: 9	Room temperature	GaAs native oxide etching
SiO_x+ SiN_y	48% HF: H_2O= 1: 9	4	Si based dielectric films

The chemical mechanism of wet etching of GaAs-based materials is the oxidation of the surface to form Ga and As oxides, and followed by the dissolving of these oxides by chemical reaction with acids or bases. Hydrogen peroxide is normally served as an oxidising agent to promote the formation of the surface oxides in most cases. A simplified representation of the chemistry typically involved in GaAs etching is given by the following equations [13]. To initiate the etching process, an oxide is formed on the surface of the GaAs by reaction with an oxidising agent, typically H_2O_2:

$$\mathrm{GaAs} + (\mathrm{oxidiser}) \rightarrow \mathrm{GaO_x/AsO_y} \tag{2.3}$$

The surface oxides are then attacked by either an acid or a base and will be dissolved to release Ga^{3+} and AsO_4^{2-} ions in solution:

$$GaO_x/AsO_y + (\text{acid or base}) \rightarrow Ga^{3+} + AsO_4^{2-} \quad (2.4)$$

The wet etching rate for GaAs is about 1.61 μm per minute. Selective etching was used to remove the surface heavily doped GaAs capping layer while preserve the AlGaAs window layer. The etching rate for GaAs is ~6 nm per second, and ~0.4 nm per second for $Al_{0.45}Ga_{0.55}As$, the rate difference is high enough to etch two layers selectively. More operation details are shown in the section 2.4.

2.3.3 Thermal and Electron-beam evaporators

For relatively large amount and quick metal deposition, thermal and electron-beam (E-beam) evaporators are the two most common equipment used for the device fabrication.

An Edward Austo 306 thermal evaporator enables deposition of a wide range of metals for various research projects. In this deposition technique, thermal energy is applied to the source material, which then evaporates after melting. These are line-of-sight depositions that take place in ultra-high vacuum conditions, where the material to be evaporated is placed inside a tungsten boat and the material is then heated resistively. Although the process is simple, the deposited materials using this method are easy to be contaminated, and cannot be used to deposit materials with high melting points [15]. This method was used to fabricate solar cell devices for growth optimization.

Alternatively, another method of depositing films on the surface of samples is by E-beam evaporation. The materials to be deposited are heated by a focused beam of electrons to a high temperature until it evaporates. The material then recondenses on all the surfaces of the evaporation chamber, including on exposed samples. In this thesis a Temescal BJD-2000 E-beam Evaporator system was used for the deposition of metal contacts (Ti, Pt, Ge, and Au) during solar cells processing to achieve Ohmic contact [15]. The system also includes an extended chamber for a larger distance between sources and samples to avoid excessive heating during thick metallization for consequent lift-off process.

2.3.4 Magnetron sputter coating technique

Magnetron sputter coating technique is a physical vapour deposition (PVD) process. During sputter deposition, the source material is a solid target and it is sputtered away by an ionised working gas (in the form of glow-discharge

plasmas), such as Ar. A DC or radio frequency (RF) power is applied between the substrate and a metal target, which acts as the cathode, to create the discharge. As the target is bombarded with ions, the surface is eroded away and material is deposited onto the anode (substrate).

In this thesis, the AJA sputtering system was used to deposit TiO_2 film on the QD solar cells as the base to form Ag nanoparticles, which will be discussed in Chapter 6. The AJA system is equipped with 6 magnetron guns (3 x DC, 3 x RF) with up to 800 ℃ substrate heating and the capability for deposition of a wide range of metal and oxide materials. The sputter has a load-lock that allowing a maximum wafer size of 100mm. A large range of metals and dielectrics are available [16].

2.3.5 Thermal annealing

2.3.5.1 Rapid thermal annealing

Rapid thermal annealing (RTA) processes are commonly used to alloy metals to form Ohmic contacts on III-V semiconductors. Also, RTA at high temperatures is carried out to produce interdiffusion effects in the devices. In this thesis, metal contact alloying and post-growth thermal annealing for QD solar cells and GaAs reference cells were accomplished by rapid thermal annealing [17]. Annealings were carried out in an AET thermal RX rapid thermal annealer or a Qualiflow JetFirst 100 annealing equipment. Cross-contamination is minimised through the use of material-specific RTA liners or graphite holders for these two machines respectively. All the anneals were carried out under high-purity Ar ambient and with fresh GaAs wafer as proximity capping to prevent As desorption which occurs at above 400 ℃. The temperature was ramped up at 100 ℃/s and after annealing the temperature was allowed to fall naturally under the Ar ambient. For contact metallization, devices were heated up to 400 ℃ for 1 minute. For post-growth thermal inter-diffusion study the QD samples were annealed at temperatures from 700 to 850 ℃ with the step of 50 ℃ for 50 s respectively. The exhaust gases and particulates are safely extracted from the laboratory.

2.3.5.2 Furnace annealing

In Chapter 6, conventional furnace annealing was used for Ag nanoparticles formation. The low temperature annealing was performed in a quartz tube at 200 ℃ for 50 minutes under the high-purity Ar ambient.

2.4 Solar cell fabrication process

The techniques described in section 2.3 were employed to fabricate the quantum dot solar cells that are investigated in this thesis. Figure 2.2 shows the flowchart for the device fabrication process. After MOCVD growth, room temperature photoluminescence (PL) was used first to evaluate the optical properties of QDs grown on the GaAs wafer. Then the samples were cleaved into several pieces and fabricated into devices with various square mesa sizes (3x3 mm^2, 2x2 mm^2, 1x1 mm^2, or 0.85x 0.85 mm^2), following the steps described below:

- **First photolithography for defining mesa squares**

Firstly, the square mesas were defined through a photolithography process as described in section 2.1.5 by the Karl Suss MA 6 Mask aligner, and photoresist was selectively removed by the developer AZ 726 MIF at room temperature. A 2 minutes hard baking at 110 ℃ was carried out to sharpen the photoresist mesa edge.

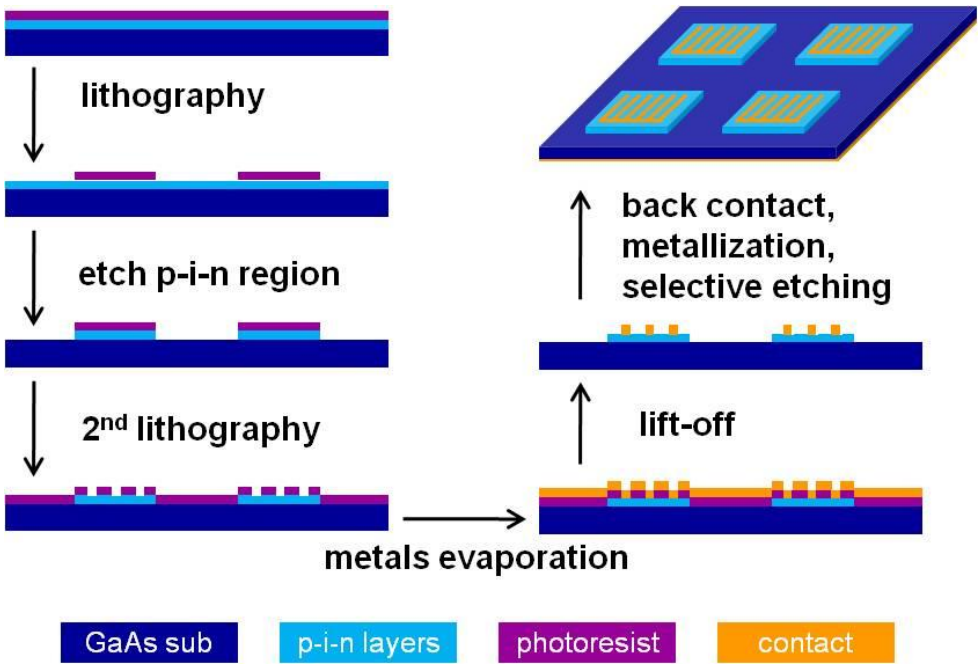

Figure 2.2: The standard processing steps used to fabricate GaAs based quantum dot solar cell devices. The particular post-growth treatments used to modify some devices are described in the relevant chapters.

- **Mesa etching**

Wet chemical etching was carried out in the mixed acid solution of $H_3PO_4/H_2O_2/H_2O$, as described in section 2.3.2. The solution was stirred in a beaker that was immersed in the 18 ℃ water bath for at least 20 minutes. The actual etching rate was tested by etching a clean GaAs wafer which was partially covered by crystal bond, the crystal bond was removed by acetone after 1 minute etching. The etching depth was measured using the AlphaStep mechanical profiler and etching speed was calibrated as 1.61 μm per minute. According to the etching rate, a certain time was calculated to remove the active layers to reach the n^+ (or p^+) bottom substrate. The photoresist was then removed by acetone followed by rinsing in isopropanol and DI water.

- **Second photolithography process for defining of metal contact patterns**

In the second photolithography step, the layout of the metal contact pattern was also defined by the MA 6 Mask aligner on the AZ 5214 E photoresist. The contact pattern was carefully aligned with respect to the mesa structure on each wafer. After photolithography the native oxide layer was removed by a dilute HCl solution for 40 s in order to make a good Ohmic contact.

- **Metallization**

After etching, the samples were immediately loaded into the electron-beam or thermal evaporator chamber. The alloys for n+ and p+ doped GaAs are Ge-(Ni)-Au and Ti-(Pt)-Au respectively in order to form Ohmic contacts (see section of 2.1.5). After metal deposition, all samples were immersed into acetone for lift-off. For work in chapters 3, 5 and 6, when the back surface contact was required due to the mask design, the rear of the wafers were mechanically polished. Then the ~180 nm Ge-(Ni)-Au alloy (for n type GaAs) was deposited on the rear surface.

In order to form effective Ohmic contacts, rapid thermal annealing was carried out at 400 ℃ for 60 seconds. The Ar gas was used as protection ambient during the whole annealing process. After metallization, the top 100 nm p^+ GaAs contact layer was selectively removed to avoid the severe light absorption beyond active region of solar cell. The etchant was the mixture of citric acid, H_2O_2 and DI water which can selectively remove GaAs but preserve p-type $Al_xGa_{1-x}As$ layer. When selective etching was finished, dried samples were cleaved into several small pieces by the Loomis Industries LSD-110 scriber. These small devices were mounted on the 14-pin dual inline

packages by the two-part conductive silver epoxy and wire-bonded using the Marpet Enterprises Inc. 1204 W ultrasonic wedge bonder.

2.5 Materials characterization techniques

2.5.1 Atomic force microscopy

The atomic force microscope (AFM) is a type of scanning probe microscope (SPM), which is designed to characterise localized material properties, such as height, friction, magnetism, with a probe. To acquire high image resolution, AFMs can generally measure the vertical and lateral deflections of the cantilever by using the optical lever. The optical lever operates by reflecting a laser beam off the cantilever.

AFM is an essential technique for quantum dot growth optimization. It is a non-destructive technique that can be used to look at the surface of a sample at the nanometre scale. The equipment used in this work was a Digital Instruments Nanoscope III Multimode AFM. The sample is placed on a piezo-electric stage and then a small sharp tip is placed above the sample. The tip sits on the end of a V-shaped cantilever that has a small spring constant. A laser beam is focused onto the tip of the cantilever and the position of the reflected laser beam is measured by a position-sensitive four-segment photo-detector. The back of the cantilever is coated in gold such that the laser light is reflected efficiently. The AFM system schematic is shown in Figure 2.3.

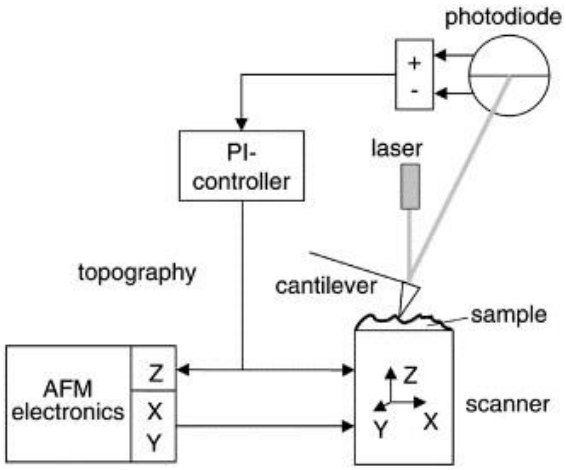

Figure 2.3: Schematic of the NanoScope III multimode scanning probe microscope that was used for AFM measurements. Quoted from Ref. [18].

Among the multiple working modes of AFM, tapping mode (noncontact mode) was the method used for QDSC measurement in this work. It operates

under AC mode, through the use of an oscillating cantilever. A stiff cantilever is oscillated in the attractive regime, meaning that the tip is quite close to the sample, but not touching it (hence, noncontact). The forces between the tip and sample are quite low. The detection scheme is based on measuring changes to the resonant frequency or amplitude of the cantilever. Using this technique, uncapped quantum dots can be measured to estimate their size, height, and also density.

2.5.2 Scanning electron microscopy

A scanning electron microscope (SEM) is a tool for observing invisible scales of microspace and nanospace. By using a focussed beam of electrons, the SEM reveals levels of detail and complexity inaccessible by conventional optical microscopy. Accelerated electrons in an SEM carry significant amounts of kinetic energy, and this energy is dissipated as a variety of signals produced by electron-sample interactions when the incident electrons are decelerated in the solid sample. These signals include secondary electrons, backscattered electrons, diffracted backscattered electrons, photons, visible light, and heat. Secondary electrons and backscattered electrons are commonly used for imaging samples: secondary electrons are most valuable for showing morphology and topography on samples and backscattered electrons are most valuable for illustrating contrasts in composition in multiphase samples. SEM images are produced by collecting the secondary electrons. SEM analysis is considered to be non-destructive, because the electrons and X-rays generated by electron-sample interactions do not lead to volume loss of the sample, so it is possible to analyse the same materials repeatedly.

The scanning transmission electron microscope (STEM) is also a useful tool for the characterization of nanostructures [19, 20]. The SEM and STEM images presented in the thesis were performed on a FEI Helios 600 NanoLab Focused Ion Beam system. 30kV e-beam was applied in this machine which allows very high resolution SEM imaging (<1nm @ 15kV and <2.5nm at 1kV electron beam) alongside other ion-beam features like simple milling and TEM lamellae preparation [21].

2.5.3 Transmission electron microscopy

The transmission electron microscope (TEM) forms an image by accelerating a beam of electrons that pass through the specimen and collecting signals. In

TEM, electrons are accelerated to 100 KeV or higher (up to 1MeV), projected onto a thin specimen (less than 200 nm) by means of the condenser lens system, and penetrate the sample thickness either undeflected or deflected. The greatest advantages that TEM offers are the high magnification ranging from 50 to 1,000,000 times and its ability to provide both image and diffraction information from a single sample. Magnifications of up to 1,000,000 times and resolution below 1 nm are achieved routinely. The scattering processes experienced by electrons during their passage through the specimen determine the kind of information obtained. Elastic scattering involves no energy loss and gives rise to diffraction patterns. Inelastic interactions between primary electrons and sample electrons at heterogeneities such as grain boundaries, dislocations, second phase particles, defects, density variations, etc., cause complex absorption and scattering effects, leading to a spatial variation in the intensity of the transmitted electrons. In TEM one can switch between imaging the sample and viewing its diffraction pattern by changing the strength of the intermediate lens. Figure 2.4 show the different signals produced by electron/sample reactions [22].

The transmission electron microscope is used to examine the crystal structure, composition, and properties of specimens in submicron details. The investigation of the morphology, structure, and local chemistry of metals, ceramics, and minerals is an important aspect of contemporary materials science.

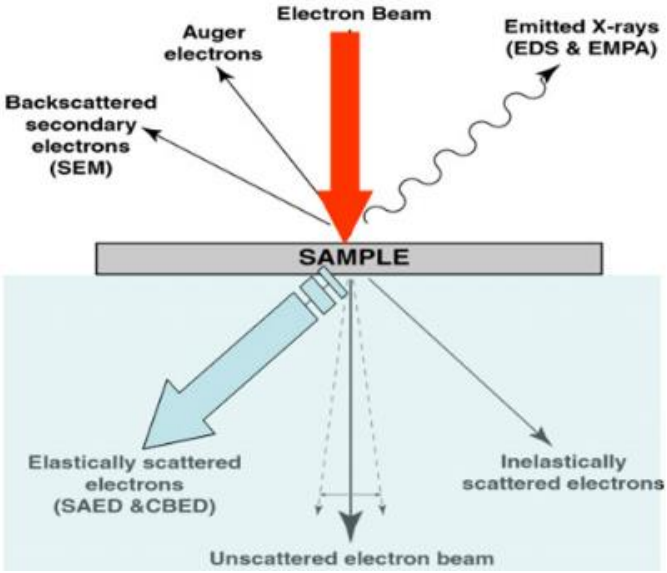

Figure 2.4: The variety of signals produced during electrons/sample interactions. Quoted from Ref. [22].

All TEM images and diffraction patterns of QDSCs presented in this thesis were captured with the help of Dr. Jenny Wong-Leung using the Philips CM300 system at the Research School of Earth Sciences, at the energy of 300 keV.

2.5.4 Mechanical surface profiler

During the solar cells fabrication and characterization processes, it is critical to measure depth or dimensions of some fine structures. A simple characterization technique used for this purpose is mechanical stylus profiler.

Basically, a stylus is scanned along the sample surface to measure the variation of sample height along the scan line. The system used for this research work is a Dektak Surface Profiler. This mechanical surface profiler allows very accurate 1D step height measurements, the analysis capability also allows for measuring wafer bow (to calculate mechanical stress) and 1D roughness. It was mainly used for the former, in order to measure etch depths or film thicknesses. It was frequently used to measure the thickness of wet etching depth after photolithography exposure and hence determine the actual etching rate for the certain materials. A video camera with variable magnification allows for manual placement of the stylus and the system is controlled from the software on PC for scan length and speed. Available stylus sizes are 12.5 μm and 2 μm and vertical resolution is as small as 1.1 nm [16].

2.6 Device characterization techniques

2.6.1 Photoluminescence

Photoluminescence is a simple, powerful and non-destructive technique that is widely used to determine the properties and quality of semiconductors. The simple principle refers to the absorption and emission of photons. The intensity and spectral content of the photoluminescence is a direct measure of various important properties, such as band gap, impurity levels and defects, and recombination mechanisms etc.

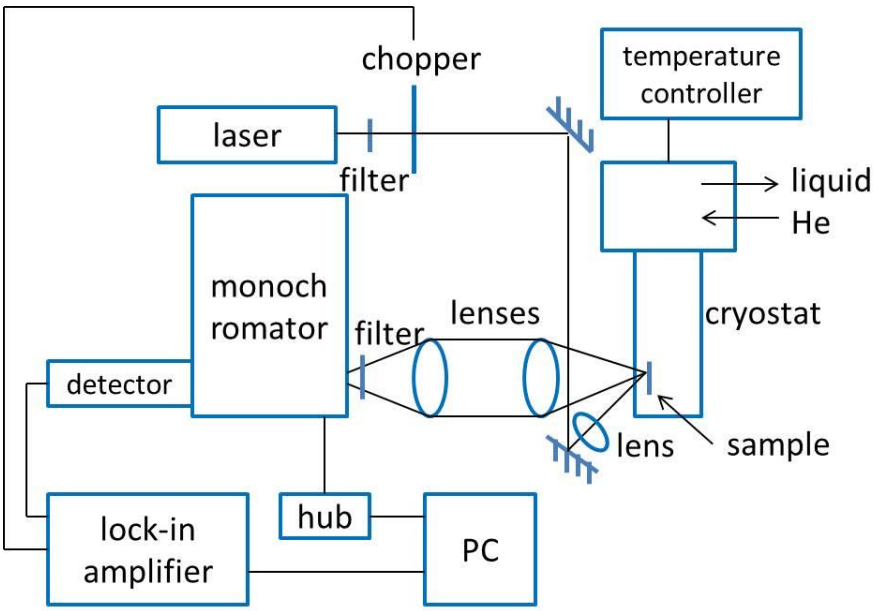

Figure 2.5: Photoluminescence system set-up used in the thesis.

We use the PL systems at EME to analyse the optical properties of different quantum dots solar cell structures throughout this thesis [15]. Upon the excitation from the Diode-Pumped frequency doubled Solid-State (DPSS) laser at a wavelength of 532 nm, electron-hole pairs will be generated in the solar cell materials and then recombine due to radiative recombination. The emitted photon from the device was collected through a Princeton Instruments SpectraPro 2300 i Monochromator and a thermal-electrically cooled InGaAs photodetector. With frequency synchronised by the chopper, the signal from the device was collected through lock-in technique. A schematic diagram of the typical PL set-up used for this thesis is shown in Figure 2.5, which allows temperature dependent PL measurements (from ~ 11 K to room temperature) over a broad spectral range (200 nm-15 μm) for various materials and structures.

2.6.2 Electroluminescence

Similar to the PL discussed in last section, which is a photon-induced emission process, semiconductor device may also produce spontaneous emission when a current is injected from external circuit, this phenomenon is called electroluminescence (EL).

In EL measurements the carriers inside the sample are injected electrically rather than excited optically, the spontaneous emission is collected and analysed. For the research in this thesis, electroluminescence measurements were carried out on QD solar cell devices that were mounted in the closed

cycled He cryostat, in which the temperature could be controlled from 10 K to 300 K. The experimental set-up is shown in Figure 2.6, the optical setup is similar to that for photoluminescence measurements except that the samples are electrically connected to a current source and the electron-holes pairs are generated by current injection (hence the name electroluminescence) instead of a laser source. The devices were put under certain forward biases and excited by injecting current with various current densities (from 10 mA/cm^2 to up to 1000 mA/cm^2). The spontaneous emission from one surface facet of the device was focussed onto the slit of monochromator and detected by an InGaAs photodetector. The Princeton Instruments SpectraPro 2300 i monochromator and a cooled InGaAs diode detector were used.

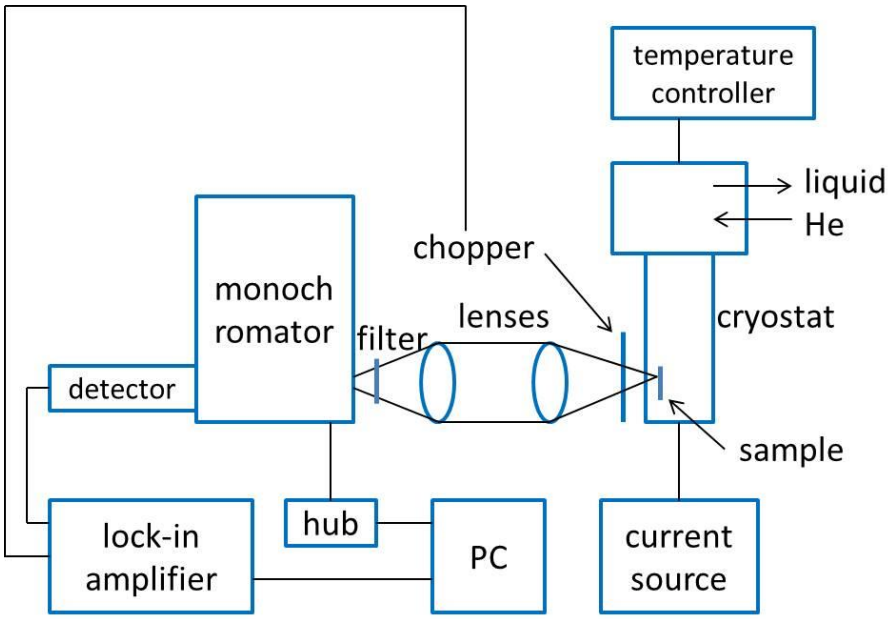

Figure 2.6: Electroluminescence system typical set-up used in the thesis.

By analysing the spontaneous emission spectra with increasing injection current intensity, for example, their peak position shift and line-width, further insight into the quantum dot solar cell devices can be obtained. The temperature dependent emission properties were also investigated to reveal the recombination phenomena within QDSCs.

2.6.3 Current-voltage (I-V) characteristics

2.6.3.1 Light I-V

For the standard I-V tests in this thesis, a Newport (Oriel) 91160 Solar Simulator (150 W) was used to measure the I-V characteristics of various

QDSCs under the 1 sun @ AM 1.5G illumination to obtain basic device parameters including short circuit current density (J_{sc}), open circuit voltage (V_{oc}), fill factor (FF), parasitic resistances and solar cell efficiency (η) [23]. Keithley 2401 Low Voltage Source meter is the 4-wire remote Instrument that was used to monitor and collect the I-V characteristics.

In addition, to investigate the temperature dependent I-V behaviour, the solar cell devices were also placed into the closed cycled He cryostat. The white light source from a tungsten lamp was focused on the device by using of optical lenses to obtain various light intensities illumination. The current-voltage data were collected by a Hewlett Packard 4140 B Pico-ampere Meter.

2.6.3.2 Dark I-V

In order to reveal fundamental mechanisms of GaAs based quantum dot solar cells, dark current-voltage is an important property to study. Temperature dependent dark currents were measured with a closed cycle He cryostat. The device packages were attached to a cold finger in the cryostat. The entire equipment was then covered by Al foil to create a dark condition, and evacuated under a vacuum of ~ 10^{-6} Torr. The temperature was adjusted with a LakeShore model 331 temperature controller to the value as low as ~11 K. Measurements were generally carried out at 20 K steps up to 310 K. Current was measured by the Hewlett Packard 4140B pico-ampere meter, the noise current was around 10 pA. This pico-ampere meter was also used as the DC voltage source and the LabVIEW programme on PC was used to automate the measurement processes.

2.6.4 External quantum efficiency and spectral response measurements

2.6.4.1 Spectral response

Generally, spectral response can be described as the ratio of the current generated by the solar cell to the power of the incident light illuminated on the cell. In this thesis, the wavelength dependent incident power from the tungsten lamp was calibrated by an InGaAs detector, and as shown by the schematics in Figure 2.9, focused on the device through the SpectraPro 2300 i monochromator. The photocurrent was then amplified through low noise current preamplifier and lock-in amplifier and then collected using the Princeton Instruments control software. During spectral response measurement, different biases were applied externally for some devices, and

the spectral response was measured in a wide temperature range from 30 K to 310 K at 20 K steps. The spectral wavelength was scanned from 750 nm to 1200 nm which covered the bandgap energies of the GaAs bulk material, wetting layer and QDs. Although the relative intensity of various peaks in spectral response curves may be different from those observed in the EQE measurement, they reveal similar physical information when comparisons were made among different samples under the same light illumination. Moreover, spectral response measurements can be performed under different biases and temperatures for detailed analysis of the carrier generation, recombination and collection processes for QD and reference devices. A schematic diagram is shown in Figure 2.7.

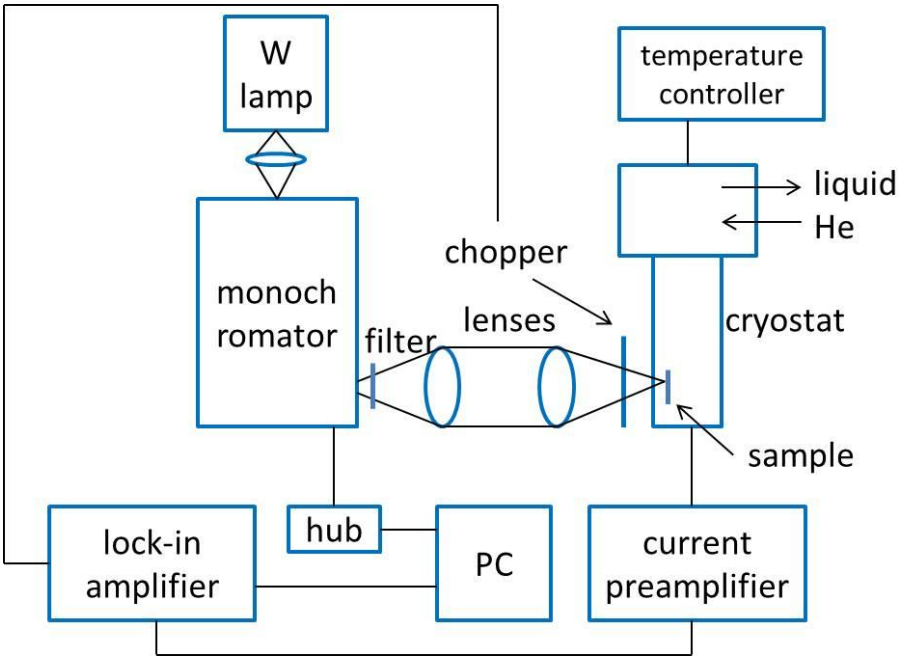

Figure 2.7: Schematic of spectral response measurement set-up.

2.6.4.2 External quantum efficiency

External quantum efficiency (EQE) is the ratio of the number of carriers collected from the solar cell to the number of photons of a given energy incident on the solar cell. Apparently, the quantum efficiency for photons with energy below the materials band gap is zero [24]. EQE of a solar cell includes the effect of optical losses such as transmission and reflection, and internal quantum efficiency (IQE) refers to the efficiency with which photons that are not reflected or transmitted out of the cell.

For practical solar cell studies, optical losses should be taken into account for its performance so EQE is the most commonly used technique to evaluate

solar cell performances. In this work, EQE measurements were performed using the ORIEL IQE-200 system, the signal was collected at the short circuit condition.

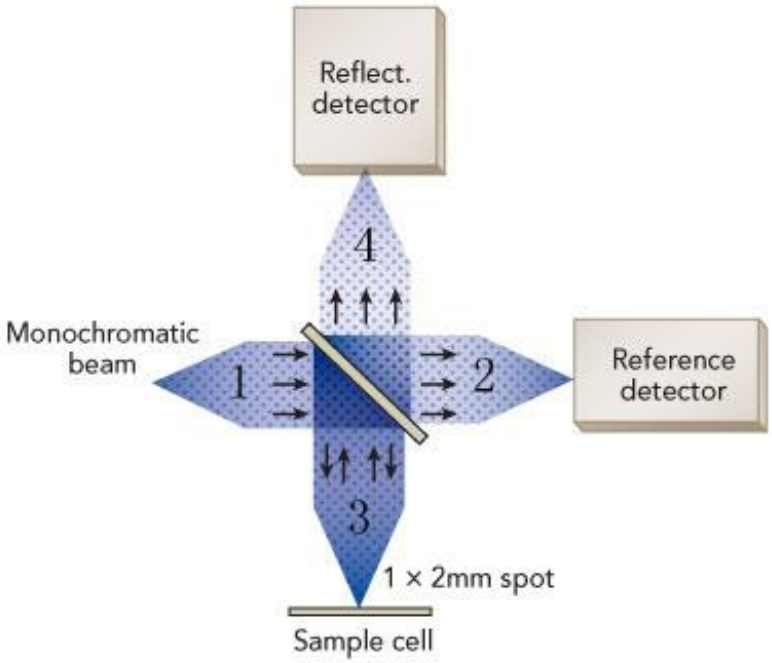

Figure 2.8: Beam delivery schematic of the Oriel IQE-200 system.

The optical layout of the QE-200 (Figure 2.8) comprises one spectrally neutral 50-50 beam splitter and four lenses. The output light from the monochromator is first collimated by lens 1. The collimated light is then split into two beams. One beam passes through the beam splitter and is focused by lens 2 onto the reference Detector. This detector measures the output light power at any given wavelength. The other beam is reflected by the beam splitter down onto the sample surface through focusing lens 3 for QE measurement, the spot size on the sample is also determined by lens 3. For internal quantum efficiency measurement, the reflected light from the sample is collimated by lens 3 and focused behind the beam splitter by lens 4 onto the reflectance detector [25].

2.6.4.3 Inter-subband photocurrent

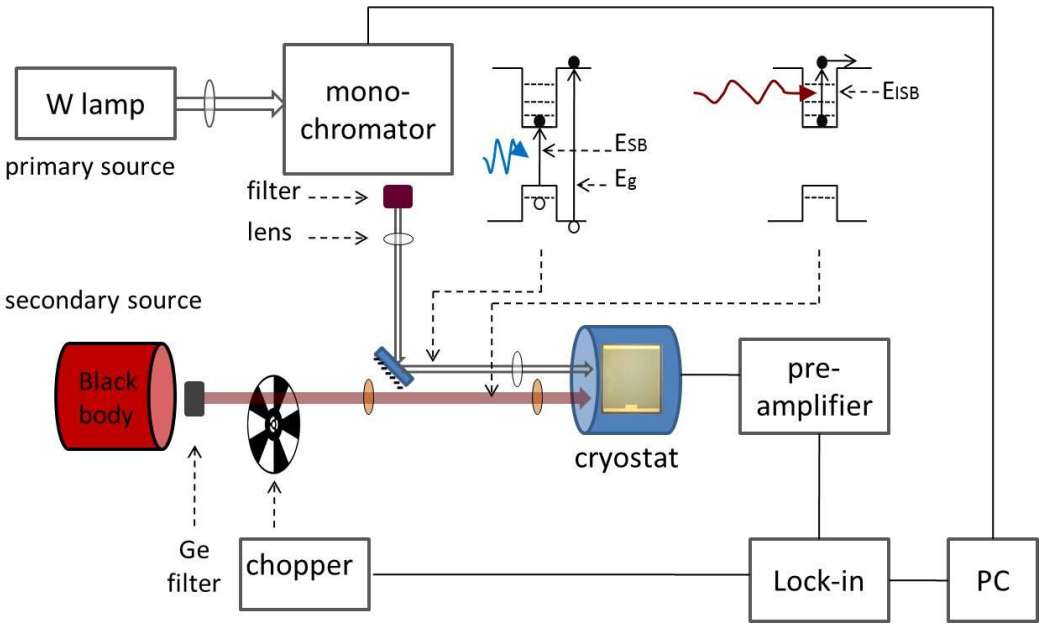

Figure 2.9: The schematic of inter-subband photocurrent measurement set-up.

In addition to the normal spectral response that is correlated to VB to CB transition, it is also expected that there is the 2nd photon excitation process for QDSC [26-28]. The so-called Inter-subband excitation can be achieved by low energy photons. To perform temperature dependent inter-subband photocurrent measurements, the solar cells were mounted in a closed cycle cryostat with a BaF_2 window that allows optical transmission up to wavelength of 11 μm [29]. A calibrated 800 ℃ blackbody radiation source with an internal chopper was used to induce the inter-subband photocurrent. While the solar cell was also illuminated by white light from a tungsten lamp to populate the QD states with photo-generated carriers. The photocurrent was collected under various biases by a current preamplifier connected to a lock-in amplifier. The measurement set-up is displayed in Figure 2.9.

References

[1] Heinrichsdorff, F., A. Krost, M. Grundmann, D. Bimberg, F. Bertram, J. Christen, A. Kosogov, and P. Werner, Self organization phenomena of InGaAs/GaAs quantum dots grown by metalorganic chemical vapour deposition. *Journal of Crystal Growth*, 1997. **170**(1-4): pp. 568-573.

[2] Gupta, J.A., S.P. Watkins, E.D. Crozier, J.C. Woicik, D.A. Harrison, D.T. Jiang, I.J. Pickering, and B.A. Karlin, Layer perfection in ultrathin InAs quantum wells in GaAs(001). *Physical Review B*, 2000. **61**(3): pp. 2073-2084.

[3] Leon, R. and S. Fafard, Structural and radiative evolution in quantum dots near the InxGa1-xAs/GaAs Stranski-Krastanow transformation. *Physical Review B*, 1998. **58**(4): pp. R1726-R1729.

[4] Coleman, J.J., Metalorganic chemical vapor deposition for optoelectronic devices. *Proceedings of the Ieee*, 1997. **85**(11): pp. 1715-1729.

[5] Thompson, A.G., MOCVD technology for semiconductors. *Materials Letters*, 1997. **30**(4): pp. 255-263.

[6] Dapkus, P.D., A Critical Comparison of Mocvd and Mbe for Heterojunction Devices. *Journal of Crystal Growth*, 1984. **68**(1): pp. 345-355.

[7] Joyce, H.J., J. Wong-Leung, Q. Gao, H.H. Tan, and C. Jagadish, Phase Perfection in Zinc Blende and Wurtzite III-V Nanowires Using Basic Growth Parameters. *Nano Letters*, 2010. **10**(3): pp. 908-915.

[8] Operation Manual. Aixtron, 2000; Available from: www.aixtron.com.

[9] Zanella, P., G. Rossetto, N. Brianese, F. Ossola, M. Porchia, and J.O. Williams, Organometallic Precursors in the Growth of Epitaxial Thin-Films of Groups Iii-V Semiconductors by Metal Organic-Chemical Vapor-Deposition. *Chemistry of Materials*, 1991. **3**(2): pp. 225-242.

[10] Dupuis, R.D., Epitaxial growth of III-V nitride semiconductors by metalorganic chemical vapor deposition. *Journal of Crystal Growth*, 1997. **178**(1-2): pp. 56-73.

[11] Ohring, M., "Plasma and ion beam processing of thin films," in The materials science of thin films: deposition and structure. second ed. 2002, San Diego, USA: Academic Press.

[12] Clariant, AZ 5214 E image reversal photoresist product data sheet. 2000, Somerville, USA.

[13] Albert G. Baca, C.I.H.A., Fabrication of GaAs Devices. 2005, London, United Kingdom: The Institution of Engineering and Technology. pp. 118-120.

[14] Plasmalab 80 Plus compact modular plasma system: configuration details, Oxford instruments plasma technology. 1997, Bristol, UK.

[15] EME equipment capabilities, available from: http://physics.anu.edu.au/eme/capabilities/.

[16] ANFF services, available from: http://anff-act.anu.edu.au/HTM/detail/other_services.htm.

[17] Fair, R.B., Rapid Thermal Processing. 1993, San Diego: Academic Press.

[18] Schitter, G., R.W. Stark, and A. Stemmer, Fast contact-mode atomic force microscopy on biological specimen by model-based control. *Ultramicroscopy*, 2004. **100**(3-4): pp. 253-257.

[19] Isaacson, M., D. Kopf, M. Utlaut, N.W. Parker, and A.V. Crewe, Direct observations of atomic diffusion by scanning transmission electron microscopy. *Proceedings of the National Academy of Sciences of the United States of America*, 1977. **74**(5): pp. 1802-1806.

[20] Crewe, A.V., J. Wall, and J. Langmore, Visibility of Single Atoms. *Science*, 1970. **168**(3937): pp. 1338-1340.

[21] ANFF flagship services, available from: http://anff-act.anu.edu.au/HTM/detail/flagship_services.htm.

[22] AMMRF training for advanced research, available from: http://www.ammrf.org.au/myscope/.

[23] Newport Solar Simulator Guide, available from: http://www.newport.com/Solar-Simulator-Guide/1016231/1033/content.aspx.

[24] Nelson, J., The Physics of Solar Cells. 2005, London: Imperial College Press.

[25] Adla, A. Instrumentation for quantum efficiency measurement of solar cells: part 2, 2010, available from: http://www.renewableenergyworld.com/rea/news/article/2010/10/instrumentation-for.

[26] Levy, M.Y. and C. Honsberg, Intraband absorption in solar cells with an intermediate band. *Journal of Applied Physics*, 2008. **104**(11): pp. 113103.

[27] Luque, A. and A. Marti, The Intermediate Band Solar Cell: Progress Toward the Realization of an Attractive Concept. *Advanced Materials*, 2010. **22**(2): pp. 160-174.

[28] Marti, A., E. Antolin, C.R. Stanley, C.D. Farmer, N. Lopez, P. Diaz, E. Canovas, P.G. Linares, and A. Luque, Production of Photocurrent due to Intermediate-to-Conduction-Band Transitions: A Demonstration of a Key Operating Principle of the Intermediate-Band Solar Cell. *Physical Review Letters*, 2006. **97**(24): pp. 247701.

[29] Jolley, G., L. Fu, H.F. Lu, H.H. Tan, and C. Jagadish, The role of intersubband optical transitions on the electrical properties of InGaAs/GaAs quantum dot solar cells. *Progress in Photovoltaics: Research and Applications*, 2013. **21**(4): pp. 736-746.

Chapter 3

Growth and properties of InGaAs/GaAs quantum dot solar cells

3.1 Introduction

To obtain efficient and reliable quantum dot solar cell devices, several structural properties of the quantum dot need to be considered [1-3]. Firstly, they need to provide enough light absorption to produce sufficient photocurrent. The three-dimensional nature of the quantum dots leads to a small absorption cross-section, which means growing of high density dots as well as stacking multiple QD layers are very important for the solar cell device to operate. Secondly, small dots are desirable as they have less confined energy states and shallower confinement which are important characteristics for easier extraction of photo-generated carriers and higher current collection efficiency. Finally, due to the accumulation of the strain and the tendency to form dislocations, the growth conditions must be carefully controlled to achieve defect-free QD structures. However, for the growth of self-assembled quantum dots (QDs) by MOCVD, there are two main challenges [4, 5]. First, growth kinetics plays a much greater role which results in a fast nucleation process and an increased tendency to form coherent islands. This is partly due to the higher growth temperatures used in the MOCVD reactor (50-100 ℃ higher than that of MBE) to ensure enough pyrolysis of the precursor sources. On the other hand, the use of in-situ monitoring techniques in MOCVD is limited, making it difficult for precise control of the quantum dot formation.

There are several main parameters which could be adjusted to optimize the growth of $In_{0.5}Ga_{0.5}As$ quantum dots during MOCVD growth. Among them, growth temperature, V/III ratio and deposition time are critical to obtain QDs with the desired dimension and density. Normally the growth temperature for planar InGaAs in MOCVD is between 600 and 650 ℃, however the temperature should be optimized for $In_xGa_{1-x}As$ dots. When growth occurs at 570 ℃ or higher, clustering and dislocations may take place due to increased mobility, which will lead to low quantum dots quality and large size distribution. But if temperature is below 550 ℃, low cracking efficiency of precursors will result in poor material quality. According to previous study on

$In_{0.5}Ga_{0.5}As$ dots growth [6], 550 ℃ was selected in this thesis for the growth temperature of the quantum dots. Also, the ratio of the amount of group V source to that of group III (V/III ratio) is an important factor in quantum dot formation. During MOCVD growth process the group V material (AsH_3) is in excess and is a thermodynamic requirement to suppress decomposition of the III-V semiconductor layers [7]. It was found that the dot density is affected by this factor [2, 5, 8], a higher V/III ratio will cause a decrease of the dot density and the formation of larger dots with higher In content. However, dot material quality becomes poor at very low V/III ratios. A V/III ratio of 18.25 was chosen for the growth of quantum dots in this thesis. Apart from these two factors, amount of material deposited that is determined by the deposition time plays an important role in the formation of quantum dots. Generally, with increasing material deposition dots will form with higher density until a saturation point is reached. Soon after the density saturation point, clusters and dislocations form and a red-shift in the photoluminescence will be observed.

In addition, quantum dot volume is relatively small to get sufficient absorption for QD solar cells to work effectively. In general, stacking multiple QD layers is essential to enhance the total QDs volume and hence their absorption, and efforts are made to increase optical absorption by growing larger number of stacked QD layers. The method of increasing the stacking number of QD layers and thus the total QD absorption has been reported by Hubbard S.M. et al and Takata A. et.al [9, 10]. However, though multiple QD layer stacking is one promising way to increase the total QD density thereby increasing the optical absorption, it is difficult to maintain the size homogeneity and structural quality of these structures. Because when more QD layers are grown on top of other layers, the formation of new dots will be affected by those underneath due to strain accumulation and dots coupling. The build-up of internal lattice strain with increased number of layers results in an increase in both the size and its fluctuation for QDs grown by S-K growth mode [10, 11]. Furthermore, the excess strain can have negative effects on QD device overall performances, mainly due to the formation of defects such as dislocations and degradation of bulk GaAs materials grown above QD layers [10, 12-14]. Therefore, the number of QD layers needs to be investigated and controlled within a reasonable number.

In this chapter, 10-layer $In_{0.5}Ga_{0.5}As$/GaAs QDSC structures grown with three different QD deposition time were studied by atomic force microscopy (AFM), photoluminescence (PL) and transmission electron microscopy (TEM). Various characteristics of the fabricated solar cells such as

temperature dependent I-V, spectral response/quantum efficiency were investigated in detail to reveal fundamental mechanisms behind QDSC behavior. With the attempt to achieve intermediate band solar cells (IBSC) by incorporating QD/WL structure, 2-photon absorption feature of the QDSC was investigated. Finally, QD solar cell structures with 15, 20 QD layers were grown and studied in comparison with the 10-layer device.

3.2 Experimental

The self-assembled $In_{0.5}Ga_{0.5}As$/ GaAs QD solar cell structures were grown on n^+ GaAs (001) substrates by metal organic chemical vapour deposition (MOCVD) as detailed in Chapter 2. A GaAs p-i-n structure was also grown as a reference. The vertical layer structure of QDSC and the control p-i-n cell structure are illustrated in Figure 3.1. Si and Zn were used as the dopants for n- and p-type doping respectively. The doping concentrations are 2×10^{17} and 2×10^{18} cm^{-3} for n^- and n^+ GaAs layers, and 5×10^{17} and 1×10^{19} cm^{-3} for p^- and p^+ doped layers, respectively. Specifically, the intrinsic region of the QD solar cell consists of ten undoped $In_{0.5}Ga_{0.5}As$ QD layers (6-monolayer thick each) sandwiched between 50 nm undoped GaAs spacers. All doped layers were grown at 650 ℃, and the intrinsic GaAs layers including QDs were grown at 550 ℃. For comparison, the GaAs reference cell has a 500-nm thick intrinsic GaAs layer which was grown at the same temperature (550 ℃).

All samples were then fabricated into a few 1×1 mm^2 and 3×3 mm^2 mesa devices with Ti/Au bus line and grids contact deposited on the top surface of the device as p-type contact, and Au/Ge alloy on the back as n-type contact. After metallization the top (exposed side) 100 nm p^+ GaAs contact layer was removed by selective etching. All devices were fabricated and characterized without any anti-reflection coating. The relevant cell structures and growth have also been reported previously [15, 16]. The structural, optical and device characterization will be presented in the following sections.

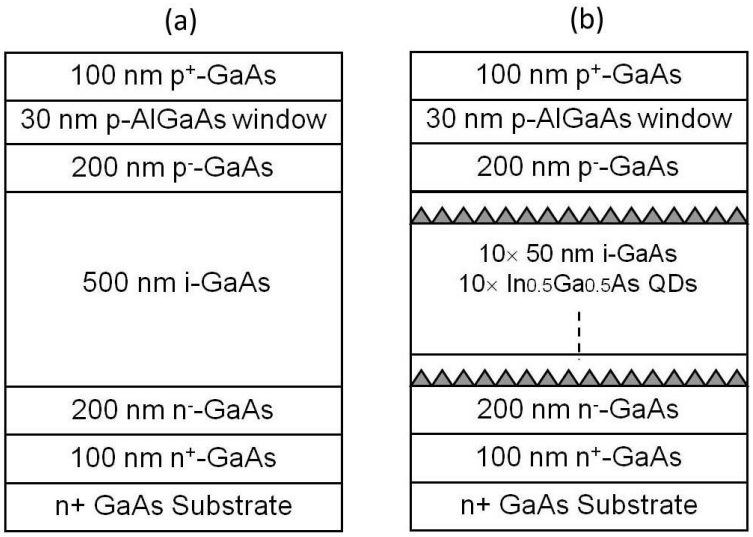

Figure 3.1: Schematic of the solar cell structure: (a) p-i-n GaAs reference cell and (b) 10-layer standard InGaAs quantum dot solar cell.

3.3 Material properties of quantum dot solar cell structures

3.3.1 Atomic Force Microscopy study

Atomic Force Microscopy (AFM) has been used as a routine technique to study the surface dot morphology, and dot density for $In_xGa_{1-x}As$/GaAs QDs [17]. To optimize the QD size and density for our solar cell structures, three QD structures were grown with the only variation of dot growth time.

The surface morphology of the $In_{0.5}Ga_{0.5}As$ QDs with the growth time of 3.3, 3.4, 3.6 s were measured using AFM and presented in Figure 3.2. Similar to what has been observed by other studies [1, 2, 5, 18], the dot density and size varies as a function of the amount of material deposited. When the dot growth time is increased from 3.3 to 3.4 s, the dot density is increased. However further increase of growth time to 3.6 s does not lead to increase of the density, indicating that saturation point is reached at a deposition time of ~ 3.4 s. Meanwhile, the QDs average size is increased with growth time. Also it is found that more clusters of larger dots are formed when the growth time is increased to 3.6 s (see Figure 3.2 (c)), which leads to more defects in the quantum dot layers [1, 4].

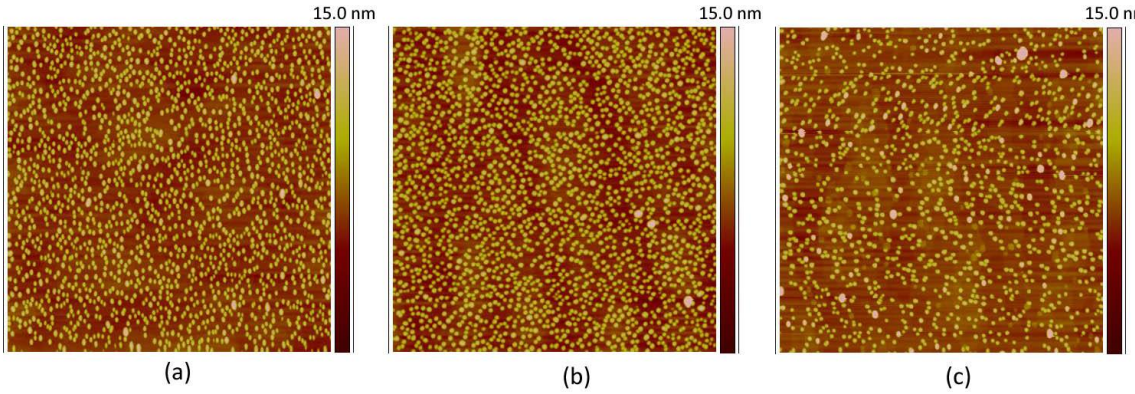

Figure 3.2: AFM images of QDs grown with different growth time: (a) 3.3 s, (b) 3.4 s, (c) 3.6 s. For all images the scales are 1 μm × 1 μm. The height profiles are shown by the colour bar.

The quantum dot density in a single layer that was grown for 3.3 s, 3.4 s, and 3.6 s were counted by ImageJ (an open source image processing program designed for scientific multidimensional images) [19] and listed in Table 3.1 below. The highest QD density is obtained from 3.4 s sample, the density is estimated at 4.5×10^{10} cm^{-2} for Figure 3.2 (b).

Table 3.1: Surface dot density for QDSC structures grown with different dot growth time.

Growth time/s	**Quantum dot density/cm^{-2}**
3.3	3.9×10^{10}
3.4	4.5×10^{10}
3.6	3.2×10^{10}

3.3.2 Photoluminescence

The room temperature photoluminescence (PL) spectra from these three QD samples with different dot deposition times are shown in Figure 3.3. For each sample, there are two distinct PL peaks originating from the QD and wetting layers respectively, indicating the high optical quality of our QDSC structures with a dominant radiative recombination process.

During the 2D-3D transition process the emission peak from the wetting layer (WL) (take 3.3 s sample for example) is blue-shifted from that expected for the nominal composition of $In_{0.5}Ga_{0.5}As$ materials [8]. This is mainly due to the quantum confinement effect for the ultra-thin wetting layer (~6 ML). Also, inter-diffusion between the InGaAs WL and GaAs layer changes the composition of the thin WL and lead to lower content of In, and thus a shorter

wavelength. The other peak at longer wavelength comes from quantum dots that have been formed. As more WL material transforms into QDs with the increase of dot growth time, the QDs grow in size with the intensity of QD peak becomes stronger and that of the wetting layer becomes weaker. The increase in the ratio of PL intensity of QDs to WL with dot growth time can be seen clearly from Figure 3.3. Also, the peak position of QDs is red-shifted with longer deposition time after 3.4 s, which is due to the formation of larger QDs which have lower ground state energy. In addition, the full width at half maximum (FWHM) becomes slightly larger for longer growth time (FWHM values of QDs are 85 nm, 92 nm and 103 nm for 3.3 s, 3.4 s and 3.6 s samples respectively), indicating that the QDs size distribution is less uniform beyond certain deposition time.

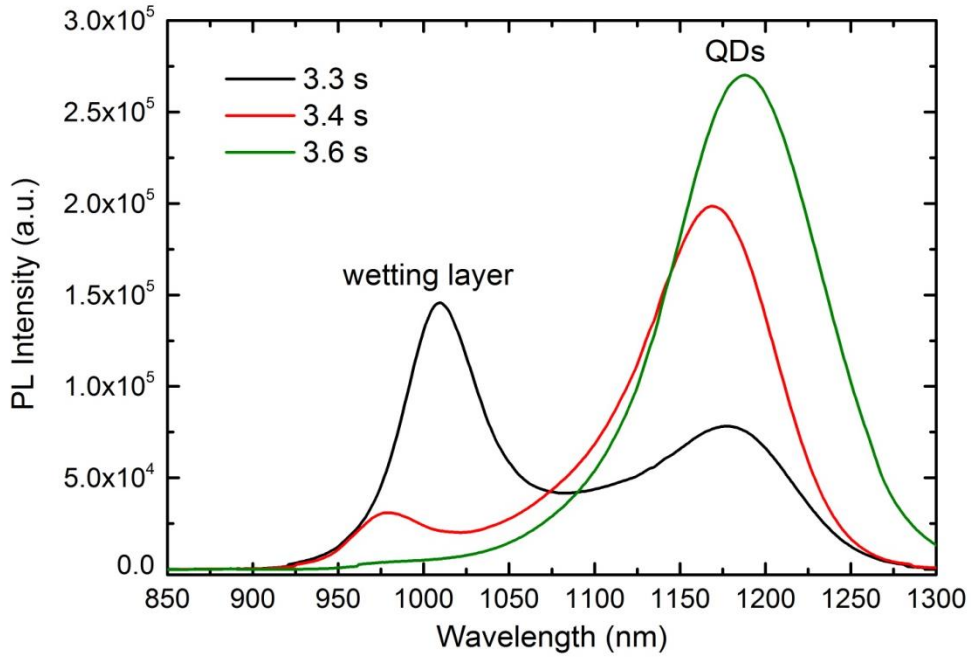

Figure 3.3: Room temperature photoluminescence spectra of $In_{0.5}Ga_{0.5}As$/GaAs QDs grown with different QD growth times.

Based on the above comparison from Figure 3.2 and Figure 3.3, 3.4 s was chosen as the growth time for the QDSC samples investigated in this work, since it provides the highest QD density and minimum cluster defects.

3.3.3 Transmission Electron Microscopy

As mentioned earlier, in order to achieve sufficient light absorption, multiple stacked QD layers is normally required in QDSC structures. However, due to

the strain-driven self-organizing growth process and thus the accumulated strain with the increasing number of layers, the QD growth conditions are extremely critical for achieving defect-free multi-layer stacked QD structures. There is the tendency for dislocations to form in one layer and propagate throughout the whole multi-layer structure, which may lead to a large V-shaped defects and thus much degraded device performance [20]. To further evaluate the material quality of our QDSC structures, cross-sectional transmission electron microscopy (TEM) analyses were carried out. Also, bright field scanning transmission electron microscope (STEM) was used for structural observation. Since growths were carried out on (100) wafers, the cross-sectional STEM and TEM images are close to one of the <110> directions.

Cross-sectional bright field STEM image for the 3.4 s sample is shown in Figure 3.4. Well defined layer structure is clearly displayed, which is in good agreement with the nominal structural design shown in Figure 3.1 (b). The structure consisting of the different layers are clearly visible. GaAs, InGaAs and AlGaAs layers appear gray, black and white, respectively, corresponding to their composition and relative average atomic weights [21].

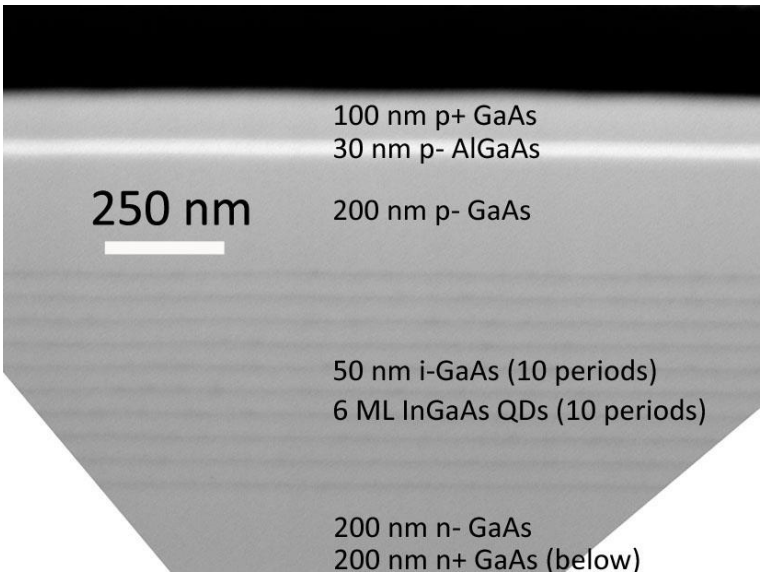

Figure 3.4: Bright field cross-sectional STEM image showing the whole quantum dot solar cell structure, in which the different layers are clearly observed.

Furthermore, Figure 3.5 shows the higher magnification TEM images of the QD region. It can be seen that the 10 QD/WL layers are well aligned with no V-shaped or other types of line defects observed in the structure. In addition, high resolution image in Figure 3.5 (c) indicates that no dislocations exist

across the GaAs barrier and InGaAs QD/WL interfaces. The strain accumulation is properly controlled by current growth conditions.

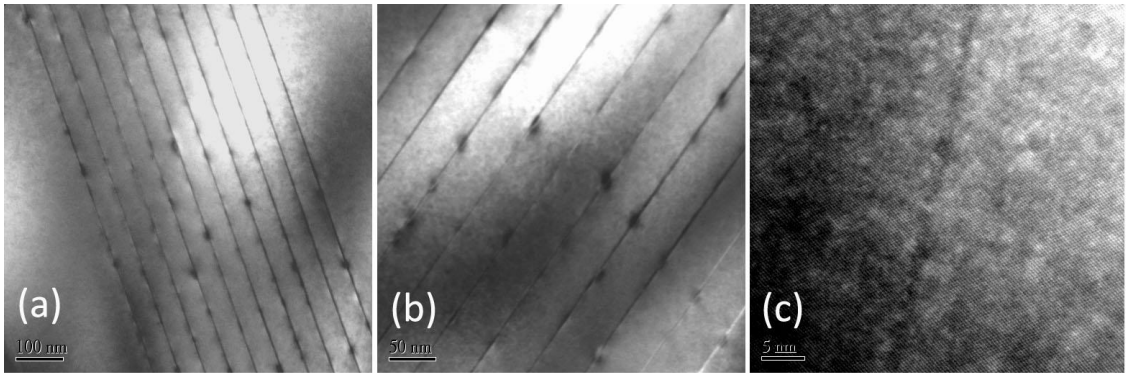

Figure 3.5: (110) cross-sectional TEM view of the 10-layer QDSC at three different magnifications, where (c) is the high resolution image.

3.4 Device performance of quantum dot solar cells

The device performance of the standard 10-layer quantum dot solar cells (QD growth time 3.4 s) were measured by an Oriel solar simulator under 1 Sun, AM 1.5 G illumination. The p-i-n GaAs control cell was also tested as a reference. I-V characteristics of both devices are plotted in Figure 3.6. The main solar cell parameters are extracted from the I-V curves and listed in Table 3.2.

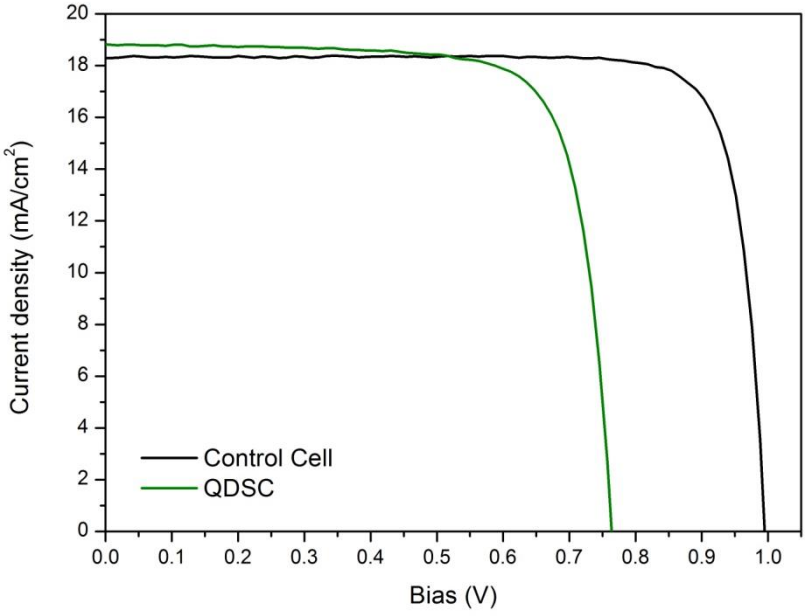

Figure 3.6: Current density versus applied bias curves for QDSC and control cell without the QD structure.

As seen in Table 3.2, the GaAs control cell shows an open circuit voltage (V_{oc}) of 0.99 V, short circuit current density (J_{sc}) of 18.3 mA/cm^2, fill factor (FF) of 83.9 % and conversion efficiency of 15.3 %, while the QDSC exhibits a slightly higher J_{sc} of 18.8 mA/cm^2, a reduced V_{oc} of 0.76 V, FF of 76.9 % and efficiency of 11.1 %. These results are consistent with the results obtained from some other studies based on different III-V group QD systems, i.e. higher J_{sc} is achieved in the QDSC however with degraded V_{oc} compared with control cell [22-24].

The value of V_{oc} of a solar cell is determined by the built-in potential (V_{bi}) which is equal to the splitting of the Fermi levels of the base and emitter layers: $V_{bi} = (E_{Fn} - E_{Fp})$. Both the reference and QD cells have the same doping scheme structure through the whole p-n junction, in theory they should have almost the same V_{bi} [15] and also the V_{oc}. But the behaviours are quite different for these two devices measured at room temperature. This phenomenon indicates that the existing of the QD layers changes the solar cell band structure. As a result, the potential between Fermi levels E_{Fn} and E_{Fp} is reduced so that the actual V_{bi} of QDSC dropped. Furthermore, it is the result of thermal injection of carriers into the QDs and subsequent recombination in the depletion region, which changes the forward injection thermal activation energy (E_a) [15], as will be discussed in detail in section 3.6.2.

For QD solar cells the absorption of lower energy photons by the QD layers are able to make additional contribution to the photocurrent, and leading to an increase of the J_{sc}. However, to understand the reason for the significant V_{oc} degradation of QD cell, it is important to investigate the I-V characteristics to obtain a deeper insight into the carrier transport and recombination processes within the QD region. Therefore, temperature dependent light and dark I-V characteristics of both reference and QD solar cells were measured over a wide temperature range from 30 to 310 K and discussed in section 3.6.

Table 3.2: Solar cell parameters measured under 1-sun condition at 298 K.

Samples	Jsc (mA/cm^2)	Voc (V)	FF (%)	Efficiency (%)
Control cell	18.3	0.99	83.9	15.3
QDSC	18.8	0.76	76.9	11.1

3.5 Quantum efficiency and spectral response of quantum dot solar cells

3.5.1 External quantum efficiency

As introduced in Chapters 1 and 2, external quantum efficiency (EQE) is an important parameter that reveals more detailed information of a solar cell performance. EQE measurements were performed at the short circuit condition. The results of both reference and QD devices are shown in Figure 3.7 together with the room temperature QD sample PL. The QD ground state recombination peak at ~1168 nm and the WL ground state recombination at ~978 nm can be correlated with the corresponding photocurrent peaks originated from QD related absorption in EQE. The sharp drop in efficiency at ~865 nm indicates the band gap energy of GaAs layers. Beyond this point, QDSC still exhibits peaks that are due to WL and QDs, indicating the QD structure can effectively broaden the solar cell response region by absorbing more long-wavelength light. The extended absorption and photocurrent result in short-circuit current enhancement compared to reference cell as observed in the section 3.4. As expected, QD device does not exhibit enhanced EQE than the reference cell in the short wavelength region (< 865 nm), indicating that there is no observable photocurrent contributed from QD structure absorption. The usage of high energy light is not improved by introducing QD structure with low energy band gap.

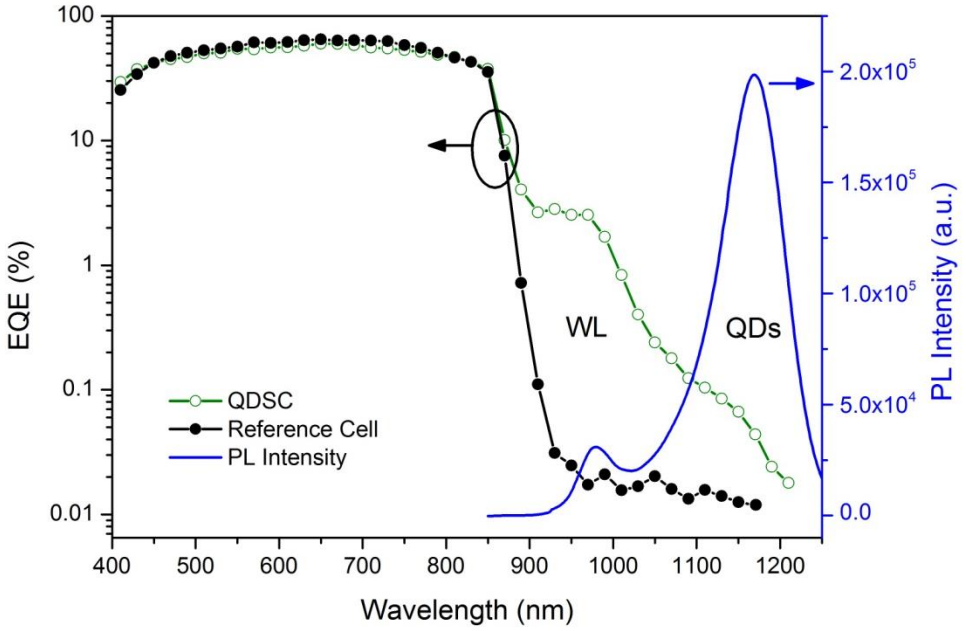

Figure 3.7: Comparison of EQE of QDSC and reference devices. The room temperature PL of QDSC is also plotted against the right axis.

3.5.2 Temperature dependent spectral response

In addition to the room temperature EQE measurements, study of spectral response at different temperatures and voltages allows further insight into the effects of carrier transport and recombination on QDSC electrical properties. In this section, a tungsten lamp was used as light source, because it was calibrated differently compared to the Xenon lamp used in solar simulator, the relative intensity of various peaks in the spectral response curves may be different from those obtained in the EQE measurement. However, they reveal the same physical information if comparisons were made between different samples under the same light illumination intensity. Moreover, spectral response measurements can be performed under different biases and temperatures for more detailed analysis of the carrier generation, recombination and collection processes.

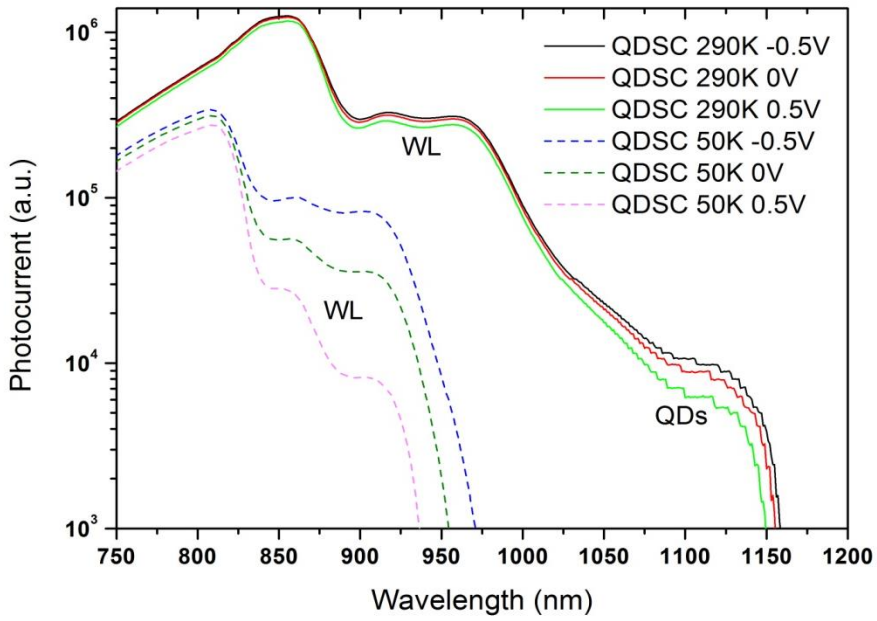

Figure 3.8: Spectral response of the 10-layer QD cell for different temperatures and applied biases.

The spectral response results at two temperatures with an applied bias of -0.5 V, 0 and 0.5 V are displayed in Figure 3.8. It can be seen at 290 K, a clear photocurrent peak at ~1150 nm is observed for QD device regardless of the polarity of the applied biases. Negative voltage improves the photocurrent slightly due to field-assisted tunneling and thus lower carrier capture probability, but its weak dependence on bias indicates that there is only a very small amount of recombination [15]. The two peaks in the spectral response that are located at 957 and 917 nm are due to wetting layer excitations. However, for the low temperature (50 K) curves no QD peak is present for all

bias conditions, and only photocurrent from bulk GaAs and WL can be observed. It implies a large amount of recombination occurs in QD layers because the thermal energy is too small for carriers to escape the confinement potential. Also the photocurrent under negative bias is increased dramatically over the whole range compared to the case of positive bias, particularly in the wavelength region of the WL. The contribution of electric field polarity to the photocurrent is more substantial at low temperatures.

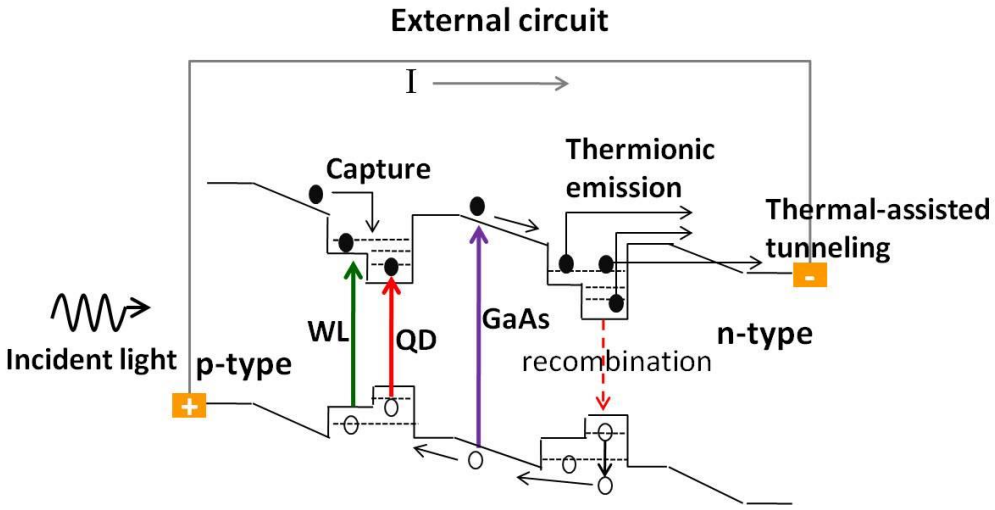

Figure 3.9: The schematic demonstrates the band structure of QDSC (taking two QD layers for example), in which related mechanisms of photocurrent are shown.

In general, for photogenerated carriers to result in an external current they must cross the intrinsic region and join the corresponding majority carriers in the contact layers. As shown by the schematic in Figure 3.9, in the process of getting through the whole QD device, carriers may be trapped in the QD layers, and they can escape the confinement potential by either optical or thermal excitation to barrier states or by direct tunneling to the adjacent layers. Direct tunneling probability through thick barrier is relatively low and therefore either thermal or optical excitations are the main processes for the QDSC studied here. For the relatively low light intensities used in the spectral response measurements (also for the condition of unconcentrated sunlight) the optical excitation rate of carriers out of the bound states would also be a slower process [15]. So the thermal excitation is the dominant process that makes carriers escape from confinement potential. However, there are two main competing processes for the photogenerated carriers: (1) thermal excitation out of the QD states and subsequent drift under the built-in electric field or (2) capture from barrier states or QDs/WL layers to QD states with possible further radiative recombination. The carrier escape time constant t_1 is dependent on temperature and it is expected that it would be longer compared

to the recombination lifetime t_2 of the trapped carriers over a certain temperature range. Also, the capture probability is related to the electric field across the p-n junction. Therefore the amount of recombination of the photocurrent should be sensitive to both the temperature and external bias.

3.6 Investigation of temperature dependence of I-V characteristics of quantum dot solar cells

Short-circuit current (I_{sc}) is dependent on the generation and actual collection amount of light-generated carriers. For an ideal solar cell, the short-circuit current and the light-generated current are identical, therefore, it is the largest current which may be extracted from the cell. The open-circuit voltage (V_{oc}) corresponds to the amount of forward bias when the dark current (I_{dark}) and I_{sc} exactly cancel out as indicated in Figure 3.10.

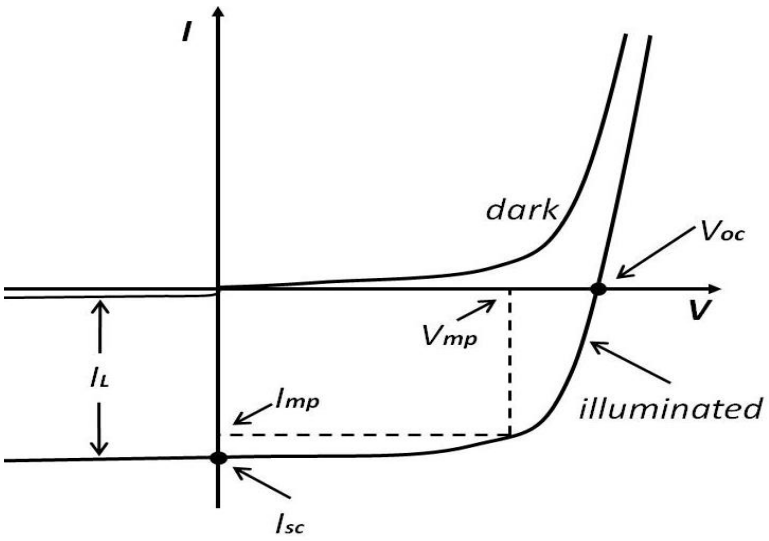

Figure 3.10: The typical light and dark I-V curves of a solar cell device.

As introduced in Chapter 1, solar cells can be modelled as a current source in parallel with a diode. When there is no light present to generate current, the solar device behaves like a diode. Therefore, I-V measurement is a powerful tool in examining the diode properties of solar devices. Under illumination, small fluctuations in the light intensity may add considerable amount of noise to the device making it difficult to obtain precise current signal. Dark I-V measurements use injected carriers into the circuit rather than with light generated carriers. The linear plot of dark current versus voltage reveals very little information about the diode, more information is revealed from a semi-

log plot, different regions of the I-V curves might be dominated by different mechanisms.

As the intensity of incident light increases, more current is generated by the solar cell. In an ideal cell the total current I(V) is equal to the short-circuit current I_{sc} minus the dark current I_{dark} according to the equation (3.1):

$$I(V) = I_{sc} - I_{dark}(V) = I_{sc} - I_0(e^{qV/nk_BT} - 1) \quad (3.1)$$

where I_0 is the saturation current of the diode, q is the elementary charge 1.6 x 10^{-19} Coulombs, k is the Boltzmann constant of value 1.38 x 10^{-23} J/K, T is the cell temperature in Kelvin, and V is the voltage across the solar cell, either produced or applied.

3.6.1 Temperature dependent light I-V analysis

I-V characteristics measurement is the most essential measure of solar device performance, from which the fundamental mechanisms could be revealed. Light I-V curves were measured at various temperatures to investigate the effects of the injected carriers recombination on V_{oc} and the total photocurrent extracted from solar cells. Light from a halogen tungsten lamp (250 W, ~ 3000 K) with the spectral range of 400- 1200 nm was used in this experiment to explore the influence of carrier transport and recombination at various temperatures and biases. The light was focused onto the solar cell devices under a similar optical setup to what has been used in PL, EQE measurement. The temperature dependent I-V curves from 30 to 310 K for both QDSCs and GaAs reference cell are shown in Figure 3.11. The reference cell shows steady photocurrent along with different voltages at all temperatures. For QDSC, obvious voltage dependent photocurrent is observed which results in a poor fill factor especially at lower temperatures. This is because both the capture rate of photo-generated carriers into the QD layers and their escape from quantum confinement to form photocurrent are affected by electric field in the p-n junction, leading to a voltage dependent recombination. The effective carrier tunnelling barrier width changes with different voltages, particularly when positive and negative biases are applied.

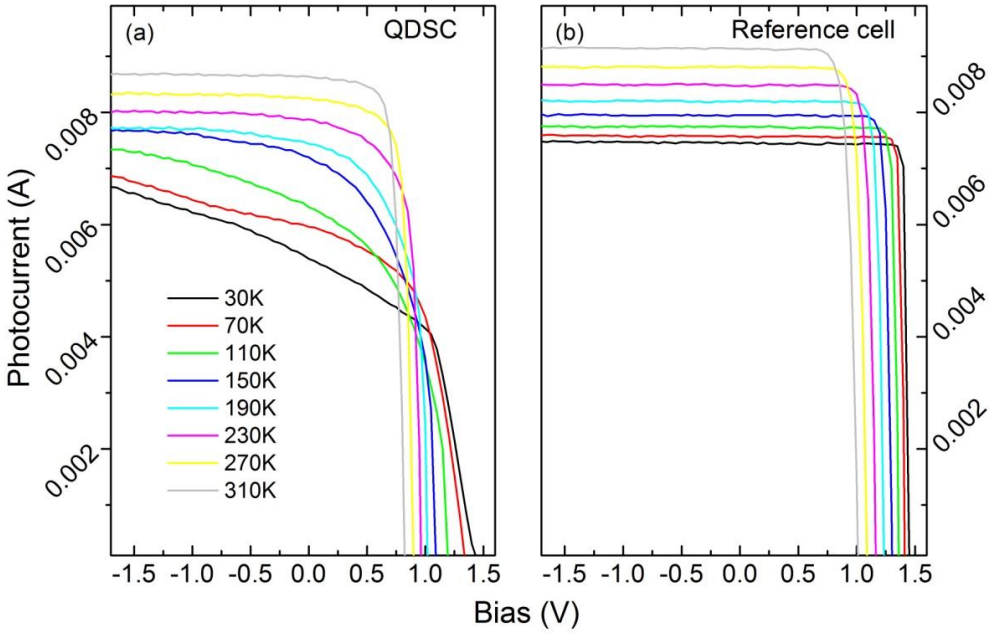

Figure 3.11: Current-voltage curves of the QD and reference solar cell exposed to light from a halogen tungsten lamp for various temperatures.

In spite of the large amount of photo-generated carrier recombination, V_{oc} of the QD cell at low temperatures is very close to that of reference device, the value is determined by the built-in potential (V_{bi}) which is equal to the splitting of the Fermi levels of the base and emitter layers: $V_{bi} = (E_{Fn} - E_{Fp})$. Because both the reference and QD cells have the same doping scheme structure through the whole p-n junction, it is assumed that they have almost the same V_{bi} [15]. This phenomenon indicates that the reduction of the QDSC V_{oc} at relatively high temperatures is the result of thermal injection of carriers into the QDs and subsequent recombination in the depletion region, which changes the forward injection thermal activation energy (E_a) [15], Figure 3.13 (c) in next section will demonstrate the mechanism of E_a reduction.

3.6.2 Temperature dependent dark I-V analysis

Many investigations based on the study of I-V characteristics have been performed to understand the effects of quantum structure on solar cell properties [25, 26], however the dark current properties which are critical for the QD solar cell performance have not been studied in-depth previously. In this section, we present a detailed study of the temperature dependent dark current of $In_{0.5}Ga_{0.5}As$/GaAs QD solar cells. The temperature dependent I-V characteristics were carried out in a close-cycled He cryostat using a Hewlett-Packard 41408 voltage source and pico-ammeter as mentioned in section 2.6.3.

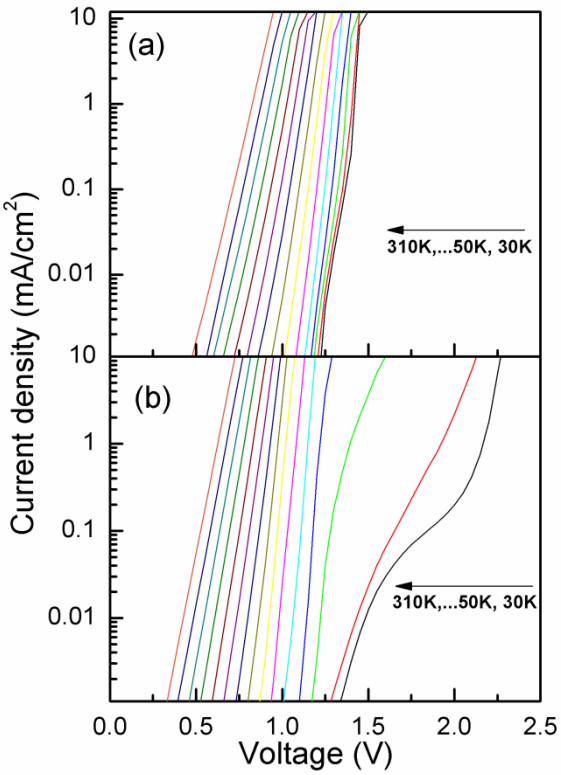

Figure 3.12: Temperature dependent dark J-V characteristics of the (a) reference GaAs solar cell and (b) QD solar cell.

As shown in Figure 3.12 (a), the GaAs reference cell displays a steady increase of dark current with temperature at a fixed voltage, mainly as a result of the exponential temperature dependence of the intrinsic carrier concentration n_i in the depletion region [27]. However, the QD device exhibits a more complicated behaviour (Figure 3.12 (b)). At low temperatures, the QD cell has much smaller dark current than that of the reference cell, however, its dark current increases more rapidly with temperature and when the temperature is over 70 K, the dark current of the QD solar cell follows a trend similar to that of the reference cell. Generally, for a normal p-i-n solar cell structure, the dark current due to the forward bias carrier injection is a combined result of recombination current in the space charge region (SCR) and diffusion current through the SCR. The change of the shape of the dark I-V curves with temperature depends on the concentration of different types of defects present in the sample with different temperature dependent carrier capture cross sections and tunnelling effects [28]. On the other hand, for the QD device, presence of QDs in the depletion region introduces additional recombination paths via QD states to contribute to dark current, the amount of which largely depends on the carrier capture and recombination processes

under different bias and temperature conditions. To discuss this more clearly, Figure 3.13 (a) re-plots the dark I-V curves of both devices at 30 and 300 K. At 30 K, as displayed in the region I in Figure 3.13 (a), the dark current of both the reference and QD devices remains very small and does not show substantial increase until a large voltage is applied. This is because at low temperatures, the kinetic energy of forward injected carriers is too small to overcome the built-in potential (V_{bi}) of the p-i-n junction to form appreciable dark current until the forward voltage is increased to a value close to V_{bi}[*]. For the QD solar cell the current is even smaller due to an additional potential barrier formed by the QDs carrier occupation [29]. In a similar manner to modulation doping, carriers in the doped contacts are captured by the QD layers. Those QD layers particularly close to the contacts will be occupied by carriers which will form an electrostatic barrier that inhibits further injection of carriers. This effect as shown schematically in Figure 3.13 (b) suppresses dark current even at biases larger than the V_{bi} (region II in Figure 3.13 (a)) where a large increase of dark current is observed for the reference cell. If the bias is further increased beyond 2.0 V the potential barrier formed by the carrier capture is overcome and the carriers start to be injected through the depletion region leading to a rapid increase of dark current with bias (region III in Figure 3.13 (a)).

[*] The V_{bi} for our GaAs reference cell is estimated to be ~ 1.36 eV at room temperature and ~ 1.5 eV at 30 K using the nominal doping concentrations of our solar cell structures. Here we assume our QD solar cell has a similar V_{bi} due to the same doping scheme in the structure.

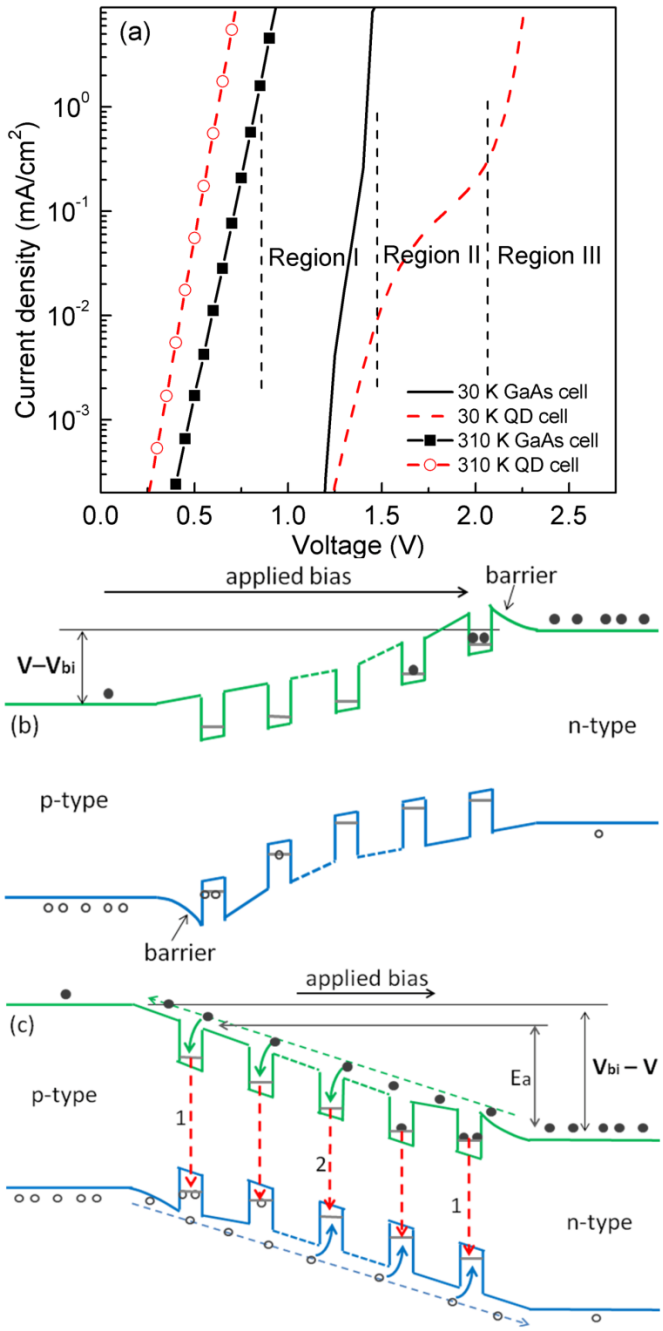

Figure 3.13: (a) Dark I-V characteristics of the solar cell devices measured at 30 and 300 K. Schematic diagrams demonstrating the different carrier capture and recombination behaviour for the QD solar cell devices at (b) low temperature (<70 K) and high bias condition ($V > V_{bi}$) and (c) high temperature (> 70 K).

The case is different at higher temperatures for QD device, e.g., > 70K, the thermal energy of carriers in the contact layers may overcome both the potential barrier formed by the trapping of carriers and the built-in potential. As the injected carriers pass through the depletion region, there is a high probability for them to be captured by the QD potential well and recombine via two different paths as demonstrated schematically in Figure 3.13 (c): 1)

For the QD layers that are close to the quasi-neutral regions, the majority carriers from the contact layers occupy QD states under a quasi-thermal equilibrium distribution. Under forward bias, these QD layers may capture injected minority carriers leading to recombination; 2) For those QD layers that are unoccupied (both conduction and valence bands), simultaneous capture of an electron and a hole by the same QD layer may also occur with subsequent recombination. These two paths will both cause a reduction of forward injection thermal activation energy (E_a) in the QDSC and increase of dark current [15], as observed previously.

Despite the complexity of dark current mechanisms, log(I)-V curves of both devices at relatively high temperatures turn out to be close to straight lines which can be fitted well using the modified one-diode exponential characteristic equation 3.2 [30, 31]:

$$J = J_0\left\{\exp\left[\frac{q(V - JR_s)}{nk_BT}\right] - 1\right\} \tag{3.2}$$

where J is the current density, V is the voltage across the device, J_0 is the reverse saturation current density, R_s is the series resistance, n is the ideality factor, q is electron charge and k_B is the Boltzmann constant. The fitting parameters for both devices at 300 K are listed in Table 3.3. The shunt resistances are also calculated using the slope of reverse current-voltage characteristics before breakdown and provided in Table 3.3. It is found that compared with the reference cell, the QDSC exhibits a larger R_s and smaller R_{sh}, which is consistent with its reduced FF (76.9 %) due to the large bias dependent carrier recombination in the QD samples. Its large saturation current suggests possible presence of significant defect concentration in the QD structures due to the strain driven self-assembled QD growth, as well as increased probability of thermal generation of carriers due to the small bandgap of QDs. However, surprisingly the ideality factor, n of the QDSC turns out to be smaller than that of the reference cell, which is contradictory to the rest of the results observed in QD devices implying larger amount of recombination. This could be due to the following reasons. For conventional solar cells, at relatively low bias conditions, the dark current is normally dominated by recombination occuring within the depletion region, which results in a smaller slope of dark log(I)-V curve and larger n value (more than 1). For the case of the QDSC, recombination within the QDs makes a large contribution to the dark current. We propose that the two different recombination paths within QD layers as mentioned earlier may have different contribution to the overall ideality factor of the QDSC. As demonstrated in

Figure 3.13 (c), under quasi-thermal equilibrium state, the first few QD layers will be occupied by majority carriers, which may then recombine with the injected minority carriers via path (1). This process is very similar to the formation of dark current outside the space charge region which requires the transport of only one type of charge carriers through the depletion region, giving a lower ideality factor (closer to 1). On the other hand, it is also likely that electrons and holes are simultaneously captured by the same QD layer and recombine directly via path (2). This process however, is associated with the QD capture cross sections for electrons and holes (which is inversely proportional to their respective lifetimes), and is similar to the defect related recombination in the depletion region of conventional solar cells leading to larger ideality factor (closer to 2). Apparently for the QDSC studied in this work, despite its larger dark current, the recombination in the first few QD layers contributes significantly to the dark current and consequently a smaller ideality factor than the GaAs reference cell.

Table 3.3: Fitting parameters for the dark I-V curves measured at 300 K.

Samples	J_s (A/cm^2)	R_s (Ω)	R_{sh} (Ω)	n
GaAs cell	2.08×10^{-11}	1.29	3.04×10^{9}	1.91
QD cell	1.39×10^{-10}	2.06	1.78×10^{9}	1.66

To further study the carrier recombination mechanisms in QD solar cells and their effects on ideality factor, the local ideality factor at various voltages can be approximated based on equation 3.3: [32]

$$n(V) = \frac{d(V/V_t)}{d\left[\ln(I)\right]} \tag{3.3}$$

where V_t is the thermal voltage of 0.026 eV at 300 K. n(V) of both GaAs reference cell and QD solar cell devices with two different sizes are plotted in Figure 3.14. Both types of devices show a change of n with voltage. In the low bias region, n is larger indicating dark current is dominated by recombination in the space charge region. Along with increase of bias, n of both devices reduces to the lowest value before a large increase due to the series resistance effect at high biases. It can be seen that the GaAs reference cells have larger n values than the QD devices. In addition, as displayed in Figure 3.14, the n(V) curves for the reference cells show fluctuations and sometimes with the presence of "peaks" in the curve, which imply additional path(s) of recombination, such as edge recombination caused by the lateral

spreading of current to the perimeter of a device. Though we have not observed any obvious size-dependent trend with these fluctuations, as have been reported previously in shallow mesa devices (to allow more lateral current diffusion) [32], the strong bias dependent n(V) curves of the GaAs control cells still imply the influence of the device edge and size variations. This is in contrast to the QD devices where consistent results have been obtained for all the devices with different sizes. All the QD devices have similar n value over the wide range of voltages. It suggests that similar to the dots-in-a-well devices [32], the use of InGaAs/GaAs QDs may be able to block lateral current flow to the device perimeter thereby reduce the edge recombination, which could be advantageous for many potential applications.

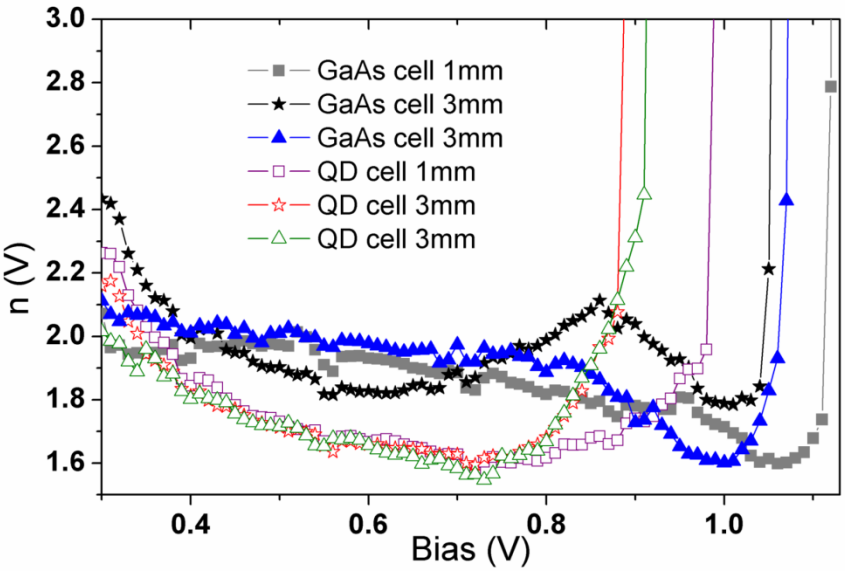

Figure 3.14: Voltage dependence of local ideality factor n(V) for various size solar cell devices.

Furthermore, it is expected that QD samples have higher defect density than the reference sample due to high strain, which may lead to the complicated dark current behaviours. Since it is difficult to quantify the effect of defects without knowing the defect types and its temperature dependent carrier capture cross section, comparison of dark currents from different QD structures grown under different conditions could be useful to provide further insight.

In summary, we have performed a comparative study on the temperature dependent dark current properties of GaAs p-i-n reference and InGaAs/GaAs QD solar cells. The QD devices exhibit much more complicated dark I-V behaviour due to the temperature and bias dependent carrier capture,

occupation and recombination via QD bound states. The results also revealed that for QD solar cell devices, the common one diode model for general interpretation of dark I-V characteristics may not be valid. To date, the unusual reduction of ideality factor of QDSC has not been reported and discussed. It suggests that for analysis of the dark I-V properties of the solar cell devices that incorporate nanostructures such as QDs, new physical model needs to be developed to take into account of their complicated recombination behaviours. These results are critical for better understanding of the fundamental properties of QD solar cells thus to stimulate new QD and/or solar cell designs for improved device performance.

3.7 Study of two-photon absorption process in quantum dot solar cells

Theoretical studies of intermediate band solar cells (IBSC) have predicted potential efficiencies of 63.2 % under full concentration condition for ideal solar cells [33-36], compared with the Shockley-Queisser limit of 40.7% for a conventional single junction device under the same conditions. The use of quantum dots for the implementation of IBSC has been proposed [37, 38], and many experimental and theoretical studies of quantum dot solar cells (QDSCs) have been reported [33, 37-40]. Based on the ideal theoretical picture of IBSC, when QD layers are incorporated into the intrinsic region of a p-i-n cell, the built-in potential should still be determined by the Fermi-level splitting of the doped emitter and base layers, as is the case for single junction GaAs solar cell. Therefore, it is possible for a QDSC to maintain the similar open-circuit voltage of the single-junction cell with an improved short-circuit current due to the extra contribution from the sub-bandgap quantum dot structures. However, as has been demonstrated and discussed in this chapter, QDs and the wetting layer influence not only absorption but also recombination and transport of carriers that in the intrinsic region, which tends to decrease the V_{oc} of the whole cell. Also, the strong QD confinement effect increases carrier recombination and thus decrease the amount of photocurrent.

On the other hand, to achieve IBSC, the two-photon absorption process is essential. Apart from the conventional semiconductor conduction band (CB) and valence band (VB), IBSC also contains an intermediate band (IB). Consequently, in addition to the electron transition between the VB and the CB, photo-induced transitions from VB to IB, and IB to CB can also take place. In this section, we investigate the two-photon absorption process in QDSC through temperature dependent inter-subband photocurrent measurements.

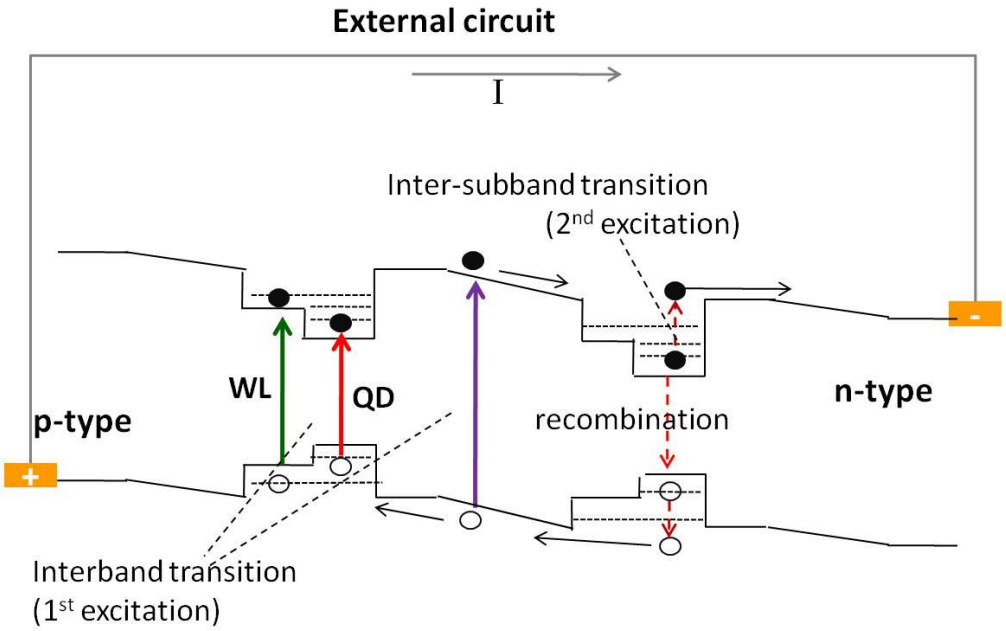

Figure 3.15: Simplified QDSC energy band diagram and the two-photon excitation process. Captured carriers can undergo inter-band transition (1st excitation), inter-subband optical transition (2nd excitation), or thermionic emission (2nd excitation), respectively.

As schematically demonstrated in Figure 3.15, when the light is shone on the QD solar cell, electron-hole pairs will be excited directly from the valence band to conduction band in both GaAs barriers and InGaAs QD structures (including QD states and WL states). This direct band-to-band transition normally only occurs via optical excitation, and it is defined here as the first photon excitation. For the carriers that are excited to the ground states of the QD and wetting layer, a second excitation (inter-subband transition as shown in the diagram) can be achieved by either optical absorption or thermionic emission. The two-photon excitation absorption process for QDSC is generally accepted regardless of the formation of continuous intermediate band of QDs [37, 41-43]. Although two-photon absorption process plays a vital role in the inter-subband optical transition, which is essential for QDSC theoretical models, very few experimental studies on this transition step have been reported [37, 44]. The determination of the various transition energy levels will depend on the composition, the strain, the band-gap discontinuities and the dimensions of the wetting layer and QDs. The QDs grown by MOCVD in this work are also probably not ideally shaped dots. It would be good to know if MOCVD grown dots are different in shape to those produced by other method such as MBE. Different dots sizes and shapes would affect

the theoretically predicted 0-D density of states. But in this section, we mainly focus on the optical inter-subband transition study through an analysis of the temperature dependent response of the $In_{0.5}Ga_{0.5}As$/ GaAs QDSC to infrared (IR) light that induces inter-subband transitions.

As relatively low energies (~100 meV) are required for inter-subband transitions, it can be induced by either low energy photons or thermionic emission. In order to examine the effect of thermal excitation, temperature dependent measurements are important. In this work, a specially designed experimental setup was used as illustrated in Figure 3.16. The quantum dot solar cell sample was mounted in a closed cycle cryostat with a BaF_2 window that allows optical transmission up to a wavelength of ~14 μm [45], which covers the intersubband transition energy range (wavelength < ~13 μm) of our InGaAs/GaAs QDs. In Figure 3.16, there are two optical paths. The first one has the white light from a tungsten lamp passing through the monochromator and incident on the device to populate the QD/WL/barrier states with the interband (first) photon, whereas for the second optical path a calibrated 800 ℃ blackbody radiation source with an internal chopper was used to produce infrared light to provide photo-excitation for the inter-subband transition. A Ge filter was used here to block the light with wavelength shorter than 1.88 μm. The output photocurrent was then amplified through a low-noise current amplifier and a lock-in amplifier and interfaced with a PC for collection. Since the blackbody signal was chopped as the reference for the lock-in amplifier, it is obvious that any photocurrent obtained here only correlates to the extra excitation from the blackbody source, namely the only second-photon excitation related process. For convenience, the photocurrent obtained through this technique is called inter-subband photocurrent in our work and is different from the photocurrent obtained earlier, which is called inter-band photocurrent.

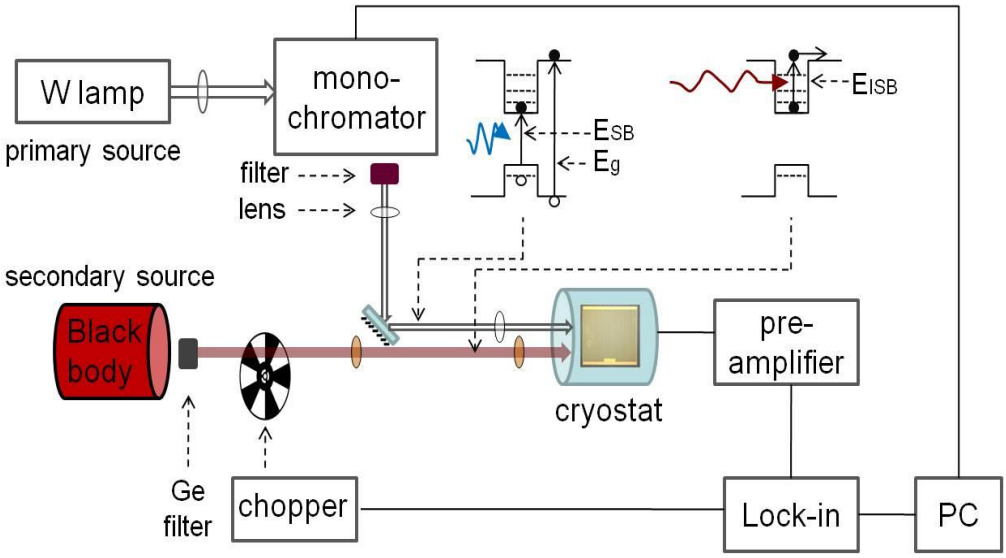

Figure 3.16: Schematic of inter-subband photocurrent measurement set-up.

The inter-subband photocurrent spectra measured at various temperatures are plotted in Figure 3.17, in comparison with the inter-band (VB-CB) photocurrent. Each spectrum is the result of two-photon processes where photons from the monochromator create electron-hole pairs, and photons from the IR source excite these carriers out of the QD/WL layers. The signal disappears when the first excitation light wavelength is beyond ~1010 nm, which is the WL ground state bandgap at low temperature, indicating that electron-hole pairs population produced from QDs VB-CB transition is too low to support the IR induced inter-subband process. It can be seen there is a clear trend that inter-subband photocurrent declines with increasing temperature and cannot be observed at temperatures greater than 70 K. This is because at higher temperatures the thermal energy is stronger and thermal transition now becomes the dominant excitation path. So it can be deduced that the thermionic emission time constant at room temperature would be many orders of magnitude smaller than the optical inter-subband excitation time constant, resulting in a negligible optical response above 70 K. Martíet al. [43] also obtained similar inter-subband photocurrent measurement results from a QDSC with delta doped QD layers that was cooled down to 36 K. Also, a small amount of photocurrent produced by two-step photon absorption in direct Si-doped InAs/GaNAs QDSC at room temperature was reported by Okada et al. [44]. All studies indicate that the second absorption (IB-CB) step is not very efficient to create effective photocurrent enhancement in these quantum dot based IBSC, indicating that it is important to improve long wavelength light absorption related processes to achieve high efficiency QDSCs.

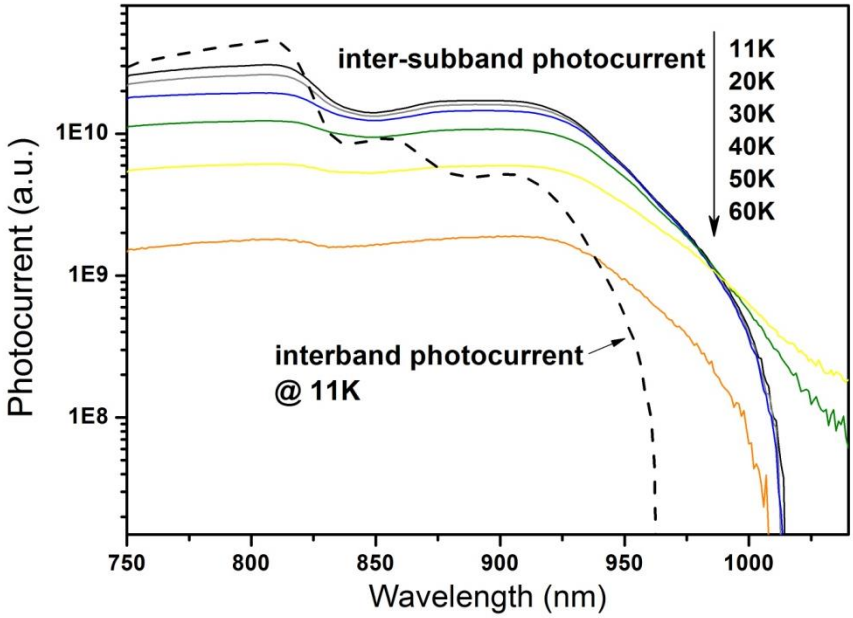

Figure 3.17: Inter-subband photocurrent spectrum of the QDSC device as a function of temperatures. Also shown is the inter-band response of the same device at 11 K.

3.8 Quantum dot solar cells with various number of QD layers

To further investigate the photon absorption and carrier collection properties of QDSCs, in this section we present a detailed study of the effect of the number of QD layers on the optoelectronic properties of QDSC structures. In addition to the photoluminescence (PL) measurements and device characterization, electroluminescence (EL) on QDSC samples containing 10, 15 and 20 layers of self-assembled $In_{0.5}Ga_{0.5}As$/GaAs quantum dots has also been studied. The EL characteristics of these devices were measured under different temperatures and carrier injection levels, with careful analysis of the EL peak position, intensity and line-width. We also demonstrate the optical and electrical characteristics of these three QDSC devices and study the influence of number of QD layers on overall device performance.

3.8.1 MOCVD growth of QDSCs with different number of QD layers

Three QDSC structures with 10, 15 and 20 layers of self-assembled $In_{0.5}Ga_{0.5}As$/GaAs QDs were grown by metal organic chemical vapour deposition with the structure schematic shown in Figure 3.18. Each sample has exactly the same p-type and n-type doped layers on each side of QD

structures as previously described in Section 3.2, with the only difference in the number of QD layers in the intrinsic region. All samples were then fabricated into 1x1 mm^2 devices with Ti/Au alloy as p-type contact (top) and Ge/Au alloy as n-type contact (bottom).

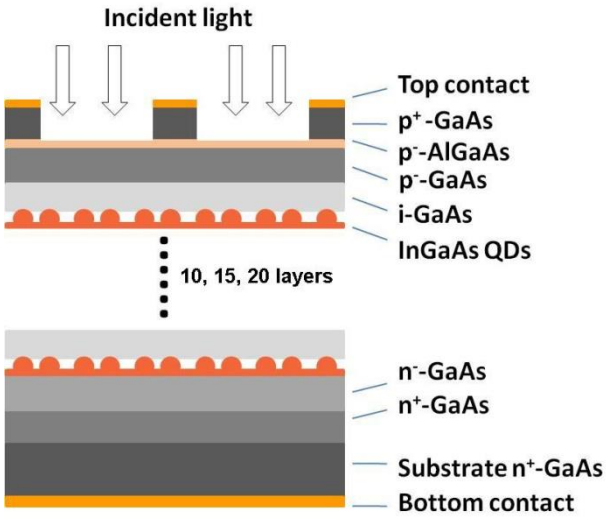

Figure 3.18: Schematic of the InGaAs/GaAs QDSC samples with different number of QD layers used in this study.

3.8.2 Photoluminescence

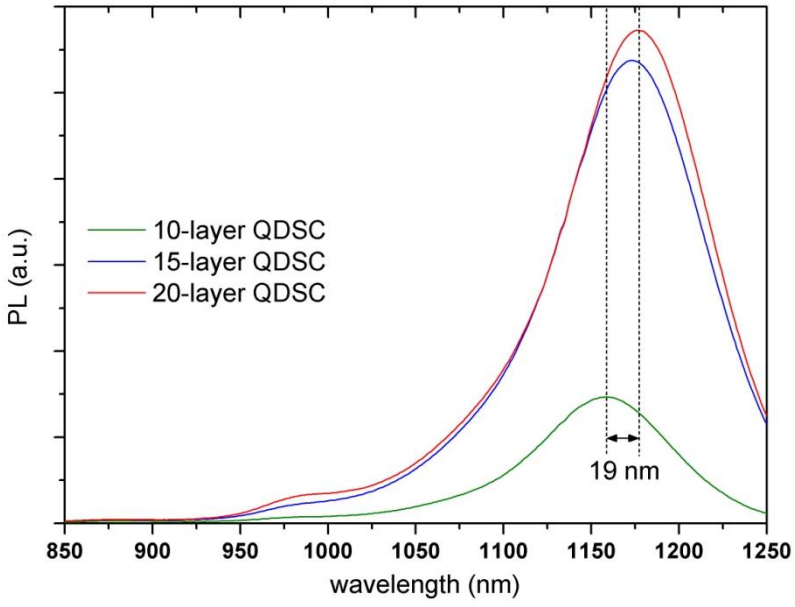

Figure 3.19: Room temperature photoluminescence curves of the three QDSC samples contain 10, 15, and 20 QD layers.

After growth, room temperature photoluminescence (PL) measurements were firstly performed on all three samples to check their optical quality, as shown in Figure 3.19. It is obvious that with an increased number of QD layers, the intensity of both the wetting layer (WL) and QD peaks are enhanced because of increased total absorption volume. The peak positions of WL and QDs are summarised in Table 3.4. The position of WL is almost the same for the three samples, indicating that the WL thickness and its indium composition almost remain the same for the three QDSC structures with different number of QD layers. However the QD peak position is red-shifted with more layers. This is due to increasing strain with increasing number of QD layers, which then lead to an increase in both the average size and size distribution of dots [10, 11]. Larger average QD size will result in lower ground state energy and thus the emission peak at longer wavelength.

Table 3.4: PL peak positions for the WL and QD for each of the QD structure.

	WL peak (nm/eV)	**QDs peak (nm/eV)**
10-layer QDSC	990 / 1.253	1156 / 1.073
15-layer QDSC	991 / 1.251	1172 / 1.058
20-layer QDSC	991 / 1.251	1175 / 1.054

3.8.3 Comparison of device performance

To compare the performance of these three different QDSC structures, the samples were fabricated into standard solar cell devices and their I-V characteristics were measured under AM 1.5G 1-sun irradiation, as plotted in Figure 3.20. Figure 3.20 (a) shows that more QD layers incorporated in the solar cell result in much more degraded performance. In particular, there is a significant decrease in J_{sc} from 18.9 mA/cm^2 for 10-layer QDSC to 1.25 mA/cm^2 for 20-layer stacked solar cell, leading to the overall efficiency dropped from 10.53 % to 0.64 %. The open-circuit voltage was also reduced slightly compared to that of standard 10-layer device. The other important solar cell parameters are also extracted and listed in Table 3.5. Despite of the improved PL intensity obtained from the structure with more quantum dot layers, surprisingly all the major device parameters are degraded. As reported by other researchers, when the number of the QD layers is increased beyond a certain value, degraded device performance has also been observed, which has

been partially ascribed to the degradation of p-GaAs emitter layer which results in low minority carrier lifetime and short diffusion length [9, 10, 14].

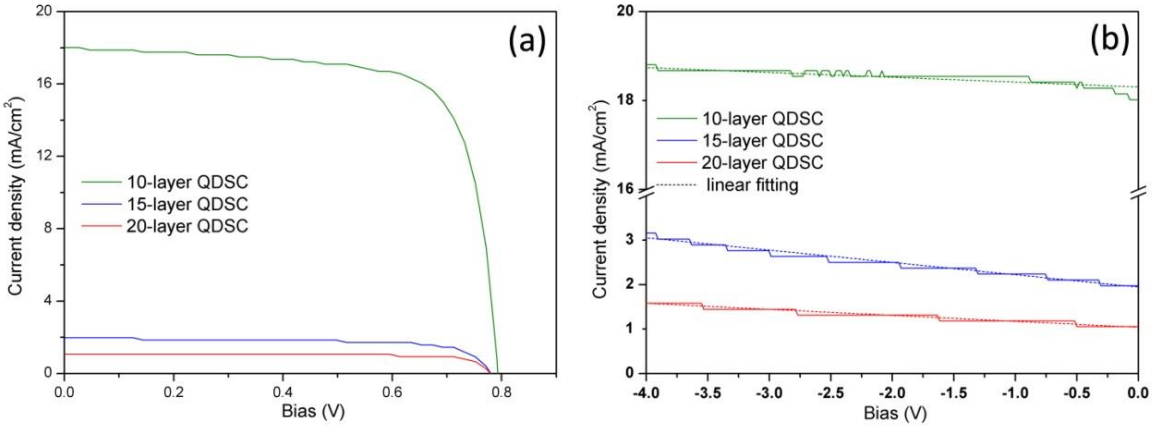

Figure 3.20: Light I-V characteristics at (a) forward bias region, and (b) large reverse bias region for QDSCs with varied stacking layer.

To qualitatively understand carrier extraction efficiency in our QDSC structures, the light I-V characteristics at negative bias region are shown in Figure 3.20 (b). It is found that compared with the 10-layer sample, the 15, 20-layer devices exhibit more obvious bias dependent photocurrent. This behaviour indicates that although higher stacked layers can result in more QD absorption, it makes carrier extraction process more difficult, which could be due to the reduced built-in electric field strength and increased QD size with the increase of number of dot layers. The built-in electric filed strength is reduced because the depletion width increased obviously. This behaviour is similar to the reported 50-layer InAs/GaAs and 100-layer InAs/GaNAs strain-compensated QDSCs [10, 14].

Table 3.5: The solar cell key parameters of samples with varied stacking layers.

	J_{sc} (mA/cm^2)	V_{oc} (V)	Fill Factor (%)	Efficiency (%)
10-layer QDSC	18.92	0.774	73.67	10.53
15-layer QDSC	2.53	0.751	70.48	1.07
20-layer QDSC	1.25	0.751	77.25	0.64

Further temperature dependent spectral response measurements were carried out to study the recombination properties in the three QDSC devices.

Figure 3.21 (a) shows the spectral response measured for these three devices at 50 and 290 K. The corresponding electroluminescence curves are also plotted in Figure 3.21 (b) to confirm the peak positions.

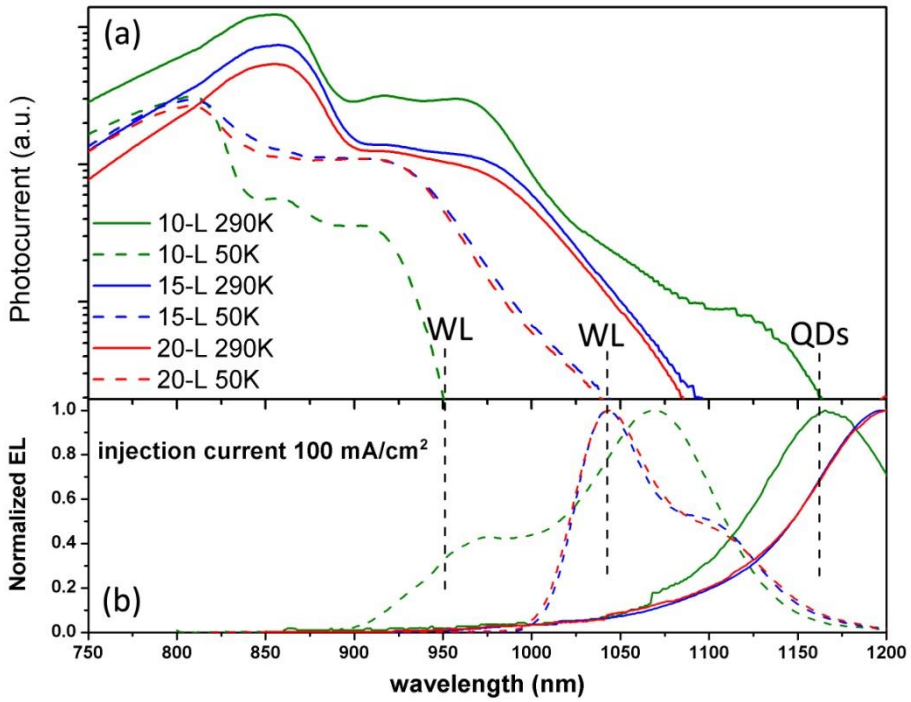

Figure 3.21: (a) Spectral response of three samples measured at 50 and 290 K, (b) the corresponding EL curves at the injection current density of 100 mA/cm^2.

At 290 K the highest photocurrent has been obtained from the QDSC contains 10 layers of quantum dots. Across the entire spectral range, it collects much higher photocurrent than those devices with 15 and 20 layers of QDs. Furthermore, it is also the only device that exhibits the detectable photocurrent contributed from the quantum dots (around 1160 nm wavelength as confirmed by the EL peak underneath). This means the photo-generated carriers from the QD layers in the other two samples are not able to be collected. The much reduced photocurrent of 15 and 20 layers samples observed in Figure 3.20 could be due to two main reasons. Firstly, the increase of number of QD layers will lead to an increased width of depletion region. The same built-in potential is assumed for all three devices, which is mainly determined by the solar cell structural design and p-n junction doping scheme [46]. Therefore, the photo-generated carriers have to go across a longer distance to reach the contact layers to form effective photocurrent in the external circuit, where there will be larger probability to be captured in the QD layers. On the other hand, due to the strain-driven growth method, more

QD layers could result in more strain and possible formation of defects in the quantum dots region which act as non-radiative recombination centres. Also, there is a chance to form strain-induced dislocations that propagate towards the p-GaAs emitter side from the QD region. Similar results have been reported by other research groups for QDSCs but in different material systems [3, 10, 39, 47]. With decreasing temperature, neither device shows the photo response from the QDs, because the escape time constant of photoexcited carriers from quantum confinement becomes longer than the capture and recombination time [48, 49]. At low temperature, it is interesting to find that the 15 and 20-layer devices present a higher photocurrent than the 10-layer (defined as standard) sample in the WL wavelength region as can be seen from Figure 3.21 (a). This phenomenon can be correlated to the EL emission features in Figure 3.21 (b), where the carriers have a higher probability to be captured in wetting layer than the QDs states for these two samples. The fundamental mechanisms behind this are not very clear, however, this feature may result in stronger photoresponse from WL for these two devices.

3.8.4 Electroluminescence

Electroluminescence (EL) is the spontaneous emission when current is injected into a p-n junction from external circuit. It is also considered a helpful tool for optoelectronic devices characterization. The injection current level can be adjusted so that the solar cells properties can be studied at various photocurrent density levels corresponding to cell operation under concentrations. Some details of carrier transfer between different energy band states may be revealed from EL investigations.

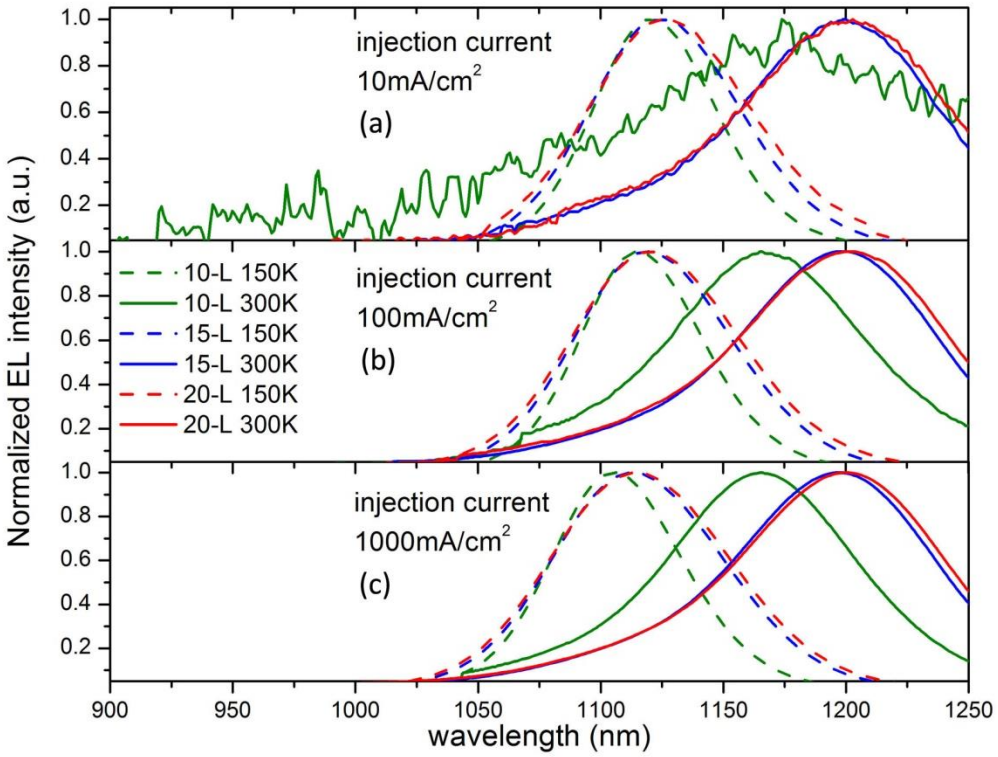

Figure 3.22: Normalized EL spectra of three QDSC samples measured at 150 and 300 K under the injection current density of (a) 10 mA/cm^2, (b) 100 mA/cm^2, (c) 1000 mA/cm^2.

The EL measurements of these three samples were performed under three injection current densities over a wide temperature range, and the data obtained at 150 and 300 K are normalized and plotted in Figure 3.22. The current densities of 10 mA/cm^2, 100 mA/cm^2 and 1000 mA/cm^2 roughly represent the standard QDSC photocurrent levels working under 1, 10 and 100 suns conditions, which is based on the linear estimation of J_{SC} under 1 sun illumination. Similar to PL spectra, these samples exhibit emissions from the QDs and WL, the intensity of the latter is relatively low when the temperature is above ~100 K. It is noted that in Figure 3.22 (a) the QD emission of the 10-layer standard cell at 300 K is weaker than the other conditions, this can be attributed to the thermal leakage of the carriers thus less amount of radiative recombination occurs, because the thermionic emission at high temperature is significant which facilitates the carrier escape from the quantum confinement.

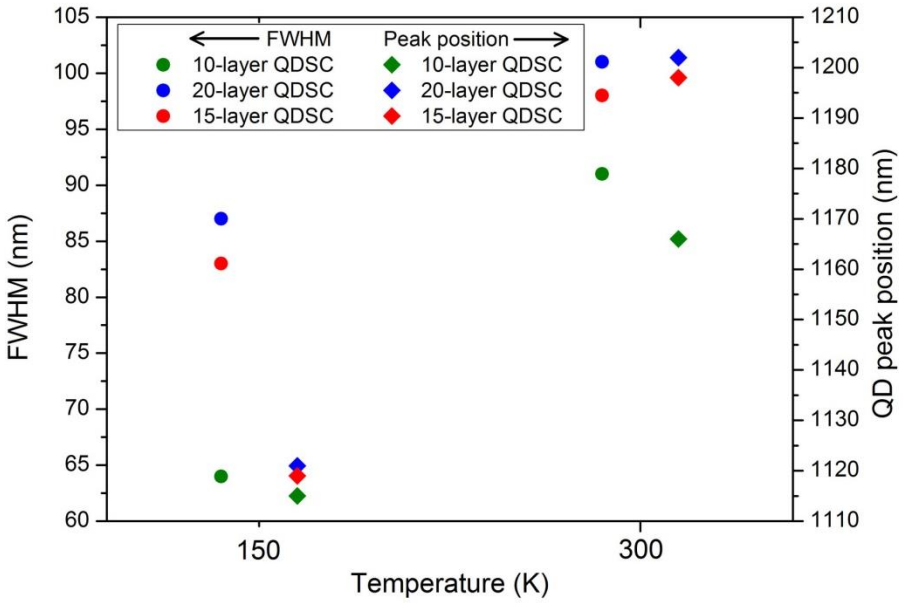

Figure 3.23: The FWHM (left axis) and QD peak positions (right axis) of the samples with different numbers of QD layers at an injection current density of 100 mA/cm^2.

Consistent with peak shift in the PL spectra, the QD EL peak is also red-shifted for devices with 15 and 20 QD layers compared to 10-layer sample. Their QD peak positions under the injection current level of 100 mA/cm^2 are compared in Figure 3.23 (right axis), in which the QD peak was shifted toward lower energies. This is caused by the larger QD sizes in the latter two samples that have deeper confined states thus lower ground states energy. Also, the corresponding full width at half maximum (FWHM) of three devices are extracted from EL curves as shown in Figure 3.23 (left axis). The FWHM becomes bigger when more QD layers were grown, indicating that the size distribution of QDs is larger as a result of higher stacking number.

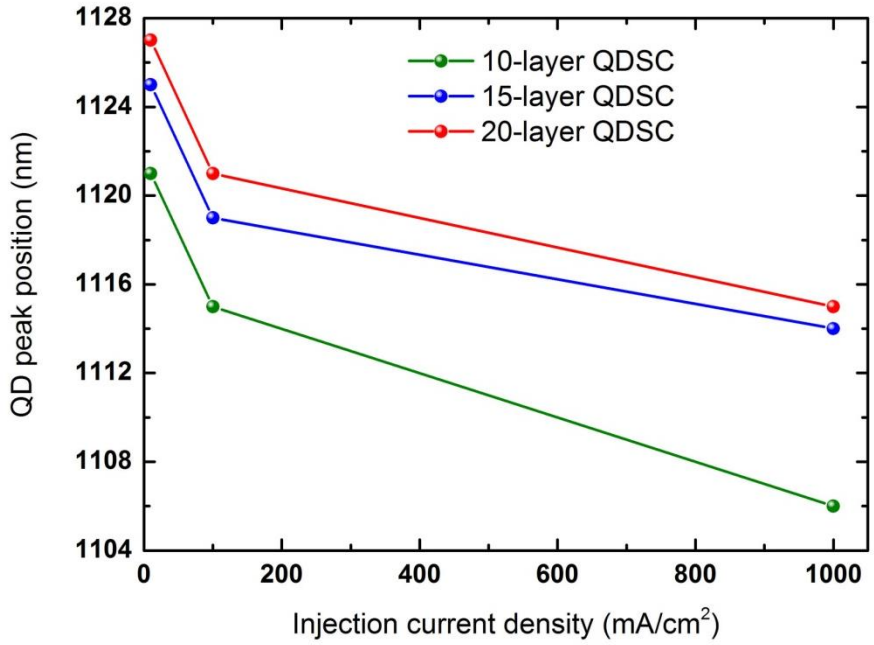

Figure 3.24: The influence of injection current density on the QD emission peak position.

In addition to the features discussed above, these QDSCs present different EL behaviours when the injection current level is changed. The QD emission peaks along with increasing injection current at 150 K are shown in Figure 3.24. It can be observed for all three devices the QD peak position is shifted to higher energies at higher injected current. This is the result of the progressive filling of QD states, which means the injected carriers fill the states of larger QDs first and then occupy the confined states of smaller dots which have higher ground state energy. The progressive filling of carriers also happens when QDSCs are illuminated under the light with different intensities. This phenomenon implies that the larger size distribution of QDs will result in the carriers filling non-uniformity.

3.9 Conclusions

The growth of InGaAs/GaAs quantum dots by MOCVD has been optimized to obtain defect-free solar cell structure. The material and device properties of QDSC structures have been studied, and the 10-layer QD device showed improved photocurrent in comparison to a GaAs control cell. However, the overall efficiency was not improved due to the reduction of open-circuit voltage. The fundamental mechanism for this observation was explored by the investigation of temperature dependent I-V measurements. Especially, we have performed a comparative study on the temperature dependent dark

current properties of GaAs p-i-n reference and InGaAs/GaAs QD solar cells. The QD devices exhibit much more complicated dark I-V behaviour due to the temperature and bias dependent carrier capture, occupation and recombination via QD bound states.

Two-photon absorption has also been investigated for 10-layer QDSC. There is a clear trend that inter-subband photocurrent declines with increasing temperature and cannot be observed at temperatures greater than 70 K. Because at higher temperatures the thermal energy is stronger and thermal transition becomes the dominant excitation path compared to optical excitation (2^{nd} photon excitation).

In addition, QDSCs with different number of QD layers were grown and analyzed. With the increasing number of layers, light absorption in the QD structures is increased however with degraded photocurrent and efficiency, because of non-radiative recombination and poor carrier extraction. EL emission of the solar cell devices under various injection densities was also studied showing that progressive filling of QD states, where the injected carriers fill the states of larger QDs first and then occupy the confined states of smaller dots which have higher ground state energy. This phenomenon implies that the larger size distribution of QDs will result in the non-uniform filling of carriers.

The results obtained in the chapter indicates that further careful design and growth of QDSC is necessary to maximize light absorption while maintaining good carrier extraction and minimization of defect related recombination. It is necessary to provide more carriers occupied in the QD/WL states to improve the photo-generated carrier collection efficiency. A possible effective approach is n-type modulation doping applied within QD layers. The investigation of modulation doping effects on QDSCs will be discussed in Chapter 4.

References

[1] da Silva, M.J., A.A. Quivy, P.P. Gonzalez-Borrero, N.T. Moshegov, and E. Marega, Correlation between structural and optical properties of InAs quantum dots along their evolution. *Journal of Crystal Growth*, 2001. **227**: pp. 1025-1028.

[2] Leon, R. and S. Fafard, Structural and radiative evolution in quantum dots near the InxGa1-xAs/GaAs Stranski-Krastanow transformation. *Physical Review B*, 1998. **58**(4): pp. R1726-R1729.

[3] Sugaya, T., S. Furue, H. Komaki, T. Amano, M. Mori, K. Komori, S. Niki, O. Numakami, and Y. Okano, Highly stacked and well-aligned $In_{0.4}Ga_{0.6}As$ quantum dot solar cells with $In_{0.2}Ga_{0.8}As$ cap layer. *Applied Physics Letters*, 2010. **97**(18): pp. 183104.

[4] Heyn, C. and C. Dumat, Formation and size evolution of self-assembled quantum dots. *Journal of Crystal Growth*, 2001. **227**: pp. 990-994.

[5] Heinrichsdorff, F., A. Krost, M. Grundmann, D. Bimberg, F. Bertram, J. Christen, A. Kosogov, and P. Werner, Self organization phenomena of InGaAs/GaAs quantum dots grown by metalorganic chemical vapour deposition. *Journal of Crystal Growth*, 1997. **170**(1-4): pp. 568-573.

[6] Lever, P., Interdiffusion and Metalorganic Vapour Phase Epitaxial Growth of Self-Assembled InGaAs Quantum Dot Structures and Devices. 2004, Australian National University: Canberra, Australia. pp. 42-51.

[7] Stringfellow, G.B., Organometallic Vapor-Phase Epitaxy: Theory and Practice. 2012: Elsevier Science.

[8] Lever, P., Interdiffusion and Metalorganic Vapour Phase Epitaxial Growth of Self-Assembled InGaAs Quantum Dot Structures and Devices. 2004, Australian National University: Canberra, Australia. pp. 49.

[9] Hubbard, S.M., C. Plourde, Z. Bittner, C.G. Bailey, M. Harris, T. Bald, M. Bennett, D.V. Forbes, and R. Raffaelle. InAs quantum dot enhancement of GaAs solar cells. in *Conference Record of the 35th Ieee Photovoltaic Specialists Conference*. 2010. New York: IEEE.

[10] Takata, A., R. Oshima, Y. Shoji, K. Akahane, and Y. Okada. Fabrication of 100 layer-stacked InAs/GaNAs strain-compensated quantum dots on GaAs (001) for application to intermediate band solar cell. in *Photovoltaic Specialists Conference (PVSC), 2010 35th IEEE*. 2010.

[11] Wasilewski, Z.R., S. Fafard, and J.P. McCaffrey, Size and shape engineering of vertically stacked self-assembled quantum dots. *Journal of Crystal Growth*, 1999. **201–202**: pp. 1131-1135.

[12] Okada, Y., N.J. Ekins-Daukes, T. Kita, R. Tamaki, M. Yoshida, A. Pusch, O. Hess, C.C. Phillips, D.J. Farrell, K. Yoshida, N. Ahsan, Y. Shoji, T. Sogabe, and J.F. Guillemoles, Intermediate band solar cells: Recent progress and future directions. *Applied Physics Reviews*, 2015. **2**(2): pp. 021302.

[13] Fu, L., I. McKerracher, H.H. Tan, C. Jagadish, N. Vukmirovic, and P. Harrison, Effect of GaP strain compensation layers on rapid thermally annealed InGaAs/GaAs quantum dot infrared photodetectors grown by metal-organic chemical-vapor deposition. *Applied Physics Letters*, 2007. **91**(7): pp. 073515.

[14] Martí A., N. López, E. Antolín, E. Cánovas, A. Luque, C.R. Stanley, C.D. Farmer, and P. Díaz, Emitter degradation in quantum dot intermediate band solar cells. *Applied Physics Letters*, 2007. **90**(23): pp. 233510.

[15] Jolley, G., H.F. Lu, L. Fu, H.H. Tan, and C. Jagadish, Electron-hole recombination properties of In0.5Ga0.5As/GaAs quantum dot solar cells and the influence on the open circuit voltage. *Applied Physics Letters*, 2010. **97**(12): pp. 123505.

[16] Lu, H.F., L. Fu, J. Greg, T. Hark Hoe, T. Sudersena Rao, and J. Chennupati, Temperature dependence of dark current properties of InGaAs/GaAs quantum dot solar cells. *Applied Physics Letters*, 2011. **98**(18): pp. 183509.

[17] Lever, P., Interdiffusion and Metalorganic Vapour Phase Epitaxial Growth of Self-Assembled InGaAs Quantum Dot Structures and Devices. 2004, Australian National University: Canberra, Australia. pp. 24.

[18] Gupta, J.A., S.P. Watkins, E.D. Crozier, J.C. Woicik, D.A. Harrison, D.T. Jiang, I.J. Pickering, and B.A. Karlin, Layer perfection in ultrathin InAs quantum wells in GaAs(001). *Physical Review B*, 2000. **61**(3): pp. 2073-2084.

[19] Yu, P.R., K. Zhu, A.G. Norman, S. Ferrere, A.J. Frank, and A.J. Nozik, Nanocrystalline TiO_2 solar cells sensitized with InAs quantum dots. *Journal of Physical Chemistry B*, 2006. **110**(50): pp. 25451-25454.

[20] Sears, K., Growth and Characterisation of Self-Assembled InAs/GaAs Quantum Dots and Optoelectronic Devices. 2006, Australian National University: Canberra, Australia. pp. 95-96.

[21] Rai, R. and C. Parsons, Characterizing III–V heteroepitaxial structures. *JOM Journal of the Minerals Metals and Materials Society*, 1994. **46**(9): pp. 50-54.

[22] Hubbard, S.M., C.D. Cress, C.G. Bailey, R.P. Raffaelle, S.G. Bailey, and D.M. Wilt, Effect of strain compensation on quantum dot enhanced GaAs solar cells. *Applied Physics Letters*, 2008. **92**(12): pp. 123512.

[23] Popescu, V., G. Bester, M.C. Hanna, A.G. Norman, and A. Zunger, Theoretical and experimental examination of the intermediate-band concept for strain-balanced (In,Ga)As/Ga(As,P) quantum dot solar cells. *Physical Review B*, 2008. **78**(20): pp. 17.

[24] Okada, Y., R. Oshima, and A. Takata, Characteristics of InAs/GaNAs strain-compensated quantum dot solar cell. *Journal of Applied Physics*, 2009. **106**(2): pp. 024306.

[25] Ekins-Daukes, N.J., K.W.J. Barnham, J.P. Connolly, J.S. Roberts, J.C. Clark, G. Hill, and M. Mazzer, Strain-balanced GaAsP/InGaAs quantum well solar cells. *Applied Physics Letters*, 1999. **75**(26): pp. 4195-4197.

[26] Aperathitis, E., C.G. Scott, D. Sands, V. Foukaraki, Z. Hatzopoulos, and P. Panayotatos, Effect of temperature on GaAs/AlGaAs multiple quantum well solar cells. *Materials Science and Engineering B-Solid State Materials for Advanced Technology*, 1998. **51**(1-3): pp. 85-89.

[27] Radziemska, E., Effect of temperature on dark current characteristics of silicon solar cells and diodes. *International Journal of Energy Research*, 2006. **30**(2): pp. 127-134.

[28] Kachare, R., B.E. Anspaugh, and G.F.J. Garlick, Tunneling effects in the current-voltage characteristics of high-efficiency GaAs solar cells. *Solid-State Electronics*, 1988. **31**(2): pp. 159-166.

[29] Ryzhii, V., I. Khmyrova, V. Pipa, V. Mitin, and M. Willander, Device model for quantum dot infrared photodetectors and their dark-current characteristics. *Semiconductor Science and Technology*, 2001. **16**(5): pp. 331-338.

[30] Schroder, D.K., Semiconductor Material and Device Characterization, 3rd ed., in Semiconductor Material and Device Characterization, 3rd ed. 2006, Wiley: New Jersey.

[31] Kavasoglu, N., A.S. Kavasoglu, and S. Oktik, A new method of diode ideality factor extraction from dark I-V curve. *Current Applied Physics*, 2009. **9**(4): pp. 833-838.

[32] Gu, T.Y., M.A. El-Emawy, K. Yang, A. Stintz, and L.F. Lester, Resistance to edge recombination in GaAs-based dots-in-a-well solar cells. *Applied Physics Letters*, 2009. **95**(26): pp. 261106.

[33] Luque, A. and A. Marti, Increasing the efficiency of ideal solar cells by photon induced transitions at intermediate levels. *Physical Review Letters*, 1997. **78**(26): pp. 5014-5017.

[34] Ley, M., J. Boudaden, and Z.T. Kuznicki, Thermodynamic efficiency of an intermediate band photovoltaic cell with low threshold Auger generation. *Journal of Applied Physics*, 2005. **98**(4): pp. 044905.

[35] Shockley, W. and H.J. Queisser, Detailed Balance Limit of Efficiency of P-N Junction Solar Cells. *Journal of Applied Physics*, 1961. **32**(3): pp. 510-519.

[36] Araújo, G.L. and A. Martí, Absolute limiting efficiencies for photovoltaic energy conversion. *Solar Energy Materials and Solar Cells*, 1994. **33**(2): pp. 213-240.

[37] Marti, A., L. Cuadra, and A. Luque. Quantum dot intermediate band solar cell. in *28th IEEE Photovoltaic Specialists Conference*. 2000. Anchorage.

[38] Aroutiounian, V., S. Petrosyan, A. Khachatryan, and K. Touryan, Quantum dot solar cells. *Journal of Applied Physics*, 2001. **89**(4): pp. 2268-2271.

[39] Laghumavarapu, R.B., M. El-Emawy, N. Nuntawong, A. Moscho, L.F. Lester, and D.L. Huffaker, Improved device performance of InAs/GaAs quantum dot solar cells with GaP strain compensation layers. *Applied Physics Letters*, 2007. **91**(24): pp. 243115.

[40] Guimard, D., R. Morihara, D. Bordel, K. Tanabe, Y. Wakayama, M. Nishioka, and Y. Arakawa, Fabrication of InAs/GaAs quantum dot solar cells with enhanced photocurrent and without degradation of open circuit voltage. *Applied Physics Letters*, 2010. **96**(20): pp. 203507.

[41] Levy, M.Y. and C. Honsberg, Intraband absorption in solar cells with an intermediate band. *Journal of Applied Physics*, 2008. **104**(11): pp. 113103.

[42] Luque, A. and A. Marti, The Intermediate Band Solar Cell: Progress Toward the Realization of an Attractive Concept. *Advanced Materials*, 2010. **22**(2): pp. 160-174.

[43] Marti, A., E. Antolin, C.R. Stanley, C.D. Farmer, N. Lopez, P. Diaz, E. Canovas, P.G. Linares, and A. Luque, Production of Photocurrent due to Intermediate-to-Conduction-Band Transitions: A Demonstration of a Key Operating Principle of the Intermediate-Band Solar Cell. *Physical Review Letters*, 2006. **97**(24): pp. 247701.

[44] Okada, Y., T. Morioka, K. Yoshida, R. Oshima, Y. Shoji, T. Inoue, and T. Kita, Increase in photocurrent by optical transitions via intermediate quantum states in direct-doped InAs/GaNAs strain-compensated quantum dot solar cell. *Journal of Applied Physics*, 2011. **109**(2): pp. 024301.

[45] Jolley, G., L. Fu, H.F. Lu, H.H. Tan, and C. Jagadish, The role of intersubband optical transitions on the electrical properties of InGaAs/GaAs quantum dot solar cells. *Progress in Photovoltaics: Research and Applications*, 2013. **21**(4): pp. 736-746.

[46] Jolley, G., H.F. Lu, L. Fu, H.H. Tan, and C. Jagadish, Electron-hole recombination properties of $In_{0.5}Ga_{0.5}As$/GaAs quantum dot solar cells and the influence on the open circuit voltage. *Applied Physics Letters*, 2010. **97**(12): pp. 123505.

[47] Antolin, E., A. Marti, C.D. Farmer, P.G. Linares, E. Hernandez, A.M. Sanchez, T. Ben, S.I. Molina, C.R. Stanley, and A. Luque, Reducing carrier escape in the

InAs/GaAs quantum dot intermediate band solar cell. *Journal of Applied Physics*, 2010. **108**(6): pp. 064513.

[48] Ramey, S.M. and R. Khoie, Modeling of multiple-quantum-well solar cells including capture, escape, and recombination of photoexcited carriers in quantum wells. *Ieee Transactions on Electron Devices*, 2003. **50**(5): pp. 1179-1188.

[49] Tsai, C.Y. and C.Y. Tsai, Effects of Carrier Escape and Capture Processes on Quantum Well Solar Cells. *Nusod '08: Proceedings of the 8th International Conference on Numerical Simulation of Optoelectronic Devices*, 2008: pp. 79-80

Chapter 4

Investigation of modulation doping in quantum dot solar cells

4.1 Introduction

It has been discussed that the incorporation of quantum dots into single junction p-i-n solar cell can produce below bandgap light absorption and generate extra photocurrent and consequently improves the short circuit current density [1-4]. QDSCs are considered as a promising candidate for the implementation of the intermediate band solar cell (IBSC) concept, which is based on sub-bandgap multi-photon absorption processes [5, 6]. However, as shown in the previous chapter, in QDSC structures considerable amount of recombination can take place in the WL and QDs confined states and thus making transport and collection of photo-generated carriers inefficient [2, 7-10]. Indeed, based on the original theoretical work on IBSC in ref [11], it is desirable to partially (half) fill the IB states with electrons so that enough electrons can be further promoted to the CB to form photocurrent. Also, in some types of semiconductor devices (including solar cells, infrared photodetectors, and lasers) QW/QD layers are doped to provide sufficient carriers for effective inter-subband transition [11-14]. Therefore, to provide sufficient carriers to occupy the QD states irrespective of large simultaneous recombination events and thus improve the carrier extraction efficiency to maximize photocurrent, doping of the QDs has been considered as a useful approach. For QDSCs, this can be achieved by introducing n-type doping in the QD growth process at a certain concentration that is approximately similar to the quantum dot density.

There are two ways to insert the dopants into QD structure. First is the direct doping where the dopants are added directly into QDs during growth. But it has been reported that defects could be formed due to direct doping which will affect optical and electrical properties of QDs [15, 16]. The second method is modulation doping where the dopants are inserted into the barrier layer prior to QD growth [17]. In this case the crystal quality of the QDs will not be affected by doping process. In this thesis, modulation doping between the QD layers is used to partially fill the sub-bandgap states with electrons by n-type doping, which can be lifted to the conduction band edge of the host GaAs materials [3, 11]. Modulation doping which is embedded into intrinsic spacer layers for various QDs systems has been investigated [13, 18, 19].

However, the effect of modulation doping placed within a thin spacer layer on the quantum dot solar cell performance and its position dependence have not been reported yet.

In this chapter, we study the influence of silicon modulation (n-type) doping on the properties and performance of 10-layer $In_{0.5}Ga_{0.5}As$/GaAs QDSC. Doping effects at two different positions were also compared and investigated.

4.2 MOCVD growth of modulation doped quantum dot solar cells

The InGaAs/GaAs QDSCs used in this study were grown on heavily n-type doped GaAs (001) substrate by metal organic chemical vapour deposition. Similar to our standard QDSC structures, the modulation doped samples all consists of n^+-doped buffer, n^--doped GaAs base layer, ten layers of 6 monolayer $In_{0.5}Ga_{0.5}As$ QDs separated by 50 nm of intrinsic GaAs barriers followed by a p^--$Al_{0.45}Ga_{0.55}As$ window layer and terminated with p^+-doped GaAs contact layer. In addition, Si dopants were incorporated within a 4 nm-thick GaAs barrier layer that is placed a certain distance away from the QD layer, with dopant sheet densities of ~ 9×10^{10}, ~ 1.8×10^{11} cm^{-2} to provide average ~ 2 and ~ 4 electrons per quantum dot. Two doping positions were investigated, (A) the 4 nm doping layer was placed 10 nm below each QD/WL layer, whereas position (B) was just 10 nm above each QD/WL layer. The doping details for the modulation doped QDSC samples are shown schematically in Figure 4.1. All samples were then fabricated into 3×3 mm^2 devices with the same procedure as described in Chapter 2. Standard solar cell characteristics were tested using an Oriel solar simulator and external quantum efficiency (EQE) measurements were carried out using an Oriel IQE-200 system.

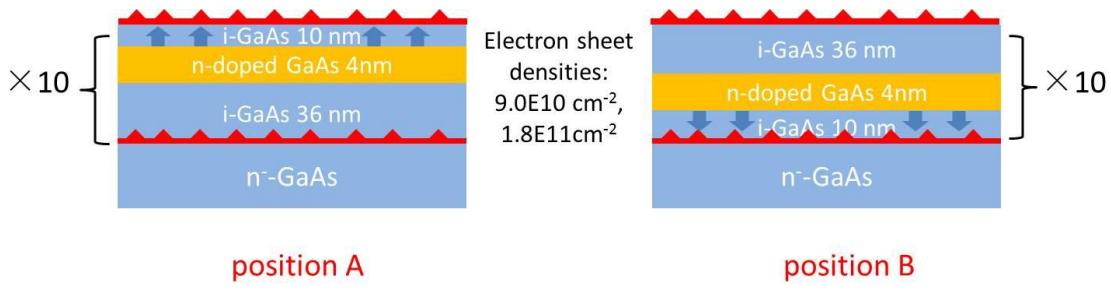

Figure 4.1: Schematic diagrams of the active region of the two n-type modulation doped QDSC structures in which the doping was placed at two different positions: (A)

the doping layer is 10 nm below QD/WL, and (B) it is 10 nm above QD/WL. Arrows indicate the electrons doping towards QD/WL.

4.3 Results and discussion

Due to different strain and surface energy, the WL- intrinsic GaAs layer interface and the QD- intrinsic GaAs layer interface are quite different. This may have different effects on the electrons filling process from the thin modulation doped GaAs layer to WL and QDs. Various optical and electrical investigations were carried out to study the electrons filling behaviours which will affect below bandgap transition and carrier transport of QDSCs.

The photoluminescence of the undoped and modulation doped QDSC samples with average doping density of 2e/dot and 4e/dot were measured at room temperature and plotted in Figure 4.2. In this Figure, only the samples with doping at position A are shown, as very similar results are observed for the samples doped at position B. Compared to the sample with no intentional doping in the QD region, modulation doped structures exhibit stronger emission from both the quantum dot and wetting layers. The intensity becomes larger with higher Si doping concentration. Because all three samples were excited by the same laser (532 nm) intensity, stronger light emission indicates a larger amount of radiative recombination. As described above, the introduction of n-type modulation doping will partially fill the quantum dot and wetting layer states by electrons, which will result in a higher concentration of electrons in QDs region when the sample is under laser excitation during PL measurements. It is likely that the extra electrons provided via modulation doping will compensate to some extent the thermal carrier leakage at room temperature during the photo excitation process leading to increased PL intensity. Besides, the results indicate that defects such as electron traps at the heterointerface may be saturated by the additional electrons and hence reduced nonradiative recombination from QDs CB to VB. This phenomenon was also observed in the direct Si-doped InAs/GaNAs strain-compensated QDSCs by Okada *et al.* [20].

For our solar cells the Si dopants were incorporated into the GaAs barrier 10 nm below the WL/QDs layer, so the size, composition, and crystal quality of QDs should not be affected. High luminescence efficiency reflects good material quality as well as photovoltaic quantum efficiency to some extent according to certain reciprocity relationship between them as described in the ref [21]. The results obtained in Figure 4.2 also imply good solar cell performance may also be obtained in our modulation doped QDSC samples.

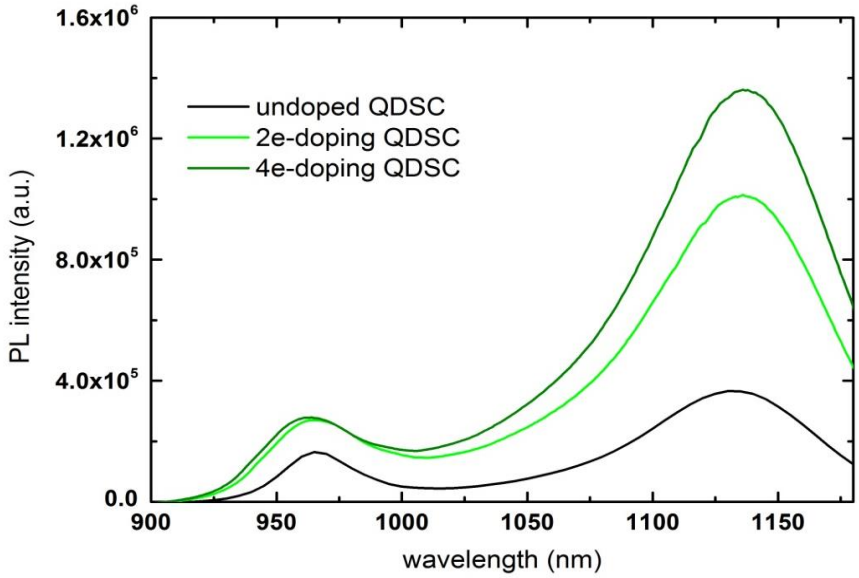

Figure 4.2: Room temperature photoluminescence spectra of undoped QD solar cell, 2e and 4e modulation doped samples, where the doping was in position A.

The I-V characteristics of undoped and doped QDSCs tested under 1 Sun AM1.5G condition are plotted in Figure 4.3, which shows that the modulation doped devices exhibit a substantial increase of J_{sc} with well maintained and a slight increase in V_{oc} compared to the undoped control cell, except for the 2e/dot doped sample at position B, which shows similar photocurrent and voltage as those of control cell. These enhancements result in improved overall conversion efficiencies, with larger improvement obtained from samples doped at position A. The detailed solar cell parameters of these five samples are also summarized in Table 4.1. By comparing the effects induced by modulation doping at the two different positions, the Si doped thin layer closer to wetting layer side (position A) generally results in better performance of solar cells than the doping position closer to quantum dots side (position B). The 4e/dot doped device at position A shows the highest improvement. The improved J_{sc} and V_{oc} result in an enhanced conversion efficiency of 8.91 % from 6.95 % of the undoped sample, i.e., an increase of 28.20 %.

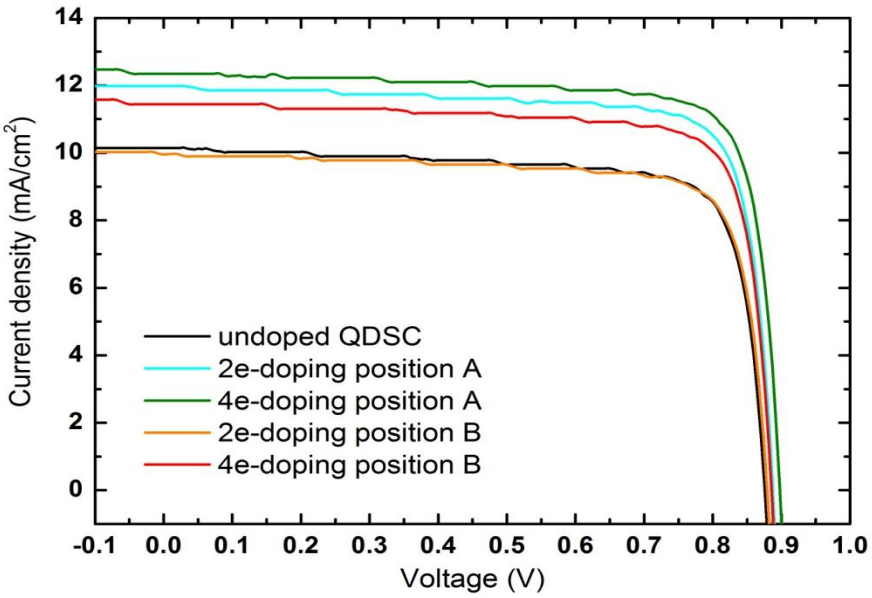

Figure 4.3: I-V characteristics of undoped and the other four modulation-doped QDSCs under 1-sun irradiation.

The slight increase of V_{oc} is most likely due to additional electrons effectively induced by modulation doping filling more the WL/QDs states that leads to higher electron quasi-Fermi level. Improved carrier escape after QD states filling also helps to increase the forward injection thermal activation energy (E_a) and hence recovery of V_{oc} achieved (Section 3.6.3). This may slightly eliminate the general V_{oc} degradation induced by quantum structures [1].

Table 4.1: The comparison of solar cell parameters of the four modulation doped QD solar cells and the undoped reference cell. The increase percentage of the best device is shown in bracket.

Samples	V_{oc} (V)	J_{sc} (mA/cm^2)	FF (%)	Efficiency (%)
Std QDSC	0.875	10.118	78.409	6.946
2e position B	0.879	10.070	79.133	7.006
4e position B	0.885	11.467	79.753	8.098
2e position A	0.887	11.944	79.867	8.463
4e position A	0.897(2.51%)	12.366(22.22%)	80.239(2.33%)	8.905(28.20%)

To further understand the effects of modulation doping, external quantum efficiency (EQE) measurements were also performed. Figure 4.4 plots the EQE of the undoped and doped cells at position A in the wavelength range from 700 - 1185 nm. Also shown on the right axis is the room temperature PL from the same samples indicating the peak positions of the WL and QDs for comparison.

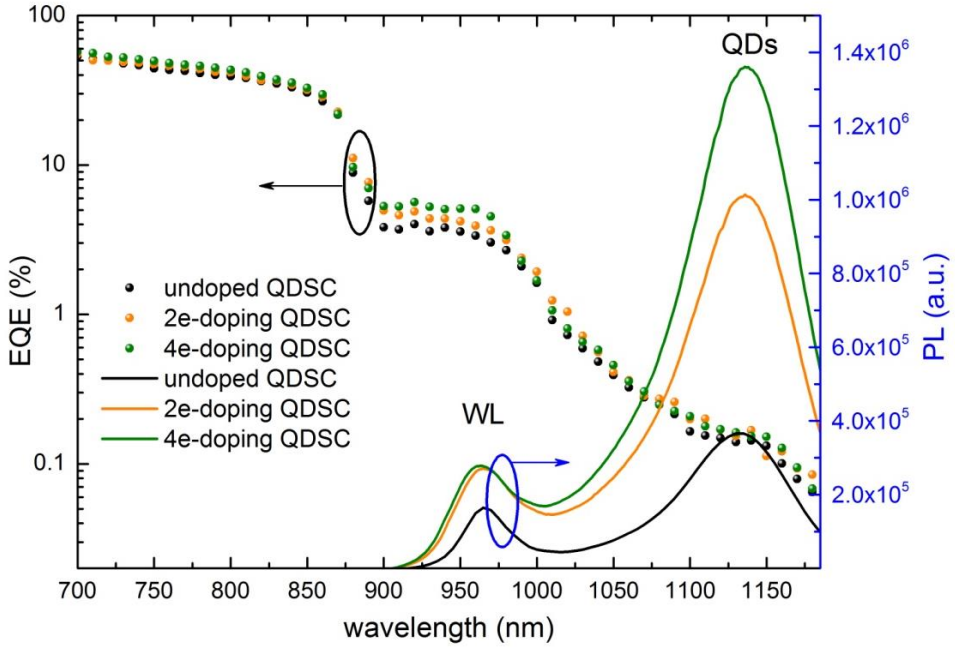

Figure 4.4: EQE of undoped and position A doped QDSCs (left axis), and the corresponding room temperature PL curves of the same samples (right axis).

For all the samples, the band-to-band absorption of GaAs is observed below 875 nm from the EQE curves. The peaks spanning the spectral range from 875 to 1000 nm correspond to the photocurrent originated from the wetting layer absorption, the wavelength region above 1000 nm is mainly related to that from QD absorption. The EQE of the two doped samples display enhancement compared to that of the undoped device, particularly in the WL region. The 4e-doped device exhibits the largest quantum efficiency enhancement, which is in good agreement with I-V results plotted in Figure 4.3. The enhancement is achieved by the introduction of additional electrons via Si n-type doping between the QD layers resulting in more carriers being photo-excited from the confined WL/QD states to the GaAs spacer layer conduction band [3, 13, 18]. Even though the most obvious quantum efficiency enhancement appears in the WL region, we can still observe a slight increase over a longer wavelength QD region. It should also be noticed that even in the GaAs region, improved quantum efficiency is obtained, meaning that the n-type modulation doping not only improves the electrons extraction in wetting layer and quantum dots, but also makes the carrier transport through the whole p-i-n junction more efficient [22]. Also, when the quantum dot states are partially filled by electrons, they will electrically weaken the trapping potential and produce a repulsive force on the surrounding mobile electrons [2, 23]. Therefore negatively charged quantum dots act as repulsive centres in the planar direction on these electrons that are

transported through the QDs layers. This Coulomb force correlates with QDs modulation doping and competes with the trapping process [24]. As more QD states are filled with doped electrons, the capture probability of carriers passing through the QD/WL layers is reduced and thus the GaAs photocurrent peak recovers.

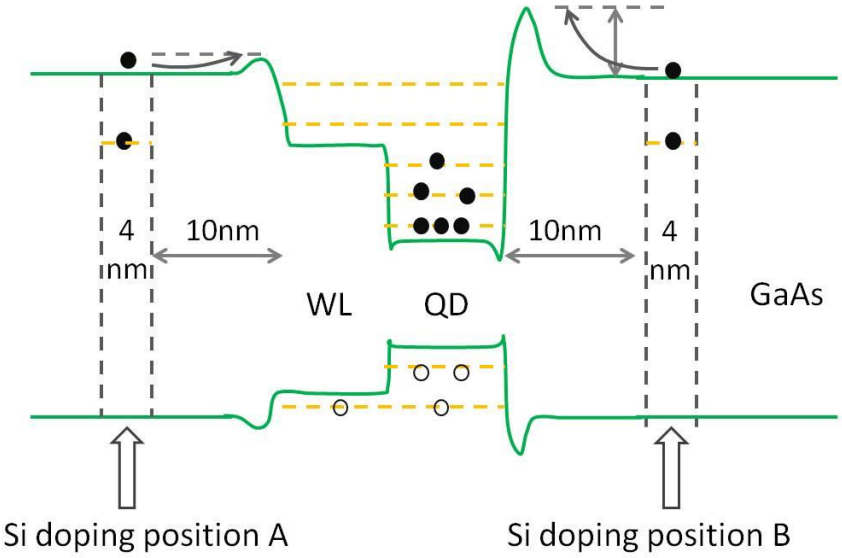

Figure 4.5: The schematic of energy band structure and electrons diffusion process, where the modulation doping is placed in two positions.

In order to explain the different behaviours of QDSCs with different doping positions, the schematic of energy band diagrams of the two modulation doped samples with doping position A and B are illustrated in Figure 4.5. In QD systems, because strain can significantly alter the semiconductor bandgap and due to the high compressive strain of QDs, its effect on the confinement potential must be taken into consideration [2, 25]. As schematically shown in Figure 4.5, based on the theoretical simulation on In(Ga)As quantum dots, with the consideration of position dependent hydrostatic strain and conduction band deformation potential, the effective potential for QDs always exhibit an increased potential at the conduction band edge [26]. For the case of modulation doping, free carriers (electrons in this case) that are created by the modulation doping in the GaAs barrier layer will need to diffuse and/or drift towards the QD region to be captured by the QD potential. In the picture, for WL/GaAs interface, the potential barrier is relatively low and will allow easy electron filling from the Si doping layer to the wetting layer and quantum dot states at room temperature, leading to efficient modulation doping with expected doping density in WL/QDs. On the

other hand, at the QD/GaAs interface, much larger potential barrier exists which will largely suppresses the modulation doping effect and thus reduced the effective electron doping density. This leads to a much less obvious improvement in photocurrent for the modulation doping achieved by doping at position B.

4.4 Conclusions

In this chapter, we have investigated the influence of n-type modulation doping on InGaAs/GaAs QDSC performance. Two doping positions and concentration levels were investigated and compared. The 4e/dot doped device at position A shows the highest improvement. Up to 28.20 % efficiency enhancement from 6.95 % to 8.91 % was achieved in modulation doped cell with respect to the undoped QDSC device, due to improved carrier transport and extraction efficiency. When the quantum dot states are partially filled by electrons, they will electrically weaken the trapping potential and produce a repulsive force on the surrounding mobile electrons.

It was also revealed that the position of modulation doping is critical to achieve effective doping in the QD structures for improved efficiency. First, due to different strain and surface energy, the WL- intrinsic GaAs layer interface and the QD- intrinsic GaAs layer interface are quite different. This may have different effects on the electrons filling process from the thin modulation doped GaAs layer to WL and QDs. On the other hand, at the QD/GaAs interface, much larger potential barrier exists which will largely suppresses the modulation doping effect and thus reduced the effective electron doping density. The results are important for future design of QDSC structures to achieve higher conversion efficiency.

References

[1] Jolley, G., H.F. Lu, L. Fu, H.H. Tan, and C. Jagadish, Electron-hole recombination properties of $In_{0.5}Ga_{0.5}As$/GaAs quantum dot solar cells and the influence on the open circuit voltage. *Applied Physics Letters*, 2010. **97**(12): pp. 123505.

[2] Lu, H.F., L. Fu, J. Greg, T. Hark Hoe, T. Sudersena Rao, and J. Chennupati, Temperature dependence of dark current properties of InGaAs/GaAs quantum dot solar cells. *Applied Physics Letters*, 2011. **98**(18): pp. 183509.

[3] Marti, A., N. Lopez, E. Antolin, E. Canovas, C. Stanley, C. Farmer, L. Cuadra, and A. Luque. Novel semiconductor solar cell structures: The quantum dot intermediate band solar cell. in *Symposium on Thin Film and Nanostructured*

Materials for Photovoltaics held at the 2005 EMRS Meeting. 2005. Strasbourg, FRANCE: Elsevier Science Sa.

[4] Riel, B.J., An introduction to self-assembled quantum dots. *American Journal of Physics*, 2008. **76**(8): pp. 750-757.

[5] Luque, A. and A. Marti, The Intermediate Band Solar Cell: Progress Toward the Realization of an Attractive Concept. *Advanced Materials*, 2010. **22**(2): pp. 160-174.

[6] Okada, Y., N.J. Ekins-Daukes, T. Kita, R. Tamaki, M. Yoshida, A. Pusch, O. Hess, C.C. Phillips, D.J. Farrell, K. Yoshida, N. Ahsan, Y. Shoji, T. Sogabe, and J.F. Guillemoles, Intermediate band solar cells: Recent progress and future directions. *Applied Physics Reviews*, 2015. **2**(2): pp. 021302.

[7] Marcinkevicius, S. and R. Leon, Carrier capture and relaxation in quantum dot structures with different dot densities. *Microelectronic Engineering*, 2000. **51-2**: pp. 79-83.

[8] Brasken, M., M. Lindberg, M. Sopanen, H. Lipsanen, and J. Tulkki, Temperature dependence of carrier relaxation in strain-induced quantum dots. *Physical Review B*, 1998. **58**(24): pp. 15993-15996.

[9] Adler, F., M. Geiger, A. Bauknecht, F. Scholz, H. Schweizer, M.H. Pilkuhn, B. Ohnesorge, and A. Forchel, Optical transitions and carrier relaxation in self assembled InAs/GaAs quantum dots. *Journal of Applied Physics*, 1996. **80**(7): pp. 4019-4026.

[10] Ohnesorge, B., M. Albrecht, J. Oshinowo, A. Forchel, and Y. Arakawa, Rapid carrier relaxation in self-assembled InxGa1-xAs/GaAs quantum dots. *Physical Review B*, 1996. **54**(16): pp. 11532-11538.

[11] Marti, A., L. Cuadra, and A. Luque, Partial filling of a quantum dot intermediate band for solar cells. *Electron Devices, IEEE Transactions on*, 2001. **48**(10): pp. 2394-2399.

[12] Li, G., M.B. Johnston, A. Babinski, S. Yuan, M. Gal, S.J. Chua, and C. Jagadish, Si and C δ-doping for device applications. *Journal of Crystal Growth*, 1998. **195**(1–4): pp. 54-57.

[13] Sablon, K.A., J.W. Little, V. Mitin, A. Sergeev, N. Vagidov, and K. Reinhardt, Strong Enhancement of Solar Cell Efficiency Due to Quantum Dots with Built-In Charge. *Nano Letters*, 2011. **11**(6): pp. 2311-2317.

[14] Zhang, Z.Y., Q. Jiang, and R.A. Hogg, Tunable interband and intersubband transitions in modulation C-doped InGaAs/GaAs quantum dot lasers by postgrowth annealing process. *Applied Physics Letters*, 2008. **93**(7): pp. 071111.

[15] Kim, J.S., P.W. Yu, J.-Y. Leem, J.I. Lee, S.K. Noh, J.S. Kim, G.H. Kim, S.-K. Kang, S.I. Ban, S.G. Kim, Y.D. Jang, U.H. Lee, J.S. Yim, and D. Lee, Growth of Si-doped InAs quantum dots and annealing effects on size distribution. *Journal of Crystal Growth*, 2002. **234**(1): pp. 105-109.

[16] Phillips, J., K. Kamath, X. Zhou, N. Chervela, and P. Bhattacharya, Photoluminescence and far-infrared absorption in Si-doped self-organized InAs quantum dots. *Applied Physics Letters*, 1997. **71**(15): pp. 2079-2081.

[17] Dingle, R., H.L. Störmer, A.C. Gossard, and W. Wiegmann, Electron mobilities in modulation-doped semiconductor heterojunction superlattices. *Applied Physics Letters*, 1978. **33**(7): pp. 665-667.

[18] Schneider, C., S. Kremling, N.V. Tarakina, T. Braun, M. Adams, M. Lermer, S. Reitzenstein, L. Worschech, M. Kamp, S. Hofling, and A. Forchel, AlGaInAs quantum dot solar cells: tailoring quantum dots for intermediate band formation. *Semiconductor Science and Technology*, 2012. **27**(3): pp. 032002.

[19] Marcinkevicius, S., J. Siegert, and Q.X. Zhao, Carrier spin dynamics in modulation-doped InAs/GaAs quantum dots. *Journal of Applied Physics*, 2006. **100**(5): pp. 054310.

[20] Okada, Y., T. Morioka, K. Yoshida, R. Oshima, Y. Shoji, T. Inoue, and T. Kita, Increase in photocurrent by optical transitions via intermediate quantum states in direct-doped InAs/GaNAs strain-compensated quantum dot solar cell. *Journal of Applied Physics*, 2011. **109**(2): pp. 024301.

[21] Rau, U., Reciprocity relation between photovoltaic quantum efficiency and electroluminescent emission of solar cells. *Physical Review B*, 2007. **76**(8): pp. 085303.

[22] Jolley, G., L. Fu, H.F. Lu, H.H. Tan, and C. Jagadish, The role of intersubband optical transitions on the electrical properties of InGaAs/GaAs quantum dot solar cells. *Progress in Photovoltaics: Research and Applications*, 2013. **21**(4): pp. 736-746.

[23] Li, T., H. Lu, L. Fu, H.H. Tan, C. Jagadish, and M. Dagenais, Enhanced carrier collection efficiency and reduced quantum state absorption by electron doping in self-assembled quantum dot solar cells. *Applied Physics Letters*, 2015. **106**(5): pp. 053902.

[24] Inoue, T., S. Kido, K. Sasayama, T. Kita, and O. Wada, Impurity doping in self-assembled InAs/GaAs quantum dots by selection of growth steps. *Journal of Applied Physics*, 2010. **108**(6): pp. 063524.

[25] Ryzhii, V., I. Khmyrova, V. Pipa, V. Mitin, and M. Willander, Device model for quantum dot infrared photodetectors and their dark-current characteristics. *Semiconductor Science and Technology*, 2001. **16**(5): pp. 331-338.

[26] Jolley, G., Growth and Analysis of Quantum Dots-in-a-Well Infrared Photodetectors, PhD thesis, Chapter 3, 2009, Australian National University.

Chapter 5

Effects of post-growth thermal annealing on quantum dot solar cells

5.1 Introduction

For the growth of self-assembled quantum dots (QDs) [1-4] and their application towards high performance optoelectronic devices such as QD lasers [5], QD infrared photodetectors (QDIPs) [6, 7] and QD solar cells (QDSC) [8, 9], a major challenge is to modify the size, shape, composition of QDs and thus their optical properties, electronic band structure, and related device properties. Indeed, due to the nature of self-organised process, modification of the QD property requires extensive growth optimization with limited window of tunability. Therefore, post-growth thermal annealing is expected to be an attractive alternative approach to tailor the QDs morphology and consequently energy band structure and carrier confinement [6, 7, 10-12], through promoting of thermal inter-diffusion between QD material and its surrounding barrier material. The experimental and theoretical work on inter-diffusion induced QD band structure change and its effect on device performance such as infrared (IR) lasers and photodetectors have been reported previously [6, 10, 11, 13], showing that the thermal annealing can lead to significant change on QD electronic band structure and thus the laser emission or photodetector detection wavelengths with modified optoelectronic properties. However, to our knowledge so far there is no report on the thermal inter-diffusion effect on QD solar cell performance.

In this chapter, we study the post-growth annealing effects on InGaAs/GaAs QDSCs with various number of QD layers, the original device performances of which have been discussed in Chapter 3. Firstly, the as-grown 10-layer QDSC sample was annealed at a wide temperature range from 700 ℃ to 850 ℃ for 50 s and characterized by photoluminescence (PL) measurements. The annealed QDSC devices were also characterized by temperature dependent dark current, 1 sun illuminated I-V characteristics, and external quantum efficiency (EQE) measurements. The effect of dopant diffusion was also investigated by Secondary Ion Mass Spectrometry (SIMS) measurements. Based on these results, annealing at 850 ℃ for 50 s was chosen for further study of the annealing effect on the QDSC samples with 15,

20 stacking layers. The effects of thermal inter-diffusion on QD size, composition, confinement energy and carrier collection efficiency and thus QDSC performance are investigated and discussed.

5.2 Experimental

The 10, 15 and 20-layer $In_{0.6}Ga_{0.4}As$/ GaAs QDSCs studied in this chapter were grown on n^+-doped GaAs (001) substrate by metal organic chemical vapour deposition, based on the same standard 10 layers p-i-n QDSC design as described in Chapter 3 but with a fine tune of QD growth time (3.5 s) and slightly higher In component. After growth the wafer was cleaved into several pieces. Rapid thermal annealing (RTA) was performed on the 10-layer QDSC samples at temperatures from 700 to 850 ℃ with a step of 50 ℃ for 50 s under Ar flow. The 15- and 20-layer QDSC samples were only annealed at 850 ℃ for 50 s under Ar flow. During annealing process, the surface of the samples were covered with a fresh piece of GaAs wafer to minimize the As desorption from sample surface. After that, all samples were fabricated into 1 x 1 mm^2 mesa devices following the fabrication process described in Chapter 2.

Low temperature photoluminescence (PL) and temperature dependent dark I-V characteristics were carried out in a close-cycled He cryostat. External quantum efficiency (EQE) was tested by an Oriel IQE-200 system. The standard device parameters were measured using an Oriel solar simulator (1-sun, AM 1.5G).

5.3 Study of annealing effects on 10-layer quantum dot solar cells

The as-grown 10-layer $In_{0.6}Ga_{0.4}As$/GaAs QDSC sample was annealed at various temperatures between 700 and 850 ℃ at a step of 50 ℃. The material and device characteristics including photoluminescence, temperature dependent dark current, external quantum efficiency and solar cell parameters at 1-sun condition were investigated and compared for the series of annealing conditions. The possible effects from annealing induced dopants diffusion on device properties will be also verified and discussed.

5.3.1 Low temperature photoluminescence

Photoluminescence is the most commonly used technique to evaluate the effect of thermal inter-diffusion on the bandgap energy of the QD samples after annealing [10, 14]. The PL spectra taken at 77 K on samples which were annealed at temperatures from 700 ℃ to 850 ℃ are shown in Figure 5.1. It indicates clearly that thermal annealing at high temperatures induces significant blue-shift of the wetting layer and QDs PL peak positions. This phenomenon is caused by the compositional inter-diffusion of the InGaAs quantum dot materials with its surrounding GaAs barriers, i.e. In and Ga inter-diffusion, which leads to decreased confinement potentials in both conduction band and valence band for WL and QDs respectively [7, 10, 11].

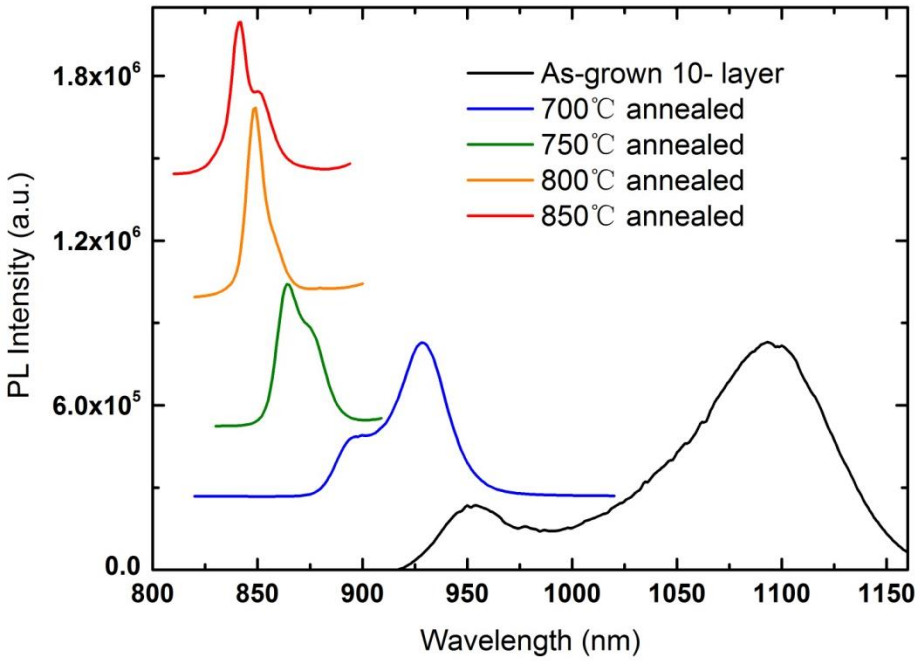

Figure 5.1: 77 K PL spectra of the as-grown QDSC and samples annealed at various temperatures.

To better understand the annealing effect, the change of QD energy band structure before and after thermal annealing is schematically illustrated in Figure 5.2. As a result of thermal annealing, the compositional inter-diffusion could lead to the modification of QD potential profile and thus a change of confinement energy and depth. The transition between QDs conduction band and valance band is blue-shifted due to higher (lower) electrons (holes) states. Correspondingly, the transition energy from WL/QD states to barrier states is decreased, which could lead to improved electrons escape and transport as will be discussed later on.

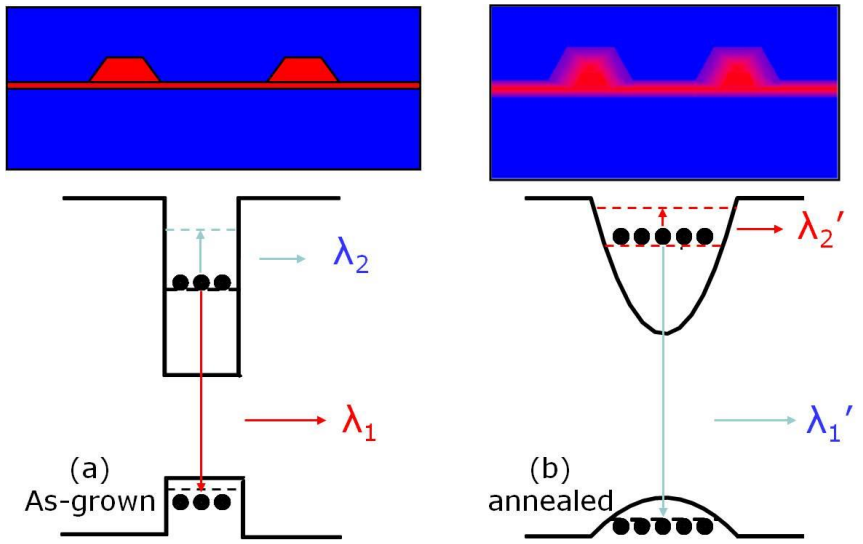

Figure 5.2: Schematic shows the energy band structure and potential difference of (a) as-grown QD structure, and (b) annealed QD layer in which inter-diffusion occurred.

Figure 5.3 plots the QD and WL PL emission energy shift as well as change of full width at half maximum (FWHM) compared with the as-grown sample as a function of annealing temperature. Apart from the obvious energy blue-shift, the linewidths of both WL and QD peaks become much narrower, indicating that a more homogenized QD size distribution is obtained after annealing treatment. In addition, it is also noted that the ratio of emission intensity between QDs and WL is decreased at higher annealing temperatures, and the 800 ℃, 850 ℃ annealed samples only show a small shoulder QDs peak. This implies that annealing at very high temperatures may lead to excessive In-Ga inter-diffusion, causing dissolution of the QDs into the wetting layer and adjacent GaAs space layer.

These results are consistent with the previously reported inter-diffusion studies of QDs [10, 11], confirming that annealing induced inter-diffusion has been successfully achieved in our QDSC samples. The QD confinement potential has been significantly modified, which is expected to affect carrier transport and device performance.

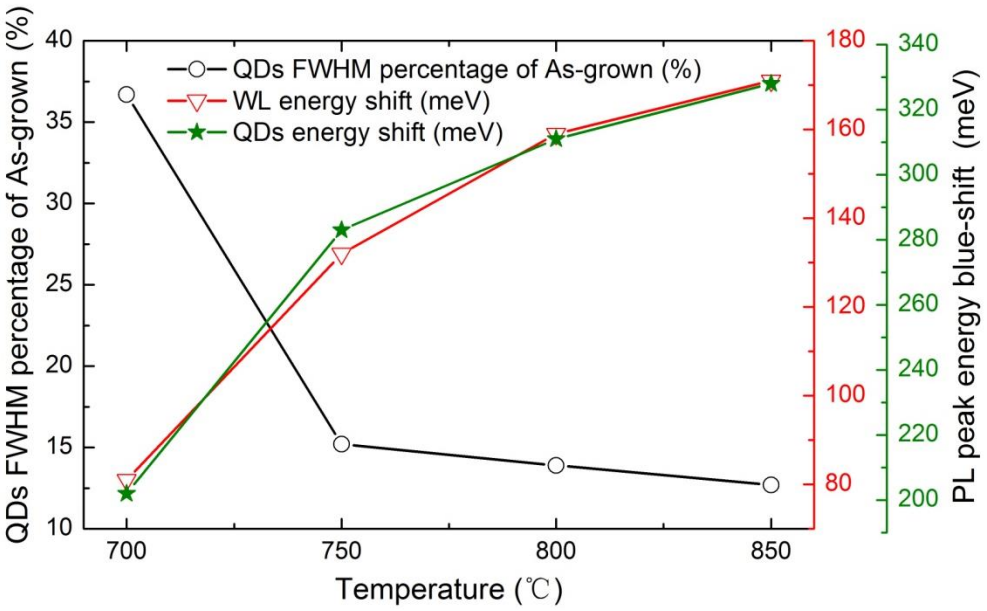

Figure 5.3: The ratio of QD PL peak linewidth (left) between annealed and unannealed sample, and PL peak energy blue-shift (right) of WL and QDs as a function of annealing temperature.

5.3.2 Dark current characteristics

Dark current is an important device parameter which should be minimized to achieve better solar cell performance. The dark current characteristics of InGaAs/GaAs QDSCs has been studied and discussed in previous chapters, as a complicated process due to multiple effects including the QD/WL confinement, progressive state filling and possible defect formation as a result of accumulated strain in the QD material [11, 15]. As mentioned earlier, the composition and 3D shape of the QDs are expected to be modified by annealing induced inter-diffusion, which could lead to the change of QD potential profile and the confinement depth. Therefore, the device dark current behaviour will also be significantly influenced, which will in turn affect the device performance.

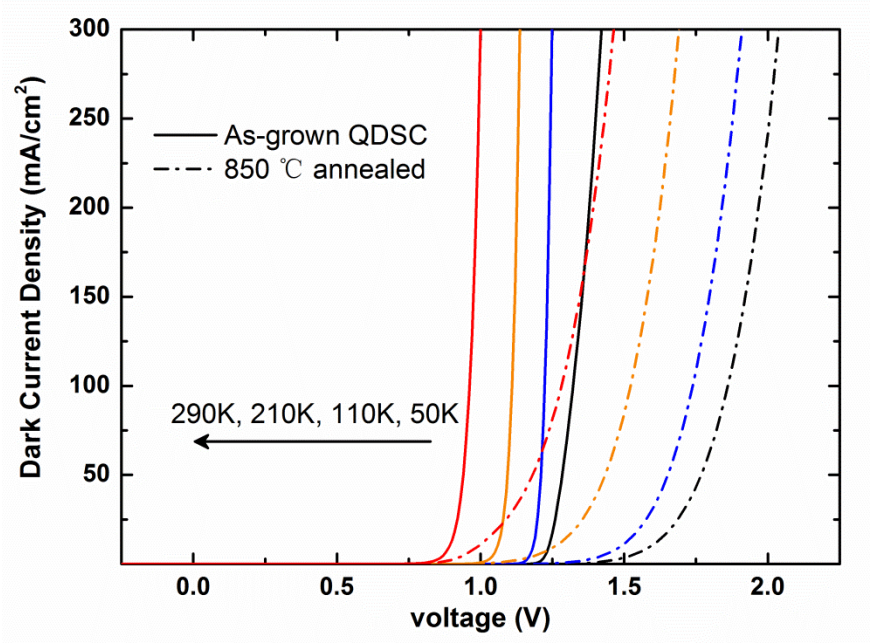

Figure 5.4: Temperature dependent dark J-V characteristics of as-grown 10-layer QDSC (solid line) and 850 ℃ annealed sample (dashed line).

Figure 5.4 displays the dark current density J (mA/cm^2) -V curves of as-grown 10-layer QDSC and the 850 ℃ annealed device, which were measured at various temperatures. Compared with the as-grown sample, the dark current of annealed sample is reduced and higher turn-on voltage is observed. By plotting the temperature dependent dark current at a fixed bias voltage, the thermal activation energy (E_a) could be deduced from the linear fitting of the slope of the curve based on the Arrhenius relationship [11],

$$I_{dark} \propto exp(-\frac{E_a}{k_b T}) \tag{5.1}$$

Where k_b is the Boltzmann constant and T is the measurement temperature in Kelvin. For our QDSCs, the activation energy for the thermally limited region is the difference between the GaAs barrier height and quasi-Fermi level of quantum confined states.

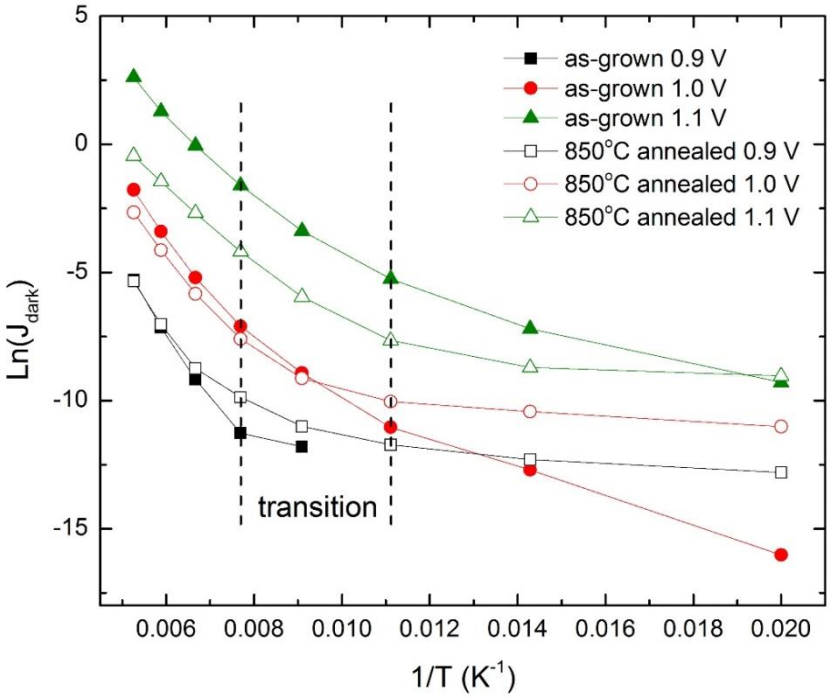

Figure 5.5: Arrhenius plot of the dark current versus inverse temperature (from 50 K to 200 K) for as-grown and 850 ℃ annealed 10-layer QDSCs, they were biased at 0.9, 1.0 and 1.1 V.

The natural logarithmic relationships of the dark current density versus inverse temperature (1/T) at biases of 0.9 V, 1.0 V, 1.1 V are plotted in Figure 5.5. Due to the measurement limit, the dark current at low temperatures and small biases cannot be measured accurately. Within the whole temperature range, all these curves exhibit a consistent increase with the temperature, however, the relationship is not linear.

There should exist two different regions during the whole temperature range, as have been observed previously in many GaAs quantum well/dot devices [10, 11, 16]. A thermally limited region (described well by the equation 5.1), and a defect-limited region, which could be distinguished from their different temperature dependent behaviours. The high temperature region was ascribed to the thermally limited region (through thermionic emission and field-assisted tunnelling), and the low temperature region to a defect-limited region. For the as-grown and annealed QDSC samples in this thesis, the transition between these two regions occurs at around 90-130 K under various biases as indicated in Figure 5.5. At higher temperatures, thermionic emission of electrons directly out of the QDs dominates the dark current, therefore the activation energy is nearly a constant. However, for temperatures below a certain value defect-assisted tunnelling and direct tunnelling of electrons become significant, directly tunnelling from the ground state is sometimes

referred to as sequential resonant tunnelling (SRT) [16]. At temperatures below the transition point the dark current of most devices is more independent of temperature indicating that defect-related tunnelling dominates the current within this temperature regime.

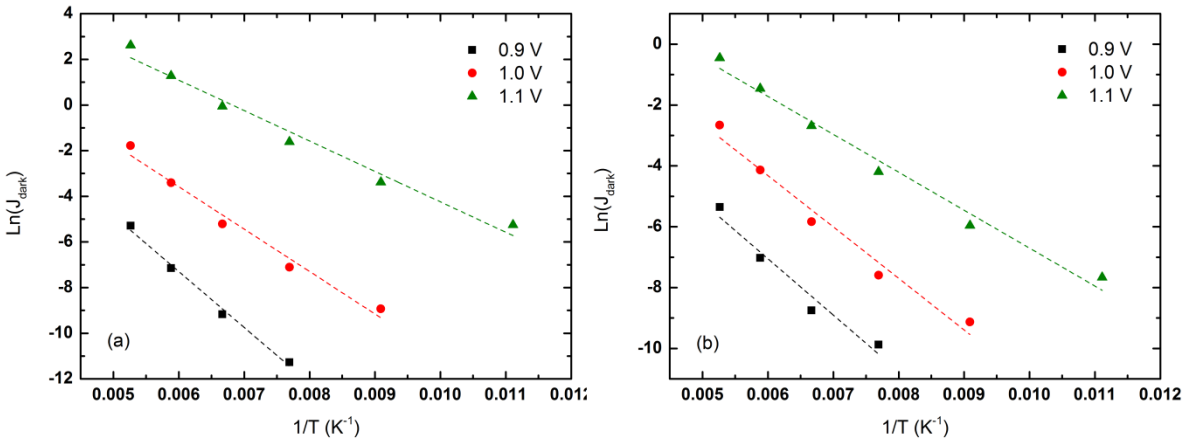

Figure 5.6: Arrhenius plot of the dark current versus inverse temperature and the fitting at linear region for (a) as-grown 10-layer QDSC and (b) 850 ℃ annealed sample at various biases.

As shown in Figure 5.6, by fitting the linear part in the relative high temperature region (> 90 K) using the Arrhenius relation (5.1), the activation energy E_a is estimated at three biases and listed in Table 5.1. The activation energy of QDSC after 850 ℃ annealing has decreased consistently. At the same time, when larger biases applied across the device electrons will be extracted from quantum structures by field-assisted tunnelling due to the strong band bending under high electric field, resulting in a large increase of dark current and much reduced activation energy. The reduced activation energy obtained for the 850 ℃ annealed sample confirms that thermal annealing causes the reduction of the QD and WL confinement energy. This implies that it will be easier for the photo-generated carriers to escape the bound states to the conduction band through thermally assistant tunneling, which will lead to improved solar cell performance. On the other hand, as discussed in Chapter 3, for the case of the QDSC, recombination within QDs makes a large contribution to the dark current. As the QD confinement is reduced, the capture cross-sections for electrons and holes are reduced leading to a much reduced dark current as observed in Figure 5.5. Moreover, thermal annealing may also reduce the overall defect density within the QD structures [11, 17] to decrease dark current and increase open circuit voltage.

Table 5.1: The calculated dark current activation energy (Ea) at various biases.

Devices	E_a (meV)		
	0.9 V	1.0 V	1.1 V
As-grown 10-layer QDSC	211	160	115
850 ℃ annealed sample	160	146	107

5.3.3 Solar cell performance

To understand the annealing effects on the solar cell performance, the light I-V characteristics of all the annealed samples were measured at AM 1.5G illumination condition and shown in Figure 5.7. The solar cell devices' parameters are all improved when higher annealing temperatures were used, as summarized in Table 5.2. It can be observed that both short-circuit current (J_{sc}) and open-circuit voltage (V_{oc}) are enhanced. Consistent with PL and dark current results, the improvements are due to the more homogenous QD size and much reduced confinement energy as a result of high temperature induced thermal inter-diffusion [6, 13]. This result is consistent with the analysis and prediction in section 5.3.2.

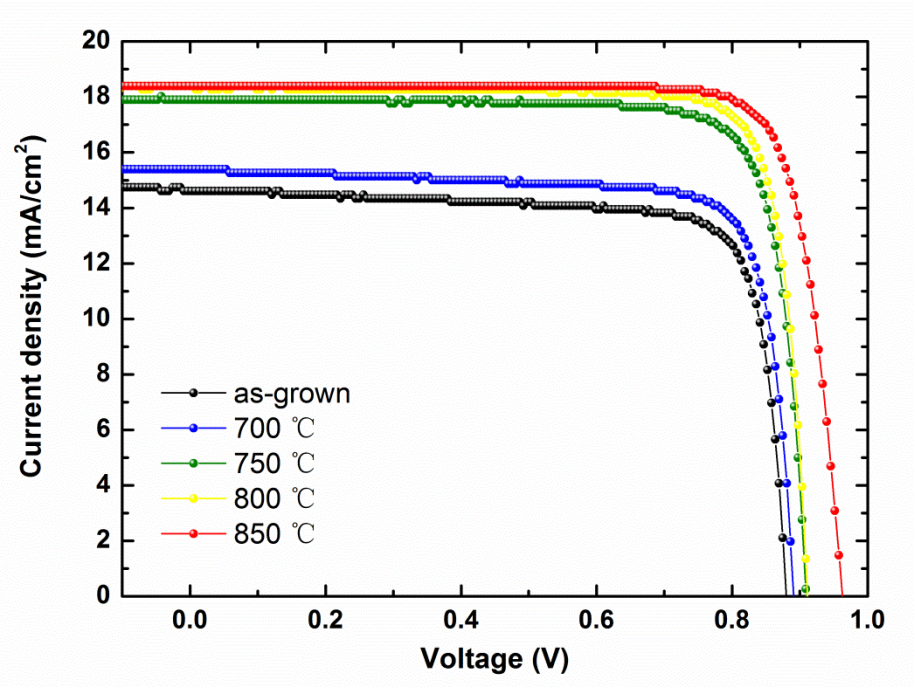

Figure 5.7: I-V curves tested under the 1-sun condition for as-grown QDSC and the samples annealed at different temperatures.

Table 5.2: Main solar cell parameters of the as-grown and annealed solar cell devices.

Samples	V_{oc} (V)	J_{sc} (mA/cm^2)	FF (%)	Efficiency (%)
As-grown QDSC	0.88	14.65	79.56	10.26
700 ℃ annealed	0.89	15.35	80.01	10.94
750 ℃ annealed	0.91	17.92	81.60	13.29
800 ℃ annealed	0.91	18.34	83.17	13.90
850 ℃ annealed	0.96	18.40	81.91	14.51

From the results listed in Table 5.2, the performance of the solar cell devices is improved steadily with the increase of the annealing temperature. The sample that was annealed at 850 ℃ displays the highest efficiency increase of 41.42 % from 10.26 % of the as-grown QDSC to 14.51 % of the annealed sample, indicating that post-growth annealing is an effective method to achieve high efficiency QDSCs.

However, there is a limit for the annealing temperature. Very high temperature will be harmful for the solar cell efficiency, because the QD structure will be nearly erased and severe dopant diffusion will degrade the electronic structure of the solar cell.

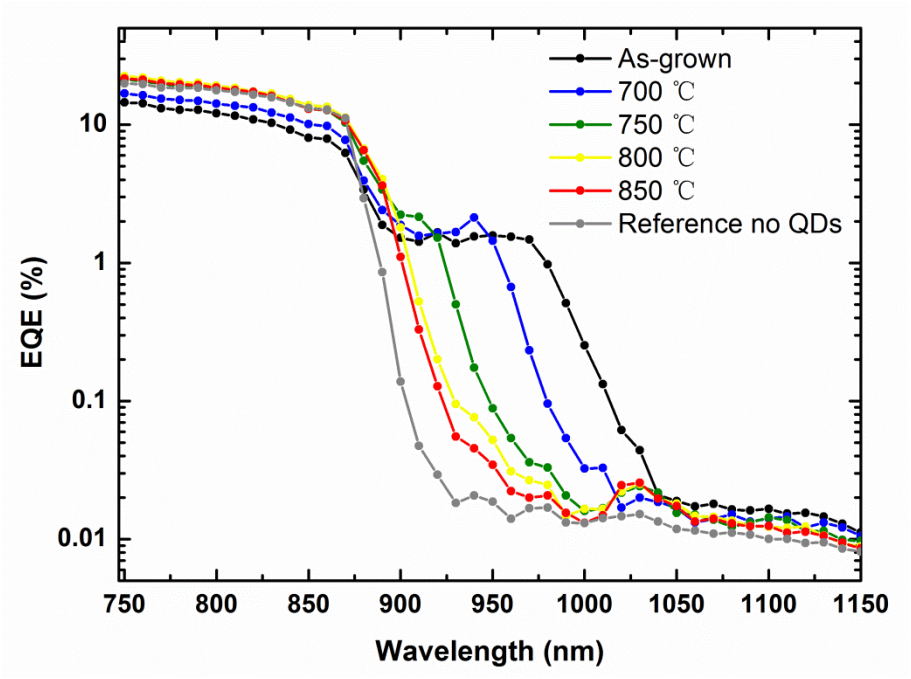

Figure 5.8: The external quantum efficiency (EQE) of all QDSC devices compared with the reference cell without quantum dot structure.

The external quantum efficiency of all five QDSC samples are measured and plotted in Figure 5.8, together with that from a p-i-n reference control cell. A consistent blue shift of WL response region is in good agreement with the blue shifted PL spectra with the annealing temperature as displayed in Figure 5.1. As the annealing temperature is increased, the WL region becomes narrower as a result of large inter-diffusion. It should also be noted that the EQE in GaAs region is also enhanced for all annealed samples, which means not only the photo carriers generated by QD and WL layers, but also those photocarriers created in GaAs barrier layers will benefit from shallower QD/WL confinement depth that enables carriers to transfer more efficiently through the entire junction structure. Also, thermal annealing may reduce the defects density within QD layers to decrease non-radiative recombination for better overall device performance.

5.3.4 Effect of dopant diffusion

Apart from the In and Ga inter-diffusion when InGaAs/ GaAs QD samples were annealed at high temperatures, the effect of dopant (in this study, Si for n-type and Zn for p-type doping) diffusion on device properties due to thermal annealing also needs to be taken into consideration. Indeed, dopant diffusion may vary the background doping concentration of the intrinsic layers (including GaAs, QD and WL layers), leading to a change of solar cell performance.

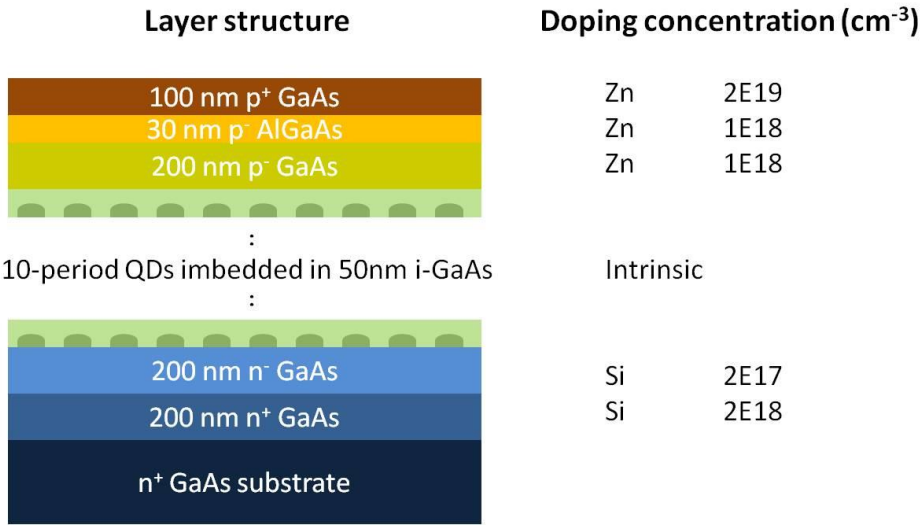

Figure 5.9: The nominal Zn and Si doping concentration profiles of the as-grown 10-layer QDSC.

To examine whether Si or Zn dopant were diffused into the unintentionally doped intrinsic QD region from n and p doped layers respectively, their concentration depth profiles were measured using the Secondary Ion Mass Spectrometry (SIMS) [18]. As a reference, the nominal doping levels of the as-grown QDSC by our MOCVD growth are plotted in Figure 5.9. And Figure 5.10 plots the Zn and Si atom concentration depth profiles before and after 850 ℃ annealing. The measurement starting point is the front surface of the QDSC sample. Compared with the initial composition steps in the as-grown sample, the amount of Si atoms diffusing into the intrinsic region after annealing is almost negligible to cause any significant effect on the device performance. On the other hand, it should be noticed that due to relatively large diffusion length of Zn dopant, the Zn concentration in the top p-layers is reduced significantly with a visible signal extending towards the substrate. A noticeable level of Zn can also be observed to diffuse into ~ 60 nm into the undoped QD structure with atomic concentration gradually changing from 10^{18} to 10^{17} cm^{-3}, which may resulted in a thin and slightly p-doped layers. This could affect the built-in electric field and depletion width in the solar cell structure, influencing the overall device performance [19]. Nevertheless, it doesn't seem to cause too much negative effects on the dark current, light I-V characteristics and also solar cell performance as shown in Table 5.2. Another interesting phenomenon can be observed here is the background Zn concentration in the as-grown sample, to a particularly high level of 10^{17} cm^{-3} in the QD region. This is not completely surprising since Zn background doping and diffusion is a well-recognized problem for III-V group semiconductors MOCVD growth [20-22]. Due to the relatively high temperature of 650 ℃ used for our QDSC doping layers growth, Zn may outdiffuse during the growth of the top p-doped layers into the intrinsic region moderating the overall background doping of the i-region. Indeed, a more careful investigation and understanding of the background doping may be very useful for further optimization of the background doping in the i-region of the QDSC structure for enhanced performance.

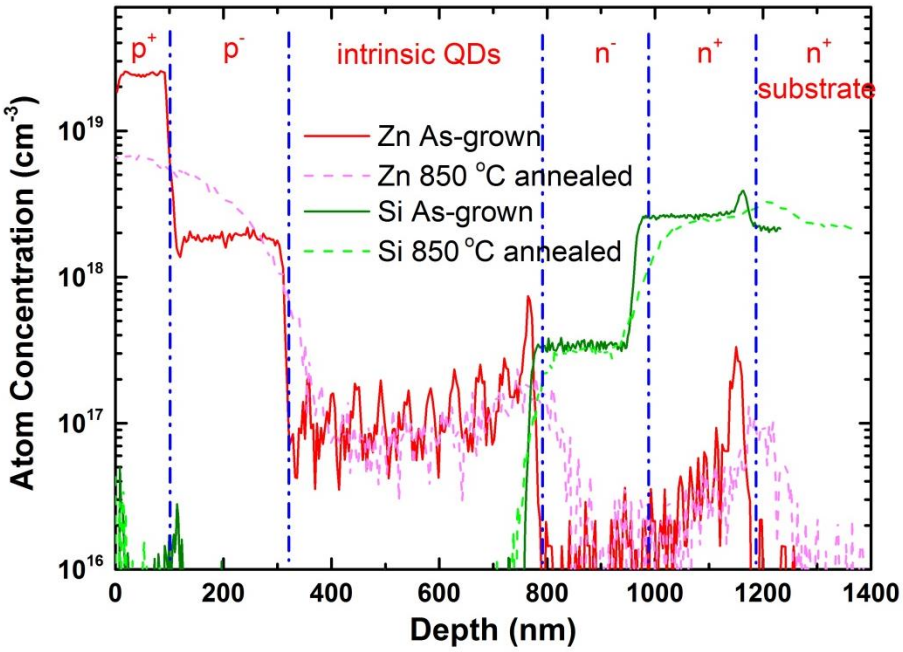

Figure 5.10: The Zn and Si dopants concentration depth profiles before and after 850 ℃ annealing by SIMS measurements.

5.4 Thermal annealing study on QDSCs with different stacking layer numbers

As discussed in Chapter 3, increasing QD stacking numbers were expected to provide stronger light absorption to improve short-circuit current and overall energy conversion efficiency. However, our 15, 20- layer samples display much reduced J_{sc} and efficiency than those of 10-layer solar cell. This is mainly due to much less efficient carrier extraction through the wider depletion region as well as increased defect density due to the accumulated strain. Based on the results from the annealing study on 10-layer QDSCs, which shows that increased annealing temperature is able to improve carrier transport and thus all the main device parameters, thermal annealing at 850 ℃ for 50 s was chosen to be performed to the 15- and 20-layer samples, to explore that if the thermal inter-diffusion is able to improve the performance of QDSCs with larger numbers of stacked layers.

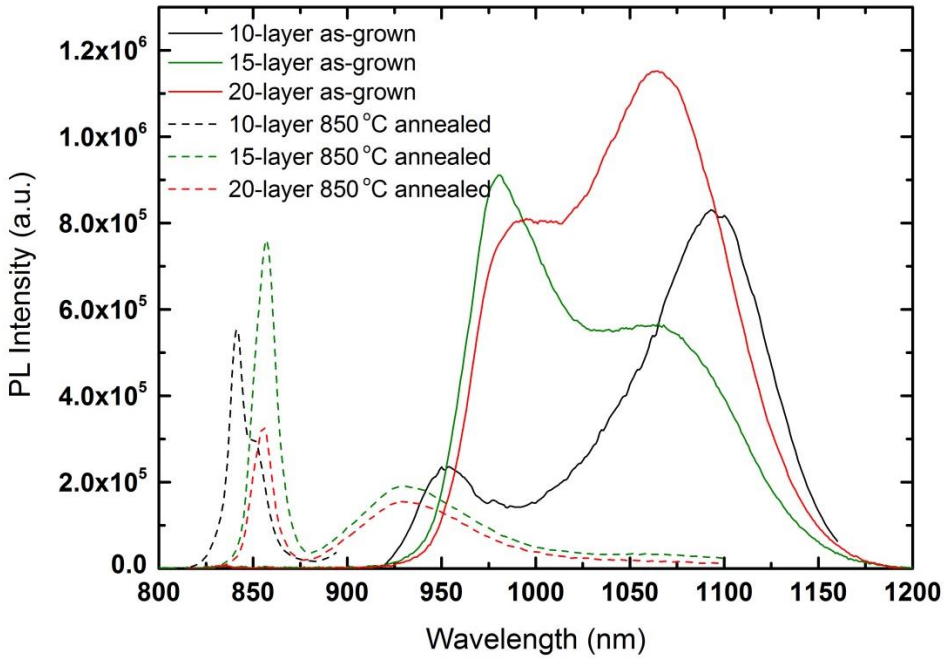

Figure 5.11: 77 K PL spectra of the as-grown 10, 15, 20-layer QDSCs and the samples annealed at 850 ℃.

Figure 5.11 plots the PL spectra from the 10, 15, and 20- layer as-grown samples and the corresponding annealed devices. The changes in PL spectra of the annealed 15, and 20- layer samples are consistent with the 10-layer sample as studied in the previous sections with the peak blue-shift attributed to increased energy states in both conduction band and valence band of QDs and WL, which is caused by the inter-diffusion of InGaAs quantum dot/ wetting layer with their surrounding GaAs materials. Apart from the obvious blue-shift, the linewidth of both WL and QD become smaller, which means relatively more homogenized QD size distribution is obtained after annealing as discussed in section 5.3. Also, the QDs emission intensity becomes relatively weaker than that of WL after annealing, indicating that annealing at 850 ℃ leads to abundant In-Ga inter-diffusion causing dissolution of the QDs into the wetting layer and adjacent GaAs space layer. Compared with the 10-layer sample, the 15- and 20-layer samples show slightly less QD peak shift. This may be due to their larger average QD size (see Chapter 3) and size distribution (than those of 10-layer sample), which restrict the effect of In-Ga inter-diffusion.

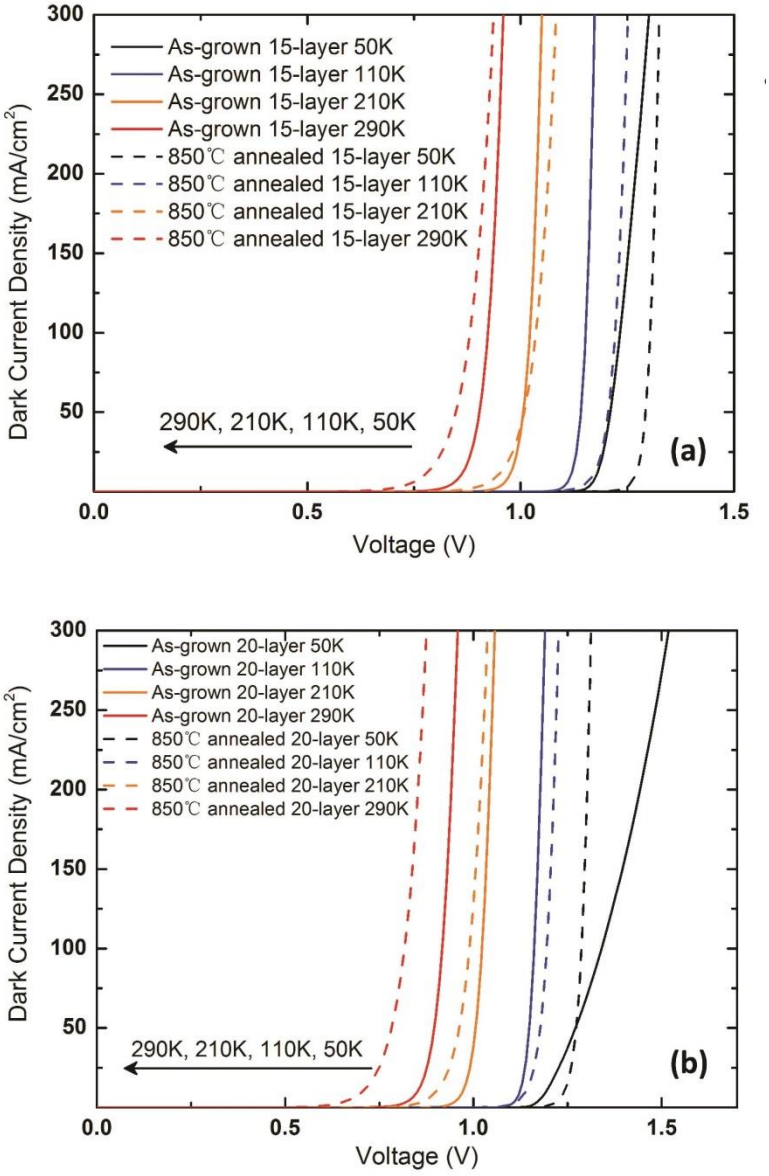

Figure 5.12: Temperature dependent dark J-V characteristics of as-grown (a) 15-layer and (b) 20-layer QDSCs (solid line) and the corresponding 850 ℃ annealed samples (dashed line).

The dark I-V characteristics were also measured for 15 and 20-layer QDSCs before and after 850 ℃ annealing as a function of temperature. Figure 5.12 demonstrates the dark current curves for these two devices measured at temperatures ranging from 50 K to 290 K, which show different behaviours compared with the 10-layer QDSC. For the 15-layer sample, when the temperature is relatively low (< 190 K), the dark current is reduced after annealing and turn-on voltage is slightly increased compare to the corresponding as-grown devices however with a much small change in values than those of 10-layer samples as shown in Figure 5.3. The situation is

reversed when the temperature is above about 210 K, a higher dark current is observed from high temperature annealed devices. For the 20-layer sample, the annealed device displays larger dark current at the whole temperature range (except for 110 K) implying possible competing transport processes in the sample.

In order to evaluate the change of QD potential depth of 15, 20-layer samples due to 850 ℃ annealing, the Arrhenius-relationship (equation (5.1)) was used again to calculate the activation energy E_a for the temperature dependence of the dark current to evaluate the change of the quantum dot confinement depth [11, 14]. The natural logarithm of the dark current density (Ln (J_{dark})) as a function of inverse temperature at a bias of 1.0 V is shown in Figure 5.13. All devices exhibit two distinct dark current regimes, a defect-limited low temperature regime and a thermally-assisted or thermionic emission dominated high temperature regime. The linear relation transition temperature for 15 and 20-layer samples is about 110 K, so the curve fitting here was also carried out in the linear region (> 110 K).

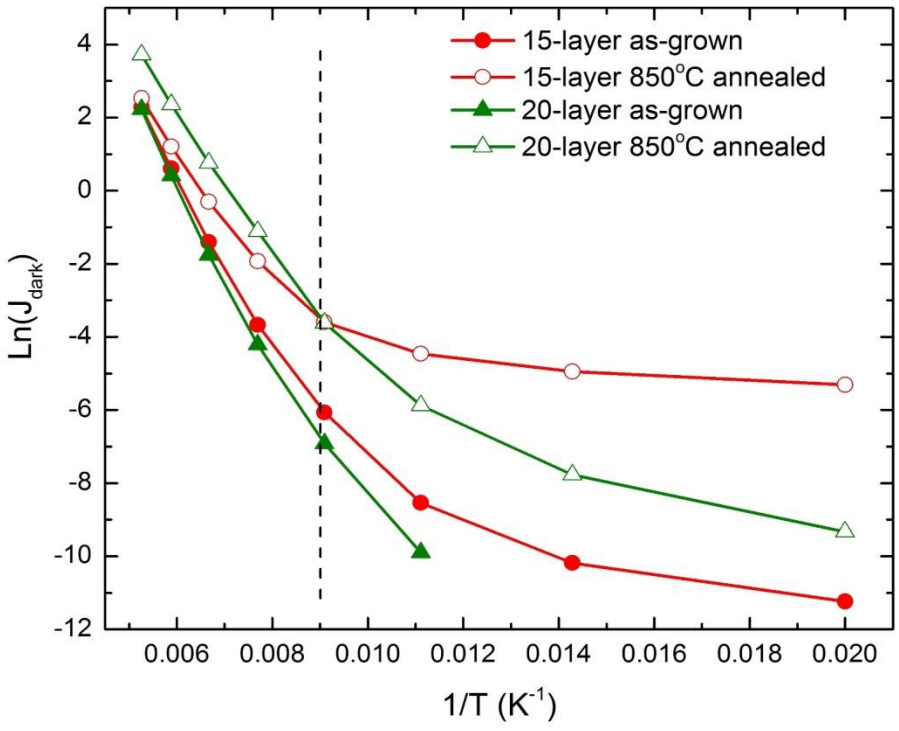

Figure 5.13: Arrhenius plot of the dark current versus inverse temperature at 1.0 V bias for 15-layer and 20-layer QDSCs before and after 850 ℃ annealing.

By fitting the linear parts of dark current curves in the temperature range of 110-190 K, the activation energy E_a for the 15- and 20-layer devices are

estimated at three biases and concluded in Table 5.3 (including results at various biases which are not shown in Figure 5.13). The activation energy of both 15 and 20-layer samples is decreased after 850 ℃ annealing, which agrees with the result obtained from the 10-layer device, indicating that thermal annealing caused reduction of the QD/ WL confinement energy. This implies that the photo-generated carriers can escape from the bound states to the conduction band of the GaAs barrier more efficiently, leading to reduced QD recombination and dark current in the annealed solar cell devices. Also, the E_a is found to be lowered as the applied bias is increased, which could be attributed to the increased thermally assisted tunnelling from the shallower bound states.

Table 5.3: The calculated dark current activation energy of 15 and 20-layer QDSC at various biases.

Samples	**Ea (meV)**		
	0.9 V	1.0 V	1.1 V
As-grown 15-layer QDSC	169	159	112
850 ℃ annealed sample	158	137	103
As-grown 20-layer QDSC	287	206	113
850 ℃ annealed sample	194	164	110

However, it is likely that extended defects also play a significant role in the 15- and 20-layer samples. In general, thermal annealing may be an effective way to remove low density of point defects formed in crystal structures to improve material quality and device performance. A good example of this is the annealing results of 10-layer QD cell discussed earlier in this chapter. On the other hand, high temperature annealing could also trigger the formation of extended defects to release the excessive strain in the highly strained multi-layer QD structures [12]. For our 15 and 20-layer samples, due to the increased accumulated strain (as discussed in Chapter 3), it is likely that some extended defects were formed during annealing [10, 12] resulting in an increased Shockley-Read-Hall (SRH) recombination rate and thus the increase of dark current. Therefore, for 15 and 20-layer samples, despite that reduced QD confinement energy after annealing could help to reduce the carrier recombination and dark current, the possible formation of extended defects on the other hand will increase the dark current. With an increase in number of QD layers, these two competing mechanisms lead to complex dark current

behaviors as observed in the annealed 15- and 20-layer QDSCs with larger dark current obtained in the 20-layer device due to increased strained and extended defect densities. This behaviour is also affected by temperature. The defects become more active as recombination centres at higher temperatures, because larger kinetic energy leads to shorter escape time from QDs/ WL confinement, which makes more carriers recombine through extended defects. However, at low temperatures the defects are saturated and related recombination is relatively low, the reduced QDs confinement depth and consequently lower recombination in QDs will still causes an overall smaller dark current than their respective as-grown reference samples.

To further study the thermal annealing effects on carrier recombination and thus the dark current mechanisms in the annealed QD solar cells, the local ideality factor (n) at various voltages calculated based on equation 3.3 (details see Chapter 3) [23] for 10, 15, 20-layer QD solar cells and corresponding annealed devices at 300 K are plotted in Figure 5.14.

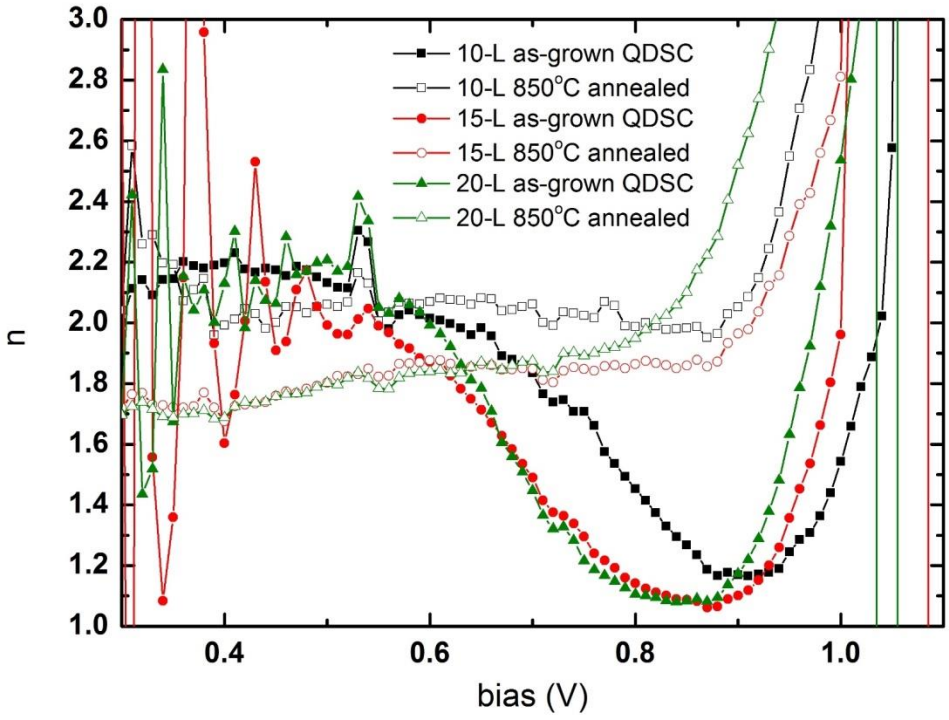

Figure 5.14: Voltage dependence of local ideality factor n(V) for 10, 15 and 20 layers QDSCs before and after 850 ℃ annealing.

The as-grown devices show obvious fluctuation of n-factor along with the voltage. However, after annealing all three devices present much more stable n-factor value, which is close to a constant in wide voltage range. This also

proves that annealing treatment could improve the materials quality of QDSC. For all devices, there is a large increase when the voltage is beyond ~0.9 V due to the series resistance effect at high current condition.

As discussed earlier in Chapter 3, we propose that there are two different recombination paths within QD layers making different contribution to the overall ideality factor of the QDSC. For all the QDSC devices, in the low bias region, the n-factor is larger indicating dark current is dominated by recombination in space charge region (SCR) due to either defect related recombination and/or QD-related recombination through simultaneous capture of electrons and holes by the same QD layer. At intermediate bias, the n-factors of devices reduce to the lowest value due to the formation of dark current outside the space charge recombination region or the first few QD layers already occupied by majority carriers under quasi-thermal equilibrium state which requires the transport of only one type of charge carrier through the depletion (SCR) region [15]. The 10-layer device shows a higher ,n-factor than that of the 15- and 20-layer samples, which may be due to the narrower depletion region width for the carriers to diffuse through more easily. For the annealed solar cells, their n-factor varies in two ways. For the low voltage region (< ~ 0.6 V), lower and smoother n-factor is obtained for all the annealed samples. This can be attributed to the annealing enhanced material quality and carrier transport and extraction that reduce the recombination in the SCR region. For the voltage region between 0.6 and 0.9 V, n-factor becomes higher after annealing. This is probably because under the assistance of higher applied bias, the injected carriers are easier to diffuse through the whole QD region and recombine with majority carriers outside the SCR regions, leading to increased dark current dominated by carrier diffusion. This is similar to GaAs reference cell behaviour as shown in section 3.6.3 as well, which results in a smaller slope of dark log (I)-V curve and larger n value compared to as-grown QDSCs. Overall, the effects of thermal annealing on n-factor indicate that annealing carried out in this chapter is likely to improve the carrier transport and materials quality of QDSC, and the dark current behaviour turns out to be closer to the one-diode exponential characteristic equation.

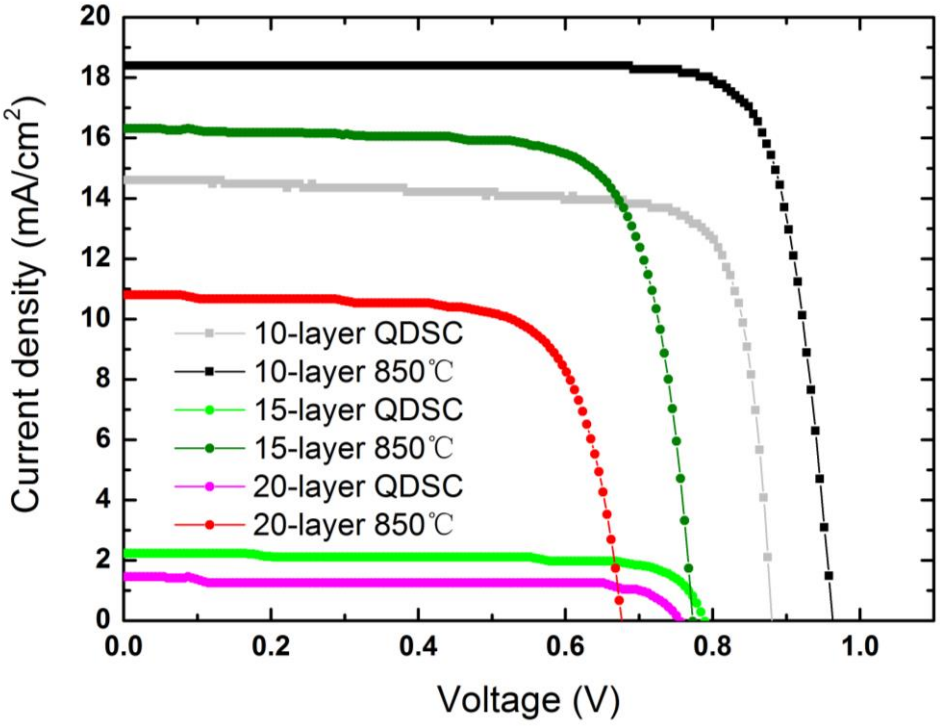

Figure 5.15: I-V curves under the 1-sun illumination condition for as-grown 10, 15, 20-layer QDSCs and the corresponding samples annealed at 850 ℃.

Figure 5.15 displays the I-V curves measured from the 10, 15 and 20-layer devices before and after 850 ℃ annealing. It is clear that after thermal annealing, the short-circuit current density (J_{sc}) of each QDSC structure is dramatically boosted, because the extraction and collection efficiency of photo-generated carriers is greatly improved by the modified QD confinement profiles. However, except for the 10-layer device, both 10 and 15-layer QDSCs show decreased V_{oc} after annealing, with a minor degradation for the former (from 0.79 V to 0.77 V) and large degradation (from 0.76 V to 0.68 V) for the latter. This may be directly correlated to the larger dark current [15, 24] due to the formation of extended defects and increased carrier diffusion at larger bias (> 0.6 V) in large QD stacking number samples after high temperature annealing.

Table 5.4: Solar cell parameters of the as-grown and annealed QDSC.

Samples	V_{oc} (V)	J_{sc} (mA/cm^2)	FF (%)	Efficiency (%)
As-grown 10-layer QDSC	0.88	14.65	79.56	10.26
850 ℃ annealed 10-layer QDSC	0.96	18.40	81.91	14.51
As-grown 15-layer QDSC	0.79	2.21	74.13	1.30
850 ℃ annealed 15-layer QDSC	0.77	16.27	75.99	9.56
As-grown 20-layer QDSC	0.76	1.35	75.57	0.77
850 ℃ annealed 20-layer QDSC	0.68	10.80	72.87	5.33

From the key device parameters summarized in Table 5.4, it can be found that the efficiency of annealed 15-layer QDSC displays the highest efficiency increase of 635 % from 1.30 % to 9.56 % compared to that of as-grown cell, and the 20-layer device is also improved significantly from 0.77 % to 5.33 % by a percentage of 592 %. This suggests that the carrier extraction has been significantly improved for the QDSC structures with large stacking QD layers. However their overall solar cell efficiencies are still lower than that of the 10-layer QDSC. One reason could be again due to the strain-related defects both before and after annealing for the QDSC with large QD stacking numbers. To solve this problem, more detailed work would be necessary to achieve strain balanced QD solar cells with large stacking numbers, based on which increased number of QD layers can be achieved without significant strain accumulation in the system. This will allow further post-growth thermal annealing to modify the QD confinement energy to improve the carrier extraction without causing formation of extended defect for improvement in both J_{sc} and V_{oc} and ultimately, the overall device efficiency.

5.5 Conclusions

To conclude, we have studied the effects of post-growth thermal annealing on the optical and electrical characteristics of $In_{0.6}Ga_{0.4}As$/ GaAs QDSCs with different QD stacking numbers. The large blue-shifts in the PL spectra have been observed for all the annealed samples, while the corresponding spectral linewidths are reduced compared to the as-grown devices. The annealing also changes the temperature dependant dark current behaviour of the devices which has been discussed in detail. The linear fitting for Arrhenius plots at higher temperature region indicates that the confinement depth related activation energy E_a is reduced after annealing. As a result, all the QD solar cell performances have shown improvement by thermal annealing. However,

for the highly strained QD structures, i.e., 15, 20-layer samples investigated in this study, in addition to the improved carrier extraction and transport after annealing, the strain relaxation on the other hand, may cause the formation of extended defects during the annealing process causing adverse effect on device performance. Development of strain balanced QD solar cells with large stacking numbers combined with post-growth thermal annealing may be a promising approach to achieve further improved solar cell efficiency. In addition, the Zn and Si dopants diffusion during annealing is also investigated and is found not to affect QDSC device main properties significantly.

References

[1] Zhuang, Q.D., H.X. Li, L. Pan, J.M. Li, M.Y. Kong, and L.Y. Lin, Self-organization of the InGaAs GaAs quantum dots superlattice. *Journal of Crystal Growth*, 1999. **201**: pp. 1161-1163.

[2] Sugaya, T., S. Furue, H. Komaki, T. Amano, M. Mori, K. Komori, S. Niki, O. Numakami, and Y. Okano, Highly stacked and well-aligned $In_{0.4}Ga_{0.6}As$ quantum dot solar cells with $In_{0.2}Ga_{0.8}As$ cap layer. *Applied Physics Letters*, 2010. **97**(18): pp. 183104.

[3] Riel, B.J., An introduction to self-assembled quantum dots. *American Journal of Physics*, 2008. **76**(8): pp. 750-757.

[4] Priester, C. and M. Lannoo, Origin of Self-Assembled Quantum Dots in Highly Mismatched Heteroepitaxy. *Physical Review Letters*, 1995. **75**(1): pp. 93-96.

[5] Mokkapati, S., H.H. Tan, and C. Jagadish, Multiple wavelength InGaAs quantum dot lasers using selective area epitaxy. *Applied Physics Letters*, 2007. **90**(17): pp. 171104.

[6] Jolley, G., I. McKerracher, L. Fu, H.H. Tan, and C. Jagadish, The conduction band absorption spectrum of interdiffused InGaAs/GaAs quantum dot infrared photodetectors. *Journal of Applied Physics*, 2012. **111**(12): pp. 123719.

[7] McKerracher, I., J. Wong-Leung, G. Jolley, L. Fu, H.H. Tan, and C. Jagadish, Selective Intermixing of InGaAs/GaAs Quantum Dot Infrared Photodetectors. *Ieee Journal of Quantum Electronics*, 2011. **47**(5): pp. 577-590.

[8] Aroutiounian, V., S. Petrosyan, A. Khachatryan, and K. Touryan, Quantum dot solar cells. *Journal of Applied Physics*, 2001. **89**(4): pp. 2268-2271.

[9] Hubbard, S.M., C.D. Cress, C.G. Bailey, R.P. Raffaelle, S.G. Bailey, and D.M. Wilt, Effect of strain compensation on quantum dot enhanced GaAs solar cells. *Applied Physics Letters*, 2008. **92**(12): pp. 123512.

[10] Fu, L., H.H. Tan, I. McKerracher, J. Wong-Leung, C. Jagadish, N. Vukmirovic, and P. Harrison, Effects of rapid thermal annealing on device characteristics of InGaAs/GaAs quantum dot infrared photodetectors. *Journal of Applied Physics*, 2006. **99**(11): pp. 114517.

[11] Jolley, G., L. Fu, H.H. Tan, and C. Jagadish, Effects of annealing on the spectral response and dark current of quantum dot infrared photodetectors. *Journal of Physics D-Applied Physics*, 2008. **41**(21): pp. 215101.

[12] Stewart, K., M. Buda, J. Wong-Leung, L. Fu, C. Jagadish, A. Stiff-Roberts, and P. Bhattacharya, Influence of rapid thermal annealing on a 30 stack InAs/GaAs quantum dot infrared photodetector. *Journal of Applied Physics*, 2003. **94**(8): pp. 5283-5289.

[13] Srujan, M., K. Ghosh, S. Sengupta, and S. Chakrabarti, Presentation and experimental validation of a model for the effect of thermal annealing on the photoluminescence of self-assembled InAs/GaAs quantum dots. *Journal of Applied Physics*, 2010. **107**(12): pp. 123107.

[14] Leon, R., Y. Kim, C. Jagadish, M. Gal, J. Zou, and D.J.H. Cockayne, Effects of interdiffusion on the luminescence of InGaAs/GaAs quantum dots. *Applied Physics Letters*, 1996. **69**(13): pp. 1888-1890.

[15] Lu, H.F., L. Fu, J. Greg, T. Hark Hoe, T. Sudersena Rao, and J. Chennupati, Temperature dependence of dark current properties of InGaAs/GaAs quantum dot solar cells. *Applied Physics Letters*, 2011. **98**(18): pp. 183509.

[16] Stiff-Roberts, A.D., X.H. Su, S. Chakrabarti, and P. Bhattacharya, Contribution of field-assisted tunneling emission to dark current in InAs-GaAs quantum dot infrared photodetectors. *Ieee Photonics Technology Letters*, 2004. **16**(3): pp. 867-869.

[17] Lever, P., H.H. Tan, and C. Jagadish, Impurity free vacancy disordering of InGaAs quantum dots. *Journal of Applied Physics*, 2004. **96**(12): pp. 7544-7548.

[18] Chia, A.C.E., J.P. Boulanger, and R.R. LaPierre, Unlocking doping and compositional profiles of nanowire ensembles using SIMS. *Nanotechnology*, 2013. **24**(4): pp. 045701.

[19] Schubert, E.F., C.J. Pinzone, and M. Geva, Phenomenology of Zn diffusion and incorporation in InP grown by organometallic vapor-phase epitaxy (OMVPE). *Applied Physics Letters*, 1995. **67**(5): pp. 700-702.

[20] Tsang, W.T., F.S. Choa, and N.T. Ha, Zinc-doping of InP during chemical beam epitaxy using diethylzinc. *Journal of Electronic Materials*, 1991. **20**(8): pp. 541-544.

[21] Kellert, F.G., S.R. Sloan, M.J. Ludowise, and J.E. Turner, Zn-doping in OMVPE Grown lnP:Zn/lnGaAs/lnPp-i-n double heterojunctlons with lnGaAs:Zn contacting layers. *Journal of Electronic Materials*, 1992. **21**(10): pp. 983-987.

[22] Sun, S.Z., E.A. Armour, K. Zheng, and C.F. Schaus, Zinc and tellurium doping in GaAs and $Al_xGa_{1-x}As$ grown by MOCVD. *Journal of Crystal Growth*, 1991. **113**(1): pp. 103-112.

[23] Gu, T.Y., M.A. El-Emawy, K. Yang, A. Stintz, and L.F. Lester, Resistance to edge recombination in GaAs-based dots-in-a-well solar cells. *Applied Physics Letters*, 2009. **95**(26): pp. 261106.

[24] Jolley, G., H.F. Lu, L. Fu, H.H. Tan, and C. Jagadish, Electron-hole recombination properties of $In_{0.5}Ga_{0.5}As$/GaAs quantum dot solar cells and the influence on the open circuit voltage. *Applied Physics Letters*, 2010. **97**(12): pp. 123505.

Chapter 6

Plasmonic nanoparticles enhanced quantum dot solar cells

6.1 Introduction

As discussed previously, while increase in short-circuit current (I_{sc}) can be achieved via QDs/barrier layer modulation/delta doping [1, 2] or by incorporating a large number of QD layers [3, 4], maintaining similar values of open-circuit voltage (V_{oc}) of QDSC (to that of reference GaAs solar cell) still remains a major challenge even for the best reported results [2, 5, 6]. This is in addition to the fact that both approaches require careful and extensive optimization of epitaxial growth conditions, especially increasing the number of QD layers tends to result in strain accumulation and increased defects density within the QDs and thus poorer over-all device performance (as investigated in Chapter 3). Another method was explored in Chapter 5, in which post-growth thermal annealing was carried out to modify the QDs confinement states. As a result, carriers collection efficiency has been improved leading to an increase of the overall solar cell efficiency.

Apart from these methods, another way to increase the absorption of the QDs is to use plasmonic effect. In this chapter, the use of Ag nanoparticles as the plasmonic scatterer on the performance of QDSC is investigated.

6.1.1 Plasmonics for thin absorber solar cells

Further cost reduction of photovoltaics to make it more competitive with conventional fossil fuel energy has been the ongoing focus of fundamental research and photovoltaic industry in recent years. For example, crystalline silicon is the dominant material in the solar panel market, for which the wafer thickness is between 180-300 μm, and most of the cost of Si solar cells is due to materials and the waste during fabrication and processing [7]. Therefore there has been great progress in development of thin-film solar cells, with film thickness in the range of 1-10 μm, which can be deposited on cheap substrates such as glass, plastic or stainless steel. Thin-absorber solar cells can be made from a variety of semiconductors including amorphous Si, GaAs, CdTe and $CuIn(Ga)Se_2$, as well as organic materials [8-12]. For realization of low-cost high performance thin film photovoltaics, new device design and/or strategy

to achieve full light absorption in thin film layers are therefore critical, such as light trapping structure [13].

Light trapping refers to the process of folding light into a thin absorber layer to increase its absorption probability. The traditional light trapping method for enhancing absorption in a Si solar cell is to employ front or back surface texturing that scatters light into the active layer at multiple angles, thereby increasing the light path length [14-16]. But this type of geometry is not suitable for thin-absorber solar cells, because the required surface roughness may be too large for active layer thickness and may cause more surface recombination. A more effective way of achieving light trapping for thin-absorber solar cells is to use metallic nanostructures that produce surface plasmons. Surface plasmons are electromagnetic oscillations of electrons at the interface between a metal and a dielectric, which have the ability to confine light within small scale materials [13, 17].

In general, plasmonic structures can offer at least three ways to reduce the physical thickness of the active layer that is required to absorb as much incident light as possible: light scattering from metal nanoparticles, near-field concentration effects by localized surface plasmons, and waveguide modes at the metal/semiconductor interface (i.e. surface plasmon polariton modes) [18, 19]. Enhancement of absorption using above three mechanisms have all been demonstrated for thin absorber solar cells [18]. As shown in Figure 6.1, the contribution of each mechanism depends on the particle size, location of nanoparticles and the structural design of the applied solar cell devices. Near-field concentration requires the nanoparticles to be embedded into active layer, while waveguide modes need the metal/ semiconductor interface very close to the active layer. Both techniques may not be suitable for application of solar cell structures fabricated through epitaxial methods, where interruption of epitaxial growth process with extra processing steps are highly impractical and undesirable for device application. On the other hand, light scattering can be produced by post-growth deposition of metal nanoparticles to couple light into the active layer to obtain enhanced far-field absorption through the high angle scattering of the nanoparticles. By trapping light in the condition it is coupled into the absorber layer outside of the escape cone [20] (or at angles larger than the critical angle for total internal reflection at the absorber-air interface), the plasmonic particles can be deposited on solar cell surface without the need to modify the growth and processing steps.

The use of plasmonics in this absorber layer was first demonstrated by Stuart and Hall [21] and has been extensively studied since then [13, 18, 19]. Enhanced performance of GaAs thin film solar cells due to plasmonic light

trapping has been also reported by depositing Ag nanoparticles on GaAs through anodic aluminium oxide templates [22]. In these reports, plasmonic light trapping were incorporated into the solar cells after the main device fabrication steps and does not alter the basic device structure/processing steps.

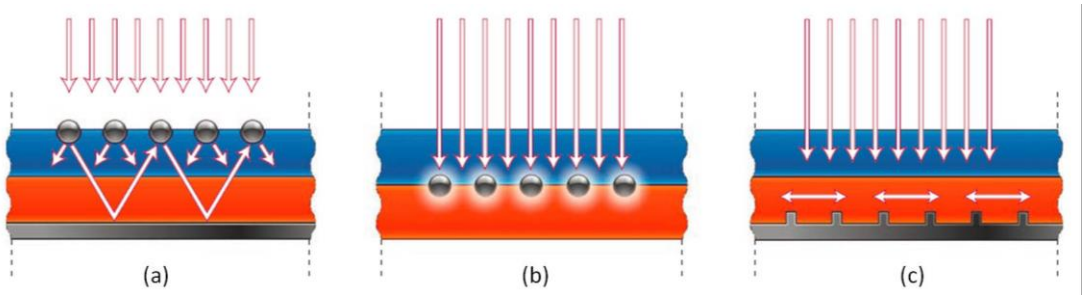

Figure 6.1: Three plasmonic light trapping strategies. (a) scattering from metal nanoparticles at the surface of the solar cell. (b) excitation of localized surface plasmons (near-field concentration effect) in metal nanoparticles embedded in the semiconductor. (c) excitation of surface plasmon polaritons (waveguide modes) at the metal/semiconductor interface. The picture is adapted from reference [18].

6.1.2 Plasmonic light trapping for quantum dot solar cells

As studied in previous chapters for the InGaAs/GaAs QDSCs, by incorporating self-assembled QDs into the intrinsic region of a standard p-i-n solar cell structure during the epitaxial growth, photons in the solar spectrum with energy lower than the energy gap of the bulk GaAs material can be absorbed by the QD layers, leading to an extended photoresponse into longer wavelengths and hence improved short circuit current density (J_{sc}) (compared with the GaAs reference cell) [6, 23-25].

However, due to the small absorption cross section [26] and limited number of QD layers in QDSCs (as discussed earlier in chapter 3), the absorption of long wavelength light in QD layers is still small. For example, less than 1 % of the incident light with wavelength larger than 875 nm is absorbed in a single pass across a 7 nm thick $In_{0.21}Ga_{0.79}As$ quantum well according to the calculation, which implies inefficient absorption in InGaAs QDs as well [27]. In order to absorb a higher fraction of light beyond the band edge of bulk GaAs in the solar cell, the long wavelength light absorption efficiency of the wetting layer and quantum dots needs to be increased substantially. One promising approach is to increase the effective optical path length, which can be achieved by trapping the weakly absorbed long wavelength light inside the solar cell structure through plasmonic effects.

In this chapter, we propose to enhance the long wavelength range (870-1180 nm) photon absorption of the QDSCs by employing light trapping provided by plasmonic nanoparticles. Due to its direct bandgap and large absorption coefficient, light trapping is not necessary for bulk GaAs layers. However, it is critical for QD layers (including wetting layers and QDs) in intrinsic region due to the very thin physical thickness (thinner than the required absorption length of corresponding wavelength light). As mentioned earlier, for the QD solar cells studied in the thesis, the QD active layers are embedded into the middle of the p-i-n cell structure, where the plasmonic effects based on near-field enhancement and SPP mechanism cannot be applied effectively due to the requirement for the position of the plasmonic structures to be in the vicinity of absorbing layers. Therefore for QDSC we employ the high angle scattering effect of plasmonic nanoparticles to provide light trapping for the long wavelength light that is not absorbed by the QD layers through the first light pass.

Light trapping can be achieved by depositing metal nanoparticles either on the front or on the rear side of the solar cells and has been investigated previously[28-30]. It has been found that below the particle plasmon resonance frequency, light scattered by the nanoparticles is in phase with respect to the incident light, whereas for higher frequencies (shorter wavelengths), the light scattered by the nanoparticles is out of phase with respect to the incident light [31]. When nanoparticles are deposited on the illuminated surface (i.e. most cases the front surface) of the solar cell, due to the phase difference, interference between light directly transmitted into the solar cell (without interaction with the nanoparticles) and light scattered into the solar cell by the nanoparticles leads to lower net intensity inside the solar cell for light with frequencies higher than the particle plasmon resonance frequency. Lower net intensity of this range light absorbed by the solar cell will degrade the photoresponse of the device at short wavelength range, resulting in overall reduced J_{sc}. However, if the same nanoparticle structures are deposited on the rear side of the solar cells, this problem could be avoided [28, 29] because short wavelength light is almost entirely absorbed in the bulk GaAs layers in the first single pass, before it reaches the rear surface and interacts with the nanoparticles. Only the long wavelength light (with energy lower than the bandgap of GaAs) that is not completely absorbed in the solar cell after the first pass will interact with the nanoparticles and be scattered back into the solar cell leading to enhanced optical path length. Enhanced path length for the long wavelength light will then increase the corresponding absorption in the WL/QD layers. For this reason, nanoparticles on the rear surface of the quantum dot solar cells are expected to enhance the QD

absorption without affecting short wavelength light absorption as to be investigated in this study. In addition, a dielectric spacer layer between the plasmonic particles and the semiconductor was investigated as it allows the plasmonic resonance frequency and scattering cross-section of nanoparticles to be tuned by spacer materials and thickness.

The plasmonic nanoparticles can be fabricated by depositing a thin film metals on the modified surface of a finished solar cell and annealing it in N_2 atmosphere [29, 32]. The difference in surface energy between the metallic layer and the spacer layer leads to the formation of nanoparticles. The fabrication process is relatively simple, does not require modification of the solar cell fabrication process and is scalable to large areas. The formation of nanoparticles can be tuned and improved by a dielectric spacer layer between metal and device surface as shown in section 6.3. To choose nanoparticle materials from different metals, aluminium and silver have highest density of free electrons which is good for the production of plasmon resonance, but the scattering crosss-section of Al native oxide and its high reflectance make it not suitable for this purpose [33]. For light trapping applications in the infrared wavelength range beyond 700 nm, both Au and Ag exhibit good dielectric functions [30]. The other issue critical to the performance of plasmonic structure is the parasitic losses inherent to the metallic nanoparticles since the intention of light trapping is to increase absorption of light in the solar cell, minimising photon loss due to absorption in the metallic material itself. Ag has lower absorption and is also less expensive than Au, therefore silver was chosen as the metal source for plasmonic nanoparticles investigated in this study.

6.2 Simulation method

In order to achieve good light trapping using plasmonic structures we need to maximise the scattering cross-section of the Ag plasmonic nanoparticles and the fraction of the scattered light that is coupled into the WL/QDs. Maximising the scattering cross-section is required to make sure that the nanoparticles interact with most of the incident light and randomise its direction. Coupling of large fraction of scattered light into the substrate is necessary to minimize the transmission losses on the rear surface. Also, the peak of the resonance frequency needs to be aligned to the wetting layer and QD emission peak positions in order to maximise the light absorption effects. However, it was found that the Ag nanoparticles with desired shape cannot be

formed on GaAs surface directly so a spacer layer is required to optimize nanoparticle formation.

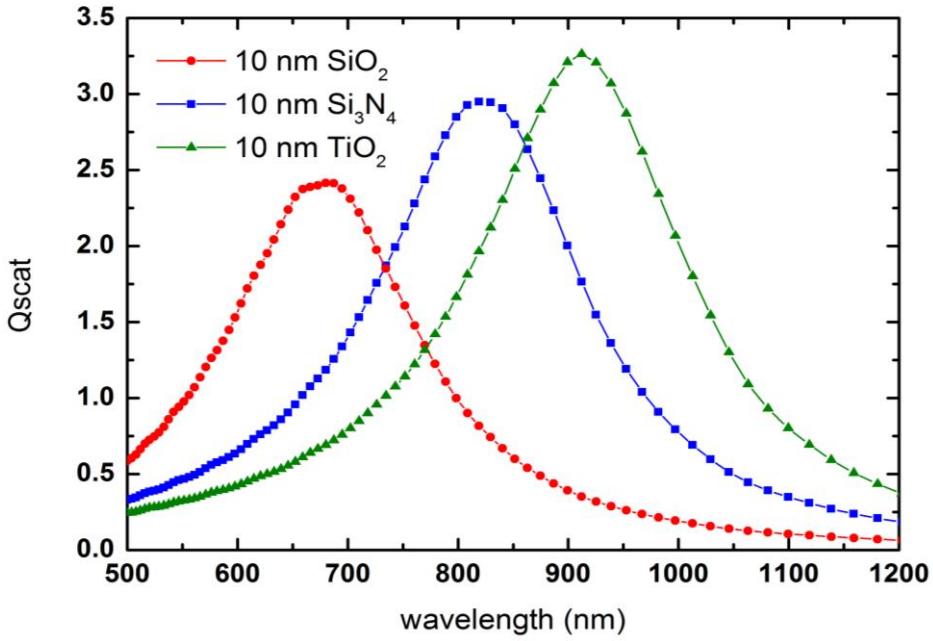

Figure 6.2: The scattering cross-section (Q_{scat}), normalized to the actual cross-sectional area, for a 120 nm diameter Ag hemisphere particle on GaAs substrate with different spacer layers (10 nm thick) in between.

The scattering cross-sections (Q_{scat}) and the fraction of scattered light coupled into the substrate (F_{sub}) were calculated by simulating light scattering from single nanoparticle using the commercially available software, Lumerical which is based on finite-difference time-domain method (FDTD) [34].

The resonance frequency and scattering cross-section of nanoparticles are determined by metal particle size and shape, spacer layer material and its thickness. First, the effect of size of Ag hemispherical particle on plasmonic behaviour was simulated. 120 nm diameter was determined to be the optimal size for the configuration without a spacer layer, because it provides high scattering cross-section and the resonance peak (~1083 nm) matches the WL/QD absorption range. On the other hand, because the surface plasmon can be tuned by varying the dielectric constant of the embedded spacer, and a higher index will lead to a relative red-shift of the resonance peak [35, 36]. Three different types of space layers placed between the GaAs substrate and 120 nm Ag nanoparticle were investigated. The wavelength dependent scattering behaviours are plotted in Figure 6.2. All the dielectric layers have a

same thickness of 10 nm. It is clear that compared to SiO_2 and Si_3N_4, TiO_2 exhibits the highest Q_{scat} and with the peak wavelength the closest to the QD region. TiO_2 was chosen as the spacer material in this study, however it is necessary for tuning the particle plasmon resonance peak closer to the band edge of QDs by changing the thickness of spacer layer, without modifying the nanoparticle size each time.

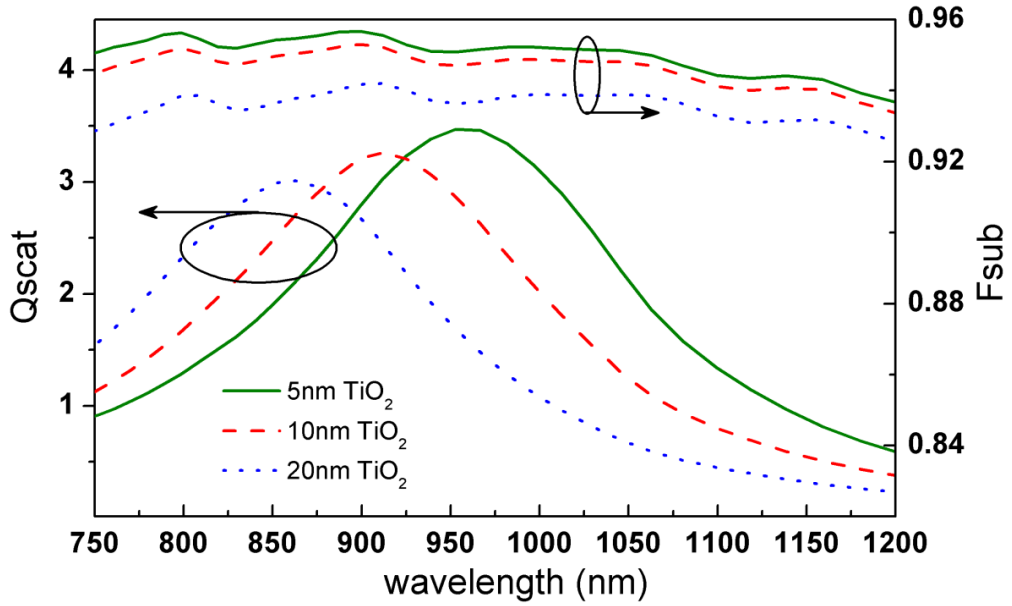

Figure 6.3: The scattering cross-section (Q_{scat}), normalized to the cross-sectional area, and fraction of scattered light coupled into the substrate (F_{sub}) for a 120 nm diameter Ag hemisphere on GaAs substrate with varying thickness of TiO_2 spacer layer.

Furthermore, Figure 6.3 shows the calculated scattering cross-sections (as normalized to the physical cross-sectional area of the particle) and the fraction of scattered light coupled into the substrate for a 120 nm diameter hemispherical Ag particle on GaAs substrate with different TiO_2 space layer thickness between them. The fraction of scattered light coupled into the substrate is determined by calculating the ratio of power scattered into the substrate to the total power scattered (into air and into the substrate) by the Ag particles. From Figure 6.3 the scattering cross section of the nanoparticles increases in magnitude, and red-shifts to longer wavelengths with decreasing TiO_2 layer thickness. Also, the fraction of scattered power coupled into the substrate is the highest over the whole wavelength range for the 5 nm TiO_2 space layer. The proximity of a high refractive index substrate affects the peak position of the particle scattering cross-section by modifying the polarizability of the particles due to dynamic depolarization effects, and this effect has been widely reported [29, 35, 37]. Thinner spacer layer ensures high degree of

overlap between the nanoparticle localized surface plasmons (near field) and the substrate, and high near field overlap can increase the field that drives the dipole oscillations in the nanoparticles. This will lead to an increase in the magnitude of scattering intensity from the nanoparticles [28] and it also results in better coupling of scattered light into the substrate [30]. For optimal device performance, the nanoparticle scattering cross-section and fraction of scattered light coupled into the substrate should be the highest around the WL/QD absorption energy, to ensure that most of the light incident on the nanoparticles at these wavelengths is efficiently scattered back into the solar cell. The results in Figure 6.3 clearly show that 5 nm TiO_2 spacer layer deposited on back GaAs surface and followed by 120 nm diameter hemispherical Ag nanoparticles is the best configuration for the selected wavelength range that of interest to our study.

6.3 Optimization of Ag nanoparticles formation

To form the Ag nanoparticles on the back of QDSC with proper diameter and size distribution, Ag thin films with various thicknesses were first evaporated on GaAs substrates with and without a pre-deposited TiO_2 layer. The samples were then annealed in N_2 ambient at 200 ℃ for 50 min. The difference in surface energy between the Ag metallic layer and the GaAs substrate (or TiO_2 layer) leads to the formation of isolated nanoparticles.

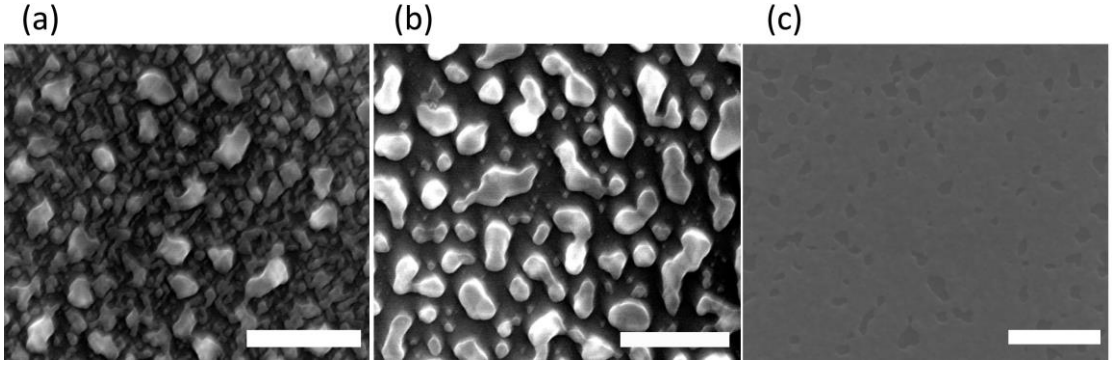

Figure 6.4: SEM images showing the morphology of Ag after 200 ℃ annealing, with (a) 10 nm, (b) 12 nm, and (c) 15 nm thick Ag films deposited on bare GaAs surface. The scale bars are 500 nm.

Silver films with 10, 12 and 15 nm thicknesses were deposited directly on the bare GaAs surface by thermal evaporation. After 200 ℃ annealing for 50 min, the morphology of Ag surface with different thickness are compared in Figure 6.4. It can be seen that Ag deposition directly on GaAs resulted in

highly non-uniform particles, and beyond a certain deposition amount (~15 nm) it remains as a film rather than isolated islands as shown in the SEM image of Figure 6.4 (c). This may be due to the reason that at this thickness, the surface energy difference between Ag and GaAs is not sufficient to isolate Ag materials. Also, the interface energy of Ag/GaAs could be too large to allow effective formation of uniform nanoparticles as required in the plasmonic configuration design.

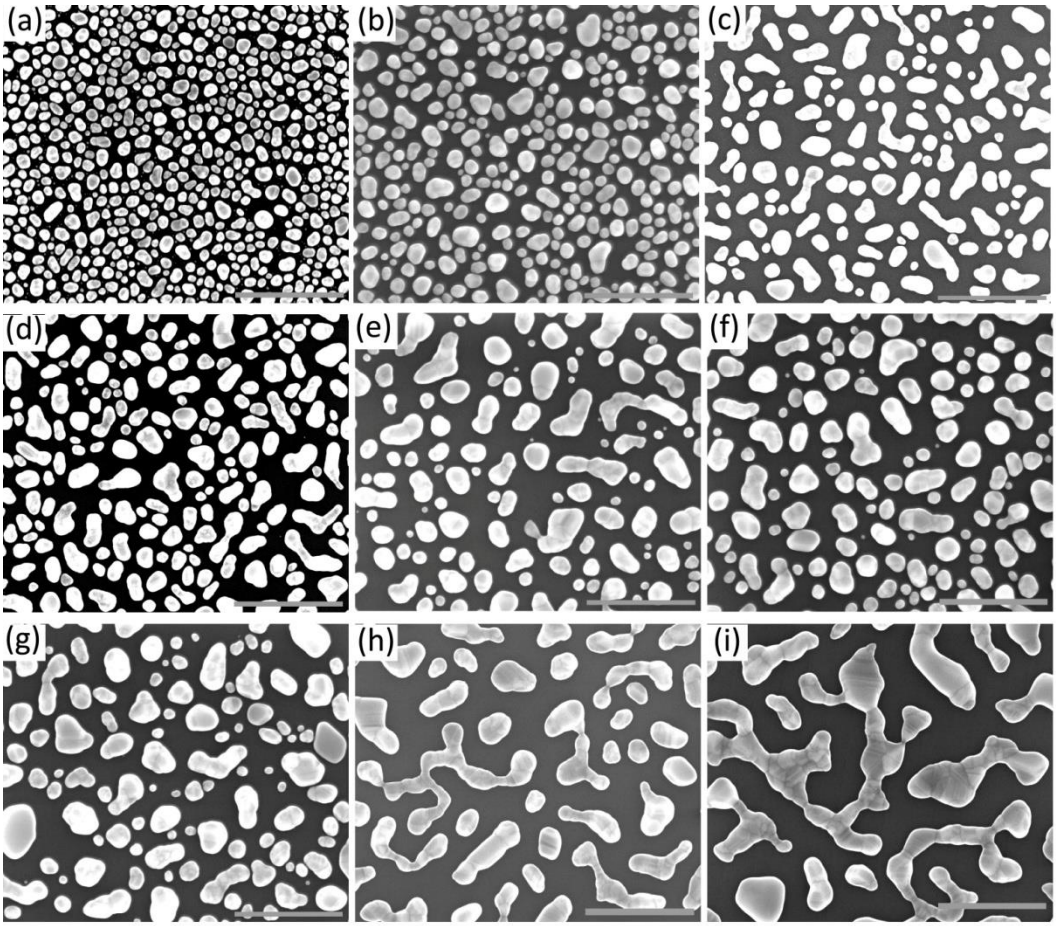

Figure 6.5: SEM images showing the surface of various thicknesses of Ag film deposited on 5 nm TiO_2 layer followed by 200 ℃ annealing in nitrogen for 50 minutes. From (a) to (i), the Ag thickness is 12.2, 14.1, 15.3, 16.0, 17.5, 18.0, 18.4, 19.0, and 19.6 nm, respectively. All the scale bars are 500 nm.

Therefore, TiO_2 films with three different thicknesses (5, 10, 20 nm) were deposited on GaAs by both ALD and sputtering deposition in two batches, followed by 14 nm silver film deposition and annealing at the same condition as above. It is found that both ALD and sputtering techniques could produce high quality TiO_2 layer with smooth surface that is required for the formation of Ag nanoparticles. In order to fabricate silver particles with average

diameter of about 120 nm, which is the optimum value for light trapping based on our theoretical calculation, silver films with nine different thicknesses (from 12.2 to 19.6 nm) were evaporated on 5 nm TiO_2 layer. Nanoparticles were formed after annealing with various size distributions, as shown by the SEM images presented in Figure 6.5. It is clear that the average size of nanoparticles becomes larger when a thicker silver layer is deposited. However, beyond a certain thickness (~19.6 nm), most of the particles are interconnected with each other, indicating that this may be the thickness limit for effective nanoparticle formation.

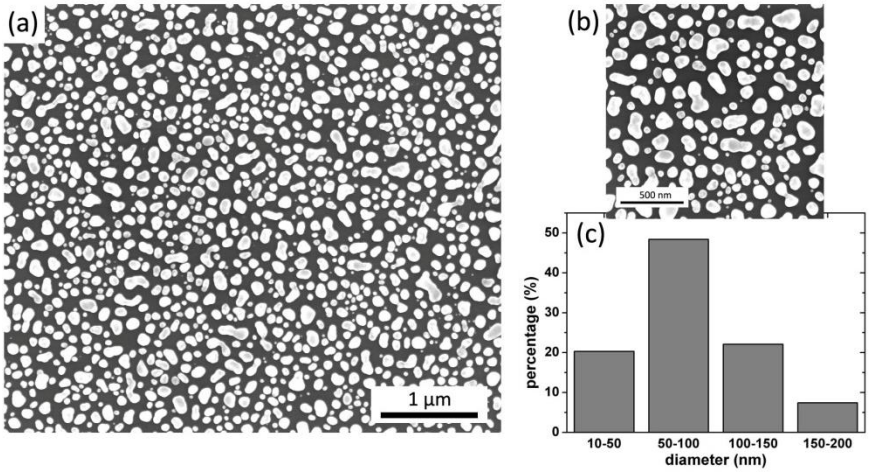

Figure 6.6: SEM images of the Ag nanoparticles formed on the rear of the solar cells (a) and (b) and their size distribution (c).

By measuring the diameters from an ensemble of Ag particles formed from different film thicknesses, 18.0 nm is the optimal Ag film thickness to obtain the particles with average size of ~120 nm. Figures 6.6 (a) and (b) are the SEM images of nanoparticles formed from 18.0 nm Ag at different magnifications. The nanoparticles also show some degree of size dispersion, as can be seen in Figure 6.6 (c). This size distribution is unavoidable due to the method used to fabricate the nanoparticles. Nevertheless, to some extent the size distribution covers WL and QDs wavelength region which in fact could be an advantage.

Figure 6.7 shows the experimental schematic of our plasmonic QDSC devices, with the 10-layer QD p-i-n InGaAs/GaAs QDSC structure deposited with a thin TiO_2 film and Ag nanoparticles on the rear surface. 850 μm diameter circular devices were fabricated by depositing of both n- and p-type contacts on the top side of the wafer as explained in Chapter 2. After metallization of contacts, 100 nm of heavily p-doped GaAs layer on the

illuminated surface of the solar cell was etched away to reduce absorption and surface recombination. Following device fabrication, the rear side of the wafers were mechanically fine polished and coated with TiO_2 layer using atomic layer deposition technique. Based on the Ag nanoparticle growth optimization, three QDSC devices were deposited with 5, 10 and 20 nm thick TiO_2 layers respectively, followed by the deposition of 18 nm thick Ag film and subsequently annealed. These QDSC samples were then characterized for spectral response and I-V characteristics.

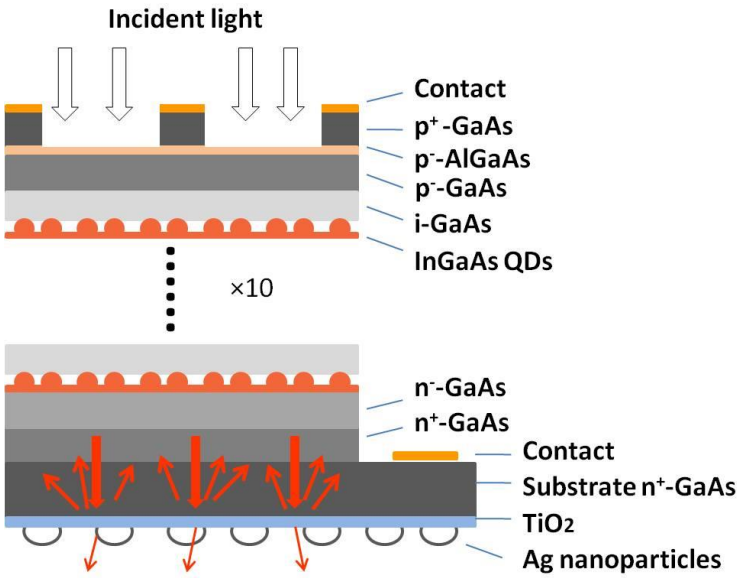

Figure 6.7: The schematic of the p-i-n QDSC with the TiO_2 film and Ag plasmonic nanoparticles on the rear surface.

6.4 Device characterization of plasmonic QD solar cells

The spectral response of a reference QDSC and the plasmonic QDSCs are shown in Figure 6.8. The response signal of the cells is normalized to the peak response at a position around 850 nm. The photocurrent from the short wavelength region up to ~870 nm is due to the absorption in the bulk GaAs layers. Due to strong absorption in bulk GaAs, light with energy greater than the bandgap of GaAs is almost completely absorbed in a first single pass through the cell, and does not interact with the nanoparticles on the rear of the cell. All the solar cell structures investigated here have shown similar GaAs photoresponse signal and further normalizing of the photocurrent response of different cells to their GaAs photoresponse allows us to compare the QD response from different plasmonic configurations. An obvious observation is

that the spectral responses from the wetting layer and the QDs are all enhanced by using plasmonic structures.

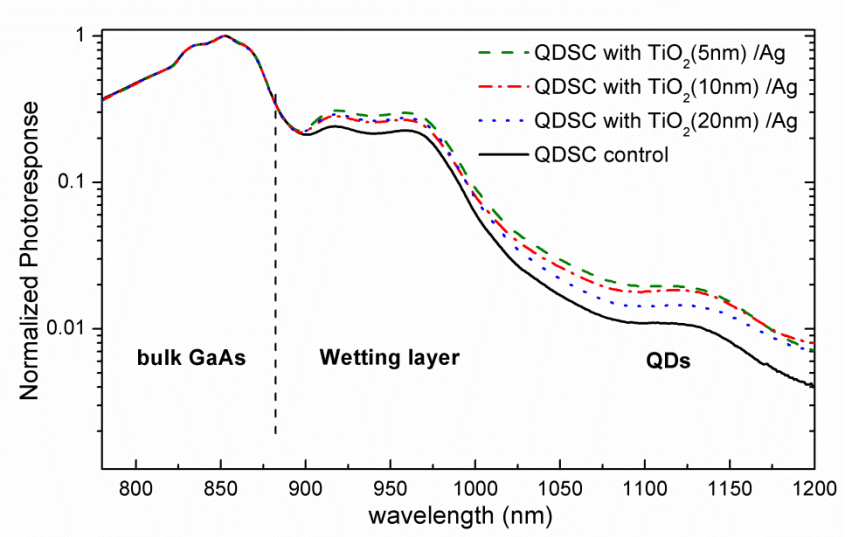

Figure 6.8: Normalized photocurrent spectral response of the reference and QDSCs with Ag plasmonic nanoparticles and different TiO_2 spacer layer thickness. The photoresponse of the cells is normalized at the GaAs wavelength region.

Consistent with the simulation results in Figure 6.3 that show increased scattering cross-section (the resonance peak is also closer to the bandgap of WL and QDs) and better coupling of scattered light into the substrate for the 5nm TiO_2 layer configuration, the experimental results in Figure 6.8 also show highest enhancement over the 900- 1200 nm range for the QDSC with plasmonic structure consisting of 5 nm TiO_2 layer and 120 nm Ag nanoparticles.

1-sun AM1.5G I-V characteristics were also measured for the QD solar cells using the Newport Oriel solar simulator. Note that measurements on the same cell were conducted just prior to the deposition of TiO_2 and nanoparticles, to ensure that any variation in J_{sc} and V_{oc} is entirely due to the surface plasmonic effects and not due to the variation between different devices across the wafer. The I-V curves of QDSC with and without 5 nm TiO_2/Ag nanoparticles structure are plotted in Figure 6.9. Compared to the control QD cell, the plasmonic device shows improved photocurrent over the whole voltage range, with a slight increase in V_{oc}.

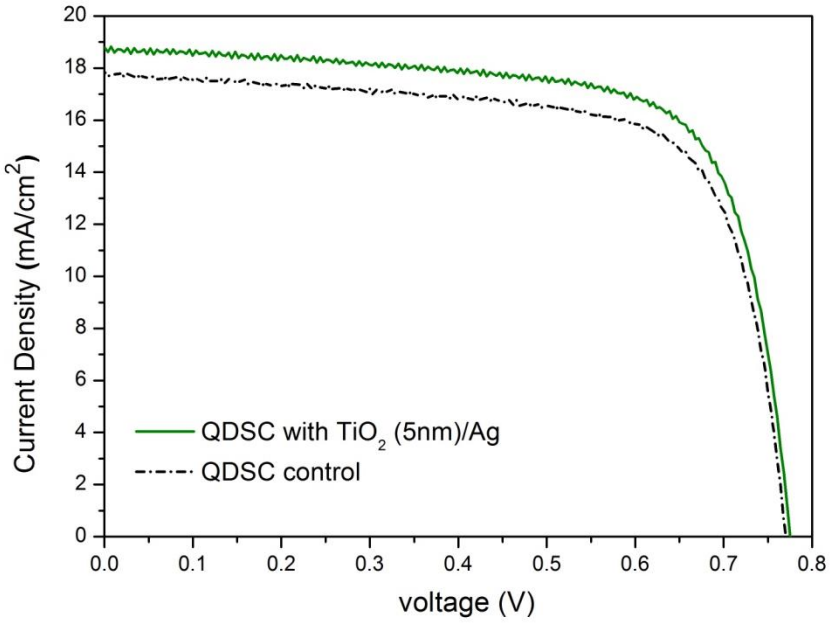

Figure 6.9: I-V characteristics of the same QDSC before and after TiO_2 (5 nm)/Ag (120 nm) nanoparticles deposition measured under AM 1.5 1-sun illumination.

Table 6.1 lists the J_{sc}, V_{oc}, conversion efficiency and their corresponding enhancement obtained from the QDSCs before and after deposition of the plasmonic structures with three different thickness of the TiO_2 layer. All three configurations provide improved solar cell performance, with the best result obtained from 5 nm TiO_2 layer structure. This plasmonic configuration results in 5.3 % enhancement of J_{sc} and 0.9 % enhancement of V_{oc} with respect to the reference QD cell, leading to an overall efficiency (η) enhancement of 7.6%. The improvement in the plasmonic solar cells is due to the enhanced absorption (and hence photoresponse, as shown in Figure 6.8) in the WL and QD regions. Unlike the other alternative approaches to increasing the absorption of long wavelength light, such as increasing the number of QD layers [3, 4] or QD/barrier doping [1, 2] which showed inconsistent influence on V_{oc} due to possible variation in dot properties in different QDSC structures, our plasmonic solar cells all exhibit an increase in both V_{oc} and J_{sc}. This is consistent with the enhancement predicted using the measured J_{sc} enhancement and the diode Equation (6.1). The simultaneous enhancement in both J_{sc} and V_{oc} observed here is significant and essential for obtaining high efficiency QDSC.

Table 6.1: Device performance parameters for the QD solar cells with different spacer (TiO_2) thickness, before (underlined numbers in italics) and after deposition of the plasmonic nanoparticles.

	J_{sc} (mA/cm^2)	J_{sc} enhancement	V_{oc} (V)	V_{oc} enhancement	Efficiency η (%)	η enhancement
5 nm spacer	***17.76*** 18.70	5.3%	***0.769*** 0.776	0.9%	***9.82*** 10.58	7.6%
10 nm spacer	***17.83*** 18.65	4.6%	***0.756*** 0.762	0.8%	***9.69*** 10.26	5.9%
20 nm spacer	***17.52*** 18.15	3.6%	***0.772*** 0.780	1.0%	***10.01*** 10.42	4.1%

An equation for V_{oc} is obtained by setting the solar cell net current to zero:

$$V_{OC} = {}^{nkT}/_{q} \ln\left({}^{J_{sc}}/_{J_0} + 1\right) \quad (6.1)$$

where J_0 is the saturation current of the device, q is the elementary charge 1.6×10^{-19} Coulombs, k is the Boltzmann constant of value 1.38×10^{-23} J/K, T is the cell temperature in Kelvin.

The optical path length enhancement, namely the ratio of the average distance travelled by weakly absorbed light in a solar cell with light trapping to the distance travelled in a planar solar cell without light trapping is often a good indicator for the effectiveness of the light trapping strategy. In this chapter, the optical path length enhancement of long wavelength light due to scattering by silver plasmonic structures is estimated from the photocurrent enhancement (Figure 6.8) using the exponential absorption relationship during light propagation. At 1000 nm, the path length enhancement is about 2.1 for the 5 nm TiO_2/Ag plasmonic QDSC studied in the thesis. The estimated path length enhancement is much lower than the ideal enhancement of $4n^2$ (where n is the refractive index of absorbing layer, i.e., n= 3.5 for GaAs at around 1000 nm) that is often used as a good benchmark for light trapping using perfectly randomized surfaces [38]. Theoretically, a path length enhancement of 2 is expected by using a perfect reflector behind the solar cell. To evaluate the practical effects of plasmonic light trapping in our solar cells, we measured the photoresponse from a reference solar cell with a thick Ag back reflector. As plotted in Figure 6.10, the enhancement due to the back reflector is very small, which is much smaller than the effect due to the plasmonic structure. This means that the TiO_2/Ag plasmonic structures indeed provide an

effective light trapping strategy in the QDSC, and the low path length enhancement factor could be caused by losses of the studied system such as free-carrier absorption.

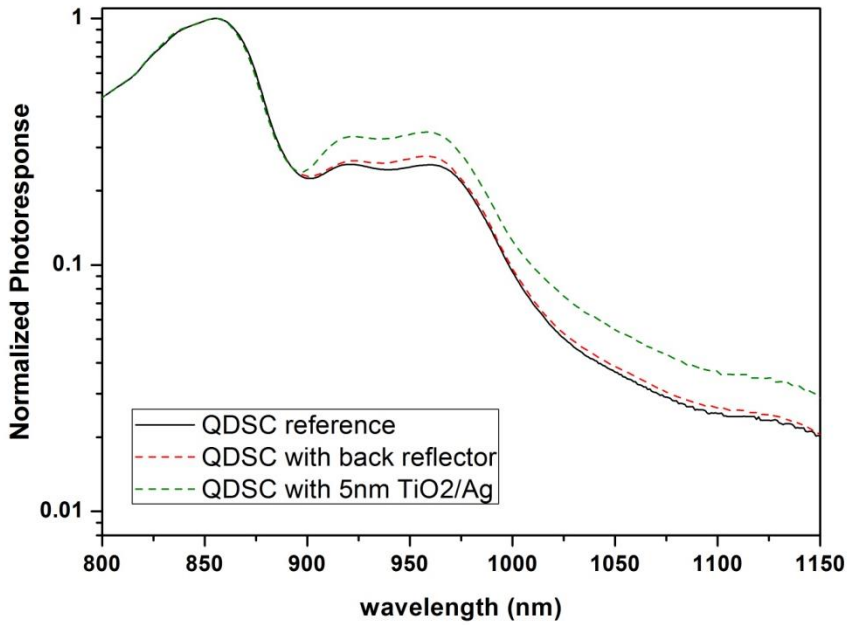

Figure 6.10: Normalized photoresponse of the reference QDSC, QDSC with a back reflector and QDSC with the plasmonic structure.

6.5 Strategy for further improvement of the plasmonic QDSC performance

Since our QD solar cells were grown on heavily n-doped GaAs substrates, it is highly likely that free carrier absorption in the substrates will result in parasitic losses and thus negate some of the benefits produced by the light trapping effect. In order to further verify this, we measured and compared the photoresponses from the reference QD solar cell under both front and rear side illumination configurations. The inset in figure 6.11 illustrates the schematic of the experimental set-up and the photoresponse spectra of the solar cell under two illumination configurations. Different from the case of the front illumination, the GaAs induced photocurrent could not be observed for back illumination due to the complete absorption in GaAs substrate which does not contribute to the solar cell junction region. There is also a significant difference in the photoresponse from the WL/QD region between the front and rear illuminations and this clearly indicates the significant free carrier absorption in the n^+ GaAs substrate.

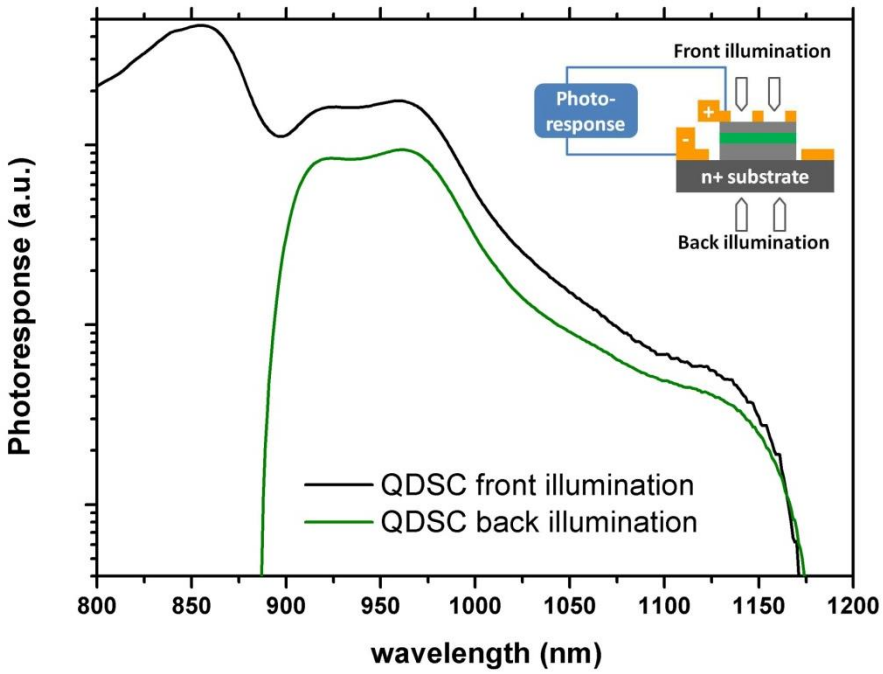

Figure 6.11: Photoresponse of the reference QDSC under front and rear illumination. The inset shows the illumination configuration.

For the front illumination configuration, light is incident on the WL/QD region first before reaching and passing through the substrate. However for rear illumination, light is attenuated by the free-carrier absorption first in the substrate, before it reaches the WL/QD region, leading to reduction in the photoresponse of the WL/QD spectral range. Note that the absorption for wavelength below 875nm is due to the normal band-edge absorption, rather than free carrier absorption. Previous studies [39] have reported significant free carrier absorption in GaAs at ~1000 nm when the dopant density is above $1x10^{18}$ cm^{-3}. Therefore it is highly possible that free carrier absorption may be responsible for the lower optical path length enhancements observed in our devices (for both with a rear reflector or the plasmonic structure) than the theoretically expected value. It has been shown in Ref. [39] that the free-carrier absorption coefficient of the semi-insulating GaAs substrate is about 2 orders of magnitude lower than that of n^+ substrate in the wavelength range around 1 μm. Hence, it can be expected that growing the same QD solar cell structures on semi-insulating substrates will significantly reduce the effect of free carrier absorption and further enhance the light trapping effect of the plasmonic structures.

The main reason that leads to V_{oc} degradation of QDSC compared to reference cell is the lowering of forward injection thermal activation energy (E_a) as reported before [40]. Since E_a will not be affected by Ag nanoparticles

deposition, by using plasmonic structure for light trapping, we are thus able to simultaneously achieve enhancement of J_{sc} and an increase of V_{oc} in In(Ga)As/GaAs QDSC.

6.6 Conclusions

In summary, we have demonstrated an increased IR photoresponse of QD solar cells by incorporating plasmonic nanoparticles on the rear side of the solar cell for trapping long wavelength light in the QD/WL absorbing layer. Contrary to the other aforementioned approaches for enhancing QD absorption, this approach does not reduce V_{oc} of the solar cell compared to the reference structure. We demonstrate simultaneous increase in J_{sc} and V_{oc} of up to 5.3 % and 0.9 %, respectively, with respect to the reference QD solar cell. A corresponding overall efficiency enhancement of 7.6 % is achieved.

However, the path length enhancement measured in this study is limited by free carrier absorption in the n^+ doped GaAs substrate. It has been shown in Ref. [39] that the absorption coefficient of the semi-insulating GaAs substrate is about 2 orders of magnitude lower than that of n^+ substrate. Hence, growing the same QD solar cell structures on semi-insulating substrates should significantly reduce the effect of free carrier absorption. It is expected that the short circuit current density and the efficiency of the quantum dot solar cell would be increased further based on the same surface plasmonic strategy studied in the thesis when the same QDSC with an n^+-doped bottom contact layer is grown on semi-insulating substrate.

In addition, the absorption enhancement mechanism studied here can be a potential approach to improve the inter-subband transitions for other quantum structures based III-V photovoltaic devices or photodetectors. For example, for quantum well/dot infrared photodetectors due to the polarisation selection rule for inter-subband transitions (growth direction TM mode polarized intersubband transitions) they are insensitive to normal incidence illumination which does not have any polarisation component along the growth direction, leading to a weak IR region response [41]. The random scattering induced by plasmonic light trapping scheme proposed by our study may lead to enhanced inter-subband absorption and thus better device performances.

References

[1] Morioka, T., R. Oshima, A. Takata, Y. Shoji, T. Inoue, T. Kita, and Y. Okada. Multi-stacked InAs/GaNAs quantum dots with direct Si doping for use in intermediate band solar cell in *Conference Record of the 35th IEEE Photovoltaic Specialists Conference*. 2010. New York: IEEE.

[2] Sablon, K.A., J.W. Little, V. Mitin, A. Sergeev, N. Vagidov, and K. Reinhardt, Strong Enhancement of Solar Cell Efficiency Due to Quantum Dots with Built-In Charge. *Nano Letters*, 2011. **11**(6): pp. 2311-2317.

[3] Hubbard, S.M., C. Plourde, Z. Bittner, C.G. Bailey, M. Harris, T. Bald, M. Bennett, D.V. Forbes, and R. Raffaelle. InAs quantum dot enhancement of GaAs solar cells. in *Conference Record of the 35th IEEE Photovoltaic Specialists Conference*. 2010. New York: Ieee.

[4] Takata, A., R. Oshima, Y. Shoji, K. Akahane, and Y. Okada. Fabrication of 100 Layer-Stacked InAs/GaNAs Strain-Compensated Quantum Dots on GaAs (001) for Application to Intermediate Band Solar Cell. in *Conference Record of the 35th IEEE Photovoltaic Specialists Conference*. 2010. New York: IEEE.

[5] Bailey, C.G., D.V. Forbes, R.P. Raffaelle, and S.M. Hubbard, Near 1 V open circuit voltage InAs/GaAs quantum dot solar cells. *Applied Physics Letters*, 2011. **98**(16): pp. 163105-3.

[6] Guimard, D., R. Morihara, D. Bordel, K. Tanabe, Y. Wakayama, M. Nishioka, and Y. Arakawa, Fabrication of InAs/GaAs quantum dot solar cells with enhanced photocurrent and without degradation of open circuit voltage. *Applied Physics Letters*, 2010. **96**(20): pp. 203507.

[7] W. Koch, A.L.E., D. Franke, C. Habler, J. P. Kalejs, H. J. Moller, Bulk Crystal Growth and Wafering for PV in Handbook of Photovoltaic Science and Engineering. 2003: John Wiley & Sons.

[8] Carlson, D.E. and C.R. Wronski, Amorphous silicon solar cell. *Applied Physics Letters*, 1976. **28**(11): pp. 671-673.

[9] Contreras, M.A., B. Egaas, K. Ramanathan, J. Hiltner, A. Swartzlander, F. Hasoon, and R. Noufi, Progress toward 20% efficiency in Cu(In,Ga)Se2 polycrystalline thin-film solar cells. *Progress in Photovoltaics: Research and Applications*, 1999. **7**(4): pp. 311-316.

[10] Bloss, W.H., F. Pfisterer, M. Schubert, and T. Walter, Thin-film solar cells. *Progress in Photovoltaics: Research and Applications*, 1995. **3**(1): pp. 3-24.

[11] Aberle, A.G., Thin-film solar cells. *Thin Solid Films*, 2009. **517**(17): pp. 4706-4710.

[12] Rand, B.P., P. Peumans, and S.R. Forrest, Long-range absorption enhancement in organic tandem thin-film solar cells containing silver nanoclusters. *Journal of Applied Physics*, 2004. **96**(12): pp. 7519-7526.

[13] Catchpole, K.R. and A. Polman, Plasmonic solar cells. *Optics Express*, 2008. **16**(26): pp. 21793-21800.

[14] Stuart, H.R. and D.G. Hall, Thermodynamic limit to light trapping in thin planar structures. *Journal of the Optical Society of America a-Optics Image Science and Vision*, 1997. **14**(11): pp. 3001-3008.

[15] Yablonovitch, E. and G.D. Cody, Intensity Enhancement in Textured Optical Sheets for Solar-Cells. *Ieee Transactions on Electron Devices*, 1982. **29**(2): pp. 300-305.

[16] Green, M.A., Limits on the Open-Circuit Voltage and Efficiency of Silicon Solar-Cells Imposed by Intrinsic Auger Processes. *Ieee Transactions on Electron Devices*, 1984. **31**(5): pp. 671-678.

[17] Maier, S., Plasmonics: Fundamentals and Applications. 2007, New York: Springer.

[18] Atwater, H.A. and A. Polman, Plasmonics for improved photovoltaic devices. *Nat Mater*, 2010. **9**(3): pp. 205-213.

[19] Ferry, V.E., J.N. Munday, and H.A. Atwater, Design Considerations for Plasmonic Photovoltaics. *Advanced Materials*, 2010. **22**(43): pp. 4794-4808.

[20] Saeta, P.N., V.E. Ferry, D. Pacifici, J.N. Munday, and H.A. Atwater, How much can guided modes enhance absorption in thin solar cells, *Optics Express*, 2009. **17**(23): pp. 20975-20990.

[21] Stuart, H.R. and D.G. Hall, Absorption enhancement in silicon-on-insulator waveguides using metal island films. *Applied Physics Letters*, 1996. **69**(16): pp. 2327-2329.

[22] Nakayama, K., K. Tanabe, and H.A. Atwater, Plasmonic nanoparticle enhanced light absorption in GaAs solar cells. *Applied Physics Letters*, 2008. **93**(12): pp. 121904.

[23] Laghumavarapu, R.B., A. Moscho, A. Khoshakhlagh, M. El-Emawy, L.F. Lester, and D.L. Huffaker, GaSb/GaAs type II quantum dot solar cells for enhanced infrared spectral response. *Applied Physics Letters*, 2007. **90**(17): pp. 173125-3.

[24] Lu, H.F., L. Fu, J. Greg, T. Hark Hoe, T. Sudersena Rao, and J. Chennupati, Temperature dependence of dark current properties of InGaAs/GaAs quantum dot solar cells. *Applied Physics Letters*, 2011. **98**(18): pp. 183509.

[25] Yoshitaka, O., O. Ryuji, and T. Ayami, Characteristics of InAs/GaNAs strain-compensated quantum dot solar cell. *Journal of Applied Physics*, 2009. **106**(2): pp. 024306.

[26] Jolley, G., H.F. Lu, L. Fu, H.H. Tan, and C. Jagadish, Electron-hole recombination properties of In0.5Ga0.5As/GaAs quantum dot solar cells and the influence on the open circuit voltage. *Applied Physics Letters*, 2010. **97**(12): pp. 123505.

[27] Turner, S., S. Mokkapati, G. Jolley, L. Fu, H.H. Tan, and C. Jagadish, Periodic dielectric structures for light-trapping in InGaAs/GaAs quantum well solar cells. *Optics Express*, 2013. **21**(9): pp. A324-A335.

[28] Beck, F.J., S. Mokkapati, A. Polman, and K.R. Catchpole, Asymmetry in photocurrent enhancement by plasmonic nanoparticle arrays located on the front or on the rear of solar cells. *Applied Physics Letters*, 2010. **96**(3): pp. 033113.

[29] Beck, F.J., A. Polman, and K.R. Catchpole, Tunable light trapping for solar cells using localized surface plasmons. *Journal of Applied Physics*, 2009. **105**(11): pp. 114310.

[30] Catchpole, K.R. and A. Polman, Design principles for particle plasmon enhanced solar cells. *Applied Physics Letters*, 2008. **93**(19): pp. 191113.

[31] Lim, S.H., W. Mar, P. Matheu, D. Derkacs, and E.T. Yu, Photocurrent spectroscopy of optical absorption enhancement in silicon photodiodes via scattering from surface plasmon polaritons in gold nanoparticles. *Journal of Applied Physics*, 2007. **101**(10): pp. 104309.

[32] Lu, H.F., S. Mokkapati, L. Fu, G. Jolley, H.H. Tan, and C. Jagadish, Plasmonic quantum dot solar cells for enhanced infrared response. *Applied Physics Letters*, 2012. **100**(10): pp. 103505.

[33] Langhammer, C., M. Schwind, B. Kasemo, and I. Zorić, Localized Surface Plasmon Resonances in Aluminum Nanodisks. *Nano Letters*, 2008. **8**(5): pp. 1461-1471.

[34] Lumerical. FDTD Solutions. Available from: http://www.lumerical.com/tcad-products/fdtd/.

[35] Xu, G., M. Tazawa, P. Jin, S. Nakao, and K. Yoshimura, Wavelength tuning of surface plasmon resonance using dielectric layers on silver island films. *Applied Physics Letters*, 2003. **82**(22): pp. 3811.

[36] Mertens, H., J. Verhoeven, A. Polman, and F.D. Tichelaar, Infrared surface plasmons in two-dimensional silver nanoparticle arrays in silicon. *Applied Physics Letters*, 2004. **85**(8): pp. 1317-1319.

[37] Meier, M. and A. Wokaun, Enhanced fields on large metal particles: dynamic depolarization. *Opt. Lett.*, 1983. **8**(11): pp. 581-583.

[38] Yablonovitch, E., Statistical ray optics. *J. Opt. Soc. Am.*, 1982. **72**(7): pp. 899-907.

[39] Spitzer, W.G. and J.M. Whelan, Infrared Absorption and Electron Effective Mass in n-Type Gallium Arsenide. *Physical Review*, 1959. **114**(1): pp. 59-63.

[40] Jolley, G., H.F. Lu, L. Fu, H.H. Tan, and C. Jagadish, Electron-hole recombination properties of In0.5Ga0.5As/GaAs quantum dot solar cells and the influence on the open circuit voltage. *Applied Physics Letters*, 2010. **97**(12): pp. 123505.

[41] Adawi, A.M., E.A. Zibik, L.R. Wilson, A. Lemaitre, W.D. Sheng, J.W. Cockburn, M.S. Skolnick, J.P. Leburton, M. Hopkinson, G. Hill, S.L. Liew, and A.G. Cullis, Observation of in-plane polarized intersublevel absorption in strongly coupled InGaAs/GaAs self assembled quantum dots. *Physica Status Solidi B-Basic Solid State Physics*, 2003. **238**(2): pp. 341-344.

Chapter 7

Conclusions and future work

7.1 Conclusions

In this thesis, we have successfully demonstrated the growth and fabrication of $In_{0.5}Ga_{0.5}As$/GaAs quantum dot solar cells, and proposed several new approaches to enhance solar cell performance. We have performed the systematic investigation on:

(1) The growth and fabrication of 10-layer QDSC, optimizing the MOCVD growth conditions and revealing the fundamental properties of QDSCs. Enhanced photocurrent is achieved for QDSC with respect to the reference device without a quantum dot structure.

(2) The effect of varied QD stacking number (10, 15 and 20 layers) on QDSCs performance. It was found that with the increase of stacking number, the light absorption in the QD structures is increased however with degraded photocurrent and efficiency, because of the larger recombination and less efficient carrier extraction in the higher QD stacked layer devices.

(3) The influence of n-type Si modulation doping on QDSC performance. Up to 28.20 % efficiency enhancement is achieved in modulation doped solar cell with respect to the undoped QDSC device.

(4) The effect of post-growth rapid thermal annealing on QDSCs with different number of QD layers. QD solar cell performance can be improved by post thermal annealing, but the stacking number of QDs should be properly controlled.

(5) The Ag nanoparticles enhanced plasmonic effect on QDSCs. We demonstrate both theoretically and experimentally that increased IR photoresponse of QD solar cells by incorporating plasmonic nanoparticles on the rear surface of the device for effectively trapping of long wavelength light. Simultaneous increase in J_{sc} and V_{oc} are obtained compared to the reference structure, with a corresponding efficiency enhancement of 7.6%.

In the first two chapters, the concepts and mechanisms on III-V semiconductor based solar cells and quantum dots enhanced devices were introduced and then the corresponding detailed experimental techniques were described.

In **Chapter 3**, metal organic chemical vapour deposition (MOCVD) growth of $In_{0.5}Ga_{0.5}As$/GaAs QDs has been optimized by controlling several

key growth parameters. Nucleation time and deposition temperature were optimised to obtain high density QDs which exhibit good optoelectronic properties for further solar cell device applications. It was found that a fast growth rate was required to create a high density of quantum dots, and the quantum dot density was found to saturate at 6.0- 6.4 monolayer of InGaAs material. It was also found that a growth temperature of 550 ℃ was sufficient to limit the clustering of the dots while maintaining high quality. The solar cells containing a p-i-n structure were grown with and without the incorporation of 10-layer QDs, and subsequently fabricated into solar cell devices. Although QDSC exhibited short-circuit current density (J_{sc}) of 18.8 mA/cm^2 and efficiency of 11.1 % [1], the open-circuit voltage (V_{oc}) was reduced compared to the control cell as widely reported in various QD systems [2-4]. The QD devices showed complicated dark I-V behaviours compared to the control device without QD layers due to temperature and bias dependent carrier capture, occupation and recombination processes. The analysis of temperature dependent dark I-V results revealed the unique characteristics for QDSC [1]. In addition, the two-photon excitation process has also been proven by the inter-subband photoresponse detected at low temperatures under blackbody excitation [5].

Due to the increase in the wetting layer/QDs sub-bandgap absorption of near infrared radiation, extended photoresponse and increased J_{sc} have been obtained for QDSC compared to GaAs reference cell [1]. However, the contribution from QDs was limited by their small volume and thus the low absorption cross-section. Stacking more QD layers is supposed to enhance the total QD volume and hence absorption. Hence we carried out experiments to grow QDSC structures with increased number of QD layers. The QD solar cells with 15 and 20 layers QDs were grown and shown bright room temperature QD/WL photoluminescence compared with 10-layer devices as a result of increased emission volume. However, much reduced photocurrent and conversion efficiency for these two samples were observed, which could be due to two main reasons, (1) the same built-in potential is assumed for all three devices [6], but larger number of QDs layers leads to an increased distance of depletion region and consequently weaker built-in electric field. Photogenerated carriers have to travel across longer distance under the lower electric field to form external circuit photocurrent, with a larger probability to be captured in QDs layers and thus a larger recombination probability. (2) Due to the strain-driven self-organizing process, growth of more QD layers without implementation of strain compensation layers normally result in large strain and thus increased defect density in the quantum dot region, which will also lead to increased carrier recombination. In addition, electroluminescence

(EL) spectra of all three samples were obtained as a function of temperatures as well as injection current levels. By studying the EL of the devices, we further extract useful information of the electronic sub-band structure of various QDSC samples.

Based on Chapter 3, a considerable amount of recombination that takes place in the confined WL and QDs states makes transport and collection of photo-generated carriers inefficient [1, 7-10]. To improve the carrier extraction efficiency and consequently more enhanced photocurrent, intentional modulation doping was introduced into in-between QDs layers to partially populate the QD confined states with carriers, which can then ensure sufficient carriers be excited to the conduction band edge of the host materials and collected to form photocurrent [11-14]. The effect of modulation doping placed within thin space layer on the QDSC performance and its position dependence have not previously been reported. In **Chapter 4**, we investigated the influence of silicon modulation (n-type) doping on the properties and performance of 10-layer $In_{0.5}Ga_{0.5}As$/GaAs QDSC. The modulation doping at the proper position in QDSC effectively improves carrier transport and collection efficiency, leading to an enhancement of the external quantum efficiency (EQE) over the whole solar cell response range. As a result, up to 28.20 % efficiency enhancement from 6.95 % to 8.91 % was achieved in modulation doped device compared to the undoped solar cell.

In addition to the design of different QDSC structures, we have also taken two different post-growth approaches to improve the QDSC efficiency, including rapid thermal annealing and surface plasmonic light trapping.

To modify the device design (especially the electronic structure design) of epitaxially grown quantum dot based devices, normally the size and/or shape of QDs need to be varied through extensive growth optimization since the formation of QDs is highly sensitive to several growth parameters. The approach of post-growth thermal annealing is considered as an attractive method to optimize QD devices performance by adjusting the energy band structures and carrier confinement of quantum wells and QDs [15, 16]. In **Chapter 5**, a standard 10-layer InGaAs/GaAs QDSC was annealed at various temperatures between 700 and 850 ℃ for 50 seconds with a step of 50 ℃. Thermal annealing at high temperatures induced significant blue-shift in the WL and QDs PL peak positions, which can be attributed to decreased confinement depth in both conduction band and valence band for WL and QDs potentials. This was caused by the inter-diffusion of the InGaAs quantum dots/wetting layer with its surrounding GaAs barriers, i.e. In and Ga atomic inter-diffusion. In the meanwhile, the dark current of the annealed devices was

decreased with the increase of the annealing temperature, as a result of reduced defect density and/or lowered QD and WL confinement energy. As a result, the efficiency of 10-layer QDSC annealed at a highest temperature of 850 ℃ displayed the highest increase of 41.42 % from 10.26 % to 14.51 %, compared to the as-grown sample. However, for the more strained QD structures, such as 15, 20-layer samples in our work, partial strain relaxation may have caused the formation of extended defects during the annealing process [15, 17], leading to higher dark current and degraded V_{oc}. The possible dopant diffusion effects from the intentional doping elements (Zn and Si) on device properties due to high temperature annealing were also examined and discussed.

As mentioned earlier, the absorption volume and cross-section of QDs are very small, resulting in inefficient absorption of long wavelength light. In order to absorb higher fraction of incident low energy light, we propose the approach to employ plasmonic enhanced light scattering effect from Ag nanoparticle to trap the weakly absorbed light inside the solar cell and hence to increase the effective optical path lengths for long wavelength light [18]. In **Chapter 6**, finite-difference time-domain simulations were performed to investigate the plasmonic light scattering properties produced by Ag nanoparticles deposited on a dielectric layer, which was able to tune the plasmonic resonance peak position as well as to improve the scattering cross-section and fraction of light coupled into solar cell substrate. It was found that the combination of 120 nm diameter hemispherical Ag nanoparticle with 5 nm thick TiO_2 dielectric film that was pre-deposited on the back of the GaAs substrate was the optimum configuration for our QDSC. Consistent with the simulation results, 120 nm Ag nanoparticle/ 5nm TiO_2 configuration improved the QDSC spectral response by 35.7% over the 900 nm – 1200 nm wavelength range. This plasmonic configuration led to 5.3 % enhancement of J_{sc} and 0.9 % enhancement of V_{oc} compared to the reference QD cell, with an overall efficiency enhancement of 7.6 %. The J_{sc} improvement was due to the enhanced long wavelength absorption in the WL and QD regions. Optical path length enhancement of long wavelength light due to light trapping was estimated from the photocurrent enhancement. At 1000 nm, the path length enhancement is about 2.1 for the best plasmonic configuration studied in the thesis. This enhancement factor is lower than the ideal enhancement of $4n^2$ (n is the refractive index of absorbing layer) that is expected by using perfectly randomizing surfaces [19]. Further improvement of the plasmonic solar cell performance may be achieved by implementing the device structure on semi-insulating substrates to avoid the serious free-carrier absorption in the n^+ GaAs substrate.

In summary, $In_{0.5}Ga_{0.5}As$/GaAs QDSCs which exhibit good performance were grown and fabricated. The properties and fundamental mechanisms behind their complicated photoelectrical behaviours were understood. Several approaches were proposed and carried out to improve the performance of QDSCs, either during the epitaxial growth process or after the growth and fabrication of the solar cells, leading to enhanced photoresponse and overall efficiency of QDSCs.

7.2 Future work

In this thesis, a major challenge for QD solar cell growth was the strain accumulation when a large number of QD layers were stacked. While incorporation of strain compensation layer such as GaP was also attempted to decrease the total strain within the QD layers during this project, the initial experimental results were not very encouraging, indicating that further study and development of the strain balance effect of GaP based layer on QD structure are necessary [20, 21]. It would be worth changing the position, and growth condition of GaP to confirm the best location in the active region. Alternatively, the use of ternary alloy $GaAs_xP_{1-x}$ instead of GaP may provide better compensation than the highly strained GaP, which is critical to increasing the total volume and absorption of QDs/WL. Also, the background doping of MOCVD grown material greatly affects the built-in electric field. More study may be required to understand and thus reduce background doping effect, such that the high electric field can be maintained for efficient carrier extraction in QDSCs with large stacked number of QD layers.

It has been shown in Ref. [22] that the absorption coefficient of the semi-insulating GaAs substrate is about 2 orders of magnitude lower than that of n^+ substrate. Hence, growing the same QD solar cell structures on semi-insulating substrates would significantly reduce the effect of free carrier absorption. It is expected that the short circuit current density and the efficiency of the quantum dot solar cell would be increased further based on the same surface plasmonic strategy studied in the thesis when the QDSCs are grown on the semi-insulating substrate.

Except for plasmonic structure, wavelength-scale diffraction gratings can be also used to couple incoming light into diffraction orders outside the escape cone in the solar cell [23]. Although compared to plasmonic approach investigated in this work, wavelength-scale dielectric gratings may require a lot more process optimization, they do have the advantage of no parasitic losses (e.g. light absorption) inherent to metallic nanoparticles, and are

considered to be a good alternative for light trapping applications in thin film solar cells application.

Furthermore, another method to eliminate parasitic losses from the substrate is epitaxial lift-off, by which the epitaxially grown thin film active layers can be lifted from the substrate and supported on an inexpensive substrate with light trapping strategies on it [24, 25]. This approach would allow the expensive substrates such as GaAs to be re-used to reduce the total cost of the QDSCs, and make it possible to fabricate large-scale light trapping structures on alternative substrates. This strategy could be a worthwhile subject for future investigation.

References

[1] Lu, H.F., L. Fu, J. Greg, T. Hark Hoe, T. Sudersena Rao, and J. Chennupati, Temperature dependence of dark current properties of InGaAs/GaAs quantum dot solar cells. *Applied Physics Letters*, 2011. **98**(18): pp. 183509.

[2] Hubbard, S.M., C.D. Cress, C.G. Bailey, R.P. Raffaelle, S.G. Bailey, and D.M. Wilt, Effect of strain compensation on quantum dot enhanced GaAs solar cells. *Applied Physics Letters*, 2008. **92**(12): pp. 123512.

[3] Popescu, V., G. Bester, M.C. Hanna, A.G. Norman, and A. Zunger, Theoretical and experimental examination of the intermediate-band concept for strain-balanced (In,Ga)As/Ga(As,P) quantum dot solar cells. *Physical Review B*, 2008. **78**(20): pp. 17.

[4] Okada, Y., R. Oshima, and A. Takata, Characteristics of InAs/GaNAs strain-compensated quantum dot solar cell. *Journal of Applied Physics*, 2009. **106**(2): pp. 024306.

[5] Jolley, G., L. Fu, H.F. Lu, H.H. Tan, and C. Jagadish, The role of intersubband optical transitions on the electrical properties of InGaAs/GaAs quantum dot solar cells. *Progress in Photovoltaics: Research and Applications*, 2013. **21**(4): pp. 736-746.

[6] Jolley, G., H.F. Lu, L. Fu, H.H. Tan, and C. Jagadish, Electron-hole recombination properties of In0.5Ga0.5As/GaAs quantum dot solar cells and the influence on the open circuit voltage. *Applied Physics Letters*, 2010. **97**(12): pp. 123505.

[7] Marcinkevicius, S. and R. Leon, Carrier capture and relaxation in quantum dot structures with different dot densities. *Microelectronic Engineering*, 2000. **51-2**: pp. 79-83.

[8] Brasken, M., M. Lindberg, M. Sopanen, H. Lipsanen, and J. Tulkki, Temperature dependence of carrier relaxation in strain-induced quantum dots. *Physical Review B*, 1998. **58**(24): pp. 15993-15996.

[9] Adler, F., M. Geiger, A. Bauknecht, F. Scholz, H. Schweizer, M.H. Pilkuhn, B. Ohnesorge, and A. Forchel, Optical transitions and carrier relaxation in self assembled InAs/GaAs quantum dots. *Journal of Applied Physics*, 1996. **80**(7): pp. 4019-4026.

[10] Ohnesorge, B., M. Albrecht, J. Oshinowo, A. Forchel, and Y. Arakawa, Rapid carrier relaxation in self-assembled InxGa1-xAs/GaAs quantum dots. *Physical Review B*, 1996. **54**(16): pp. 11532-11538.

[11] Marti, A., N. Lopez, E. Antolin, E. Canovas, C. Stanley, C. Farmer, L. Cuadra, and A. Luque. Novel semiconductor solar cell structures: The quantum dot intermediate band solar cell. in *Symposium on Thin Film and Nanostructured Materials for Photovoltaics held at the 2005 EMRS Meeting*. 2005. Strasbourg, FRANCE: Elsevier Science Sa.

[12] Sablon, K.A., J.W. Little, V. Mitin, A. Sergeev, N. Vagidov, and K. Reinhardt, Strong Enhancement of Solar Cell Efficiency Due to Quantum Dots with Built-In Charge. *Nano Letters*, 2011. **11**(6): pp. 2311-2317.

[13] Schneider, C., S. Kremling, N.V. Tarakina, T. Braun, M. Adams, M. Lermer, S. Reitzenstein, L. Worschech, M. Kamp, S. Hofling, and A. Forchel, AlGaInAs quantum dot solar cells: tailoring quantum dots for intermediate band formation. *Semiconductor Science and Technology*, 2012. **27**(3).

[14] Marcinkevicius, S., J. Siegert, and Q.X. Zhao, Carrier spin dynamics in modulation-doped InAs/GaAs quantum dots. *Journal of Applied Physics*, 2006. **100**(5): pp. 054310.

[15] Fu, L., H.H. Tan, I. McKerracher, J. Wong-Leung, C. Jagadish, N. Vukmirovic, and P. Harrison, Effects of rapid thermal annealing on device characteristics of InGaAs/GaAs quantum dot infrared photodetectors. *Journal of Applied Physics*, 2006. **99**(11): pp. 114517.

[16] Jolley, G., L. Fu, H.H. Tan, and C. Jagadish, Effects of annealing on the spectral response and dark current of quantum dot infrared photodetectors. *Journal of Physics D-Applied Physics*, 2008. **41**(21): pp. 215101.

[17] Stewart, K., M. Buda, J. Wong-Leung, L. Fu, C. Jagadish, A. Stiff-Roberts, and P. Bhattacharya, Influence of rapid thermal annealing on a 30 stack InAs/GaAs quantum dot infrared photodetector. *Journal of Applied Physics*, 2003. **94**(8): pp. 5283-5289.

[18] Atwater, H.A. and A. Polman, Plasmonics for improved photovoltaic devices. *Nat Mater*, 2010. **9**(3): pp. 205-213.

[19] Yablonovitch, E., Statistical ray optics. *J. Opt. Soc. Am.*, 1982. **72**(7): pp. 899-907.

[20] Fu, L., I. McKerracher, H.H. Tan, C. Jagadish, N. Vukmirovic, and P. Harrison, Effect of GaP strain compensation layers on rapid thermally annealed InGaAs/GaAs quantum dot infrared photodetectors grown by metal-organic chemical-vapor deposition. *Applied Physics Letters*, 2007. **91**(7): pp. 073515.

[21] Laghumavarapu, R.B., M. El-Emawy, N. Nuntawong, A. Moscho, L.F. Lester, and D.L. Huffaker, Improved device performance of InAs/GaAs quantum dot solar cells with GaP strain compensation layers. *Applied Physics Letters*, 2007. **91**(24): pp. 243115.

[22] Spitzer, W.G. and J.M. Whelan, Infrared Absorption and Electron Effective Mass in n-Type Gallium Arsenide. *Physical Review*, 1959. **114**(1): pp. 59-63.

[23] Turner, S., S. Mokkapati, G. Jolley, L. Fu, H.H. Tan, and C. Jagadish, Periodic dielectric structures for light-trapping in InGaAs/GaAs quantum well solar cells. *Optics Express*, 2013. **21**(9): pp. A324-A335.

[24] Lee, K., J.D. Zimmerman, X. Xiao, K. Sun, and S.R. Forrest, Reuse of GaAs substrates for epitaxial lift-off by employing protection layers. *Journal of Applied Physics*, 2012. **111**(3): pp. 033527.

[25] Bauhuis, G.J., P. Mulder, E.J. Haverkamp, J.C.C.M. Huijben, and J.J. Schermer, 26.1% thin-film GaAs solar cell using epitaxial lift-off. *Solar Energy Materials and Solar Cells*, 2009. **93**(9): pp. 1488-1491.